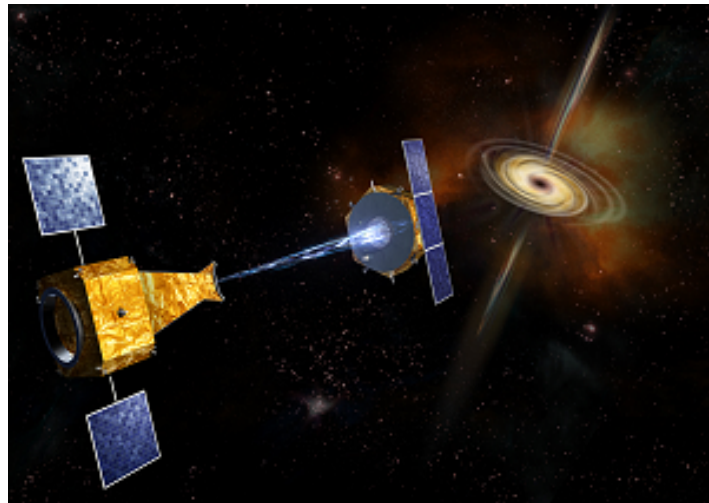


# Compact objects with neutron stars observed with Simbol-X



Diploma thesis

submitted by

Benjamin Mück

Eberhard Karls Universität Tübingen  
Fakultät für Mathematik und Physik  
Institut für Astronomie und Astrophysik  
Abteilung Astronomie

June, 2009



# Contents

<b>1</b>	<b>Introduction</b>	<b>3</b>
<b>2</b>	<b>X-ray satellites</b>	<b>5</b>
2.1	Past Missions . . . . .	5
2.1.1	Uhuru . . . . .	5
2.1.2	Einstein . . . . .	5
2.1.3	EXOSAT . . . . .	6
2.1.4	ROSAT . . . . .	7
2.1.5	BeppoSax . . . . .	7
2.2	Current Missions . . . . .	8
2.2.1	Rossi XTE . . . . .	8
2.2.2	XMM-Newton . . . . .	9
<b>3</b>	<b>A new era: Simbol-X and IXO</b>	<b>11</b>
3.1	Focusing of X-rays . . . . .	11
3.2	<i>Simbol-X</i> . . . . .	12
3.2.1	Performance . . . . .	12
3.2.2	Focusing optic . . . . .	13
3.2.3	Focal plane . . . . .	13
3.2.4	Science with <i>Simbol-X</i> . . . . .	15
3.3	International X-ray observatory - IXO . . . . .	17
3.3.1	Satellite and performance . . . . .	17
3.3.2	Instruments . . . . .	18
3.3.3	Science with IXO . . . . .	19
<b>4</b>	<b>X-ray binaries</b>	<b>21</b>
4.1	Equipotential surfaces and Roche lobe . . . . .	21
4.2	Formation of X-ray binaries . . . . .	21
4.2.1	High Mass X-ray Binaries . . . . .	22
4.2.2	Low Mass X-ray Binaries - <i>LMXB</i> . . . . .	23
4.3	Accretion . . . . .	26
4.3.1	Idea of Accretion . . . . .	26
4.3.2	Eddington Luminosity . . . . .	26
4.3.3	Roche lobe overflow - accretion discs . . . . .	27
4.3.4	Stellar wind Accretion . . . . .	29

<b>5</b>	<b>Properties of X-ray binaries</b>	<b>31</b>
5.1	Origin of X-rays . . . . .	31
5.1.1	Blackbody radiation . . . . .	31
5.1.2	Bremsstrahlung . . . . .	32
5.1.3	Synchrotron radiation . . . . .	32
5.1.4	Compton scattering . . . . .	33
5.1.5	Fluorescence . . . . .	34
5.2	Timing properties . . . . .	35
5.3	Spectral properties of <i>HMXB</i> . . . . .	36
5.4	Spectral properties of <i>LMXB</i> . . . . .	37
5.4.1	Western model - Birmingham model . . . . .	38
5.4.2	Eastern model . . . . .	38
5.4.3	Powerlaw and reflection component . . . . .	40
<b>6</b>	<b>Broad iron lines and quasi periodic oscillations</b>	<b>41</b>
6.1	Broad iron lines . . . . .	41
6.1.1	List of all observed broad iron line in <i>LMXB</i> . . . . .	42
6.1.2	Mechanism of broadening . . . . .	42
6.2	kilohertz Quasi Periodic Oscillations . . . . .	45
6.2.1	Detection of <i>kHz QPOs</i> . . . . .	45
6.2.2	List of all observed QPOs in <i>LMXRBS</i> . . . . .	46
6.2.3	Orbital motion . . . . .	47
6.2.4	Models of <i>kHz QPOs</i> . . . . .	49
<b>7</b>	<b>Results</b>	<b>53</b>
7.1	Xspec and IDL . . . . .	53
7.1.1	Xspec - A X-ray spectral fitting package . . . . .	53
7.1.2	IDL - Interactive Development Language . . . . .	54
7.2	Studied Sources . . . . .	55
7.2.1	Serpens X-1 . . . . .	57
7.2.2	4U 1820-303 . . . . .	60
7.2.3	4U 1636-536 . . . . .	64
7.3	Quasi Periodic Oscillations . . . . .	68
7.3.1	Simulations . . . . .	68
<b>8</b>	<b>Conclusions and final remarks</b>	<b>73</b>
<b>9</b>	<b>References</b>	<b>75</b>
<b>10</b>	<b>Online References</b>	<b>81</b>

# List of Figures

1.1	Absorption of electromagnetic waves in the Atmosphere . . . . .	4
2.1	All Uhuru Sources . . . . .	6
2.2	Einstein sources up to 1 keV . . . . .	6
2.3	ROSAT all sky survey bright sources . . . . .	7
2.4	Artistic view of RXTE and XMM-Newton . . . . .	8
3.1	Wolter Type I telescope . . . . .	12
3.2	Orbit of <i>Simbol-X</i> . . . . .	13
3.3	Focal plane assembly of <i>Simbol-X</i> . . . . .	15
3.4	Sensitivity and effective area of <i>Simbol-X</i> . . . . .	16
3.5	IXO in On-orbit and launch configuration . . . . .	17
3.6	Wide Field and Hard X-ray Imager of IXO . . . . .	19
3.7	Spectral resolution and effective area of <i>IXO</i> . . . . .	20
4.1	Equipotential surfaces and Roche Lobe, Wilms 1996 . . . . .	22
4.2	Distributions of <i>LMXB</i> and <i>HMXB</i> in the galaxy . . . . .	23
4.3	Illustration of <i>HMXB</i> . . . . .	24
4.4	Illustration of <i>LMXB</i> . . . . .	25
4.5	Illustration of a thin accretion disc . . . . .	28
4.6	Illustration of the stellar wind . . . . .	29
5.1	Blackbody spectra for different temperatures . . . . .	32
5.2	Illustration of compton scattering . . . . .	33
5.3	Spectrum of a comptonized blackbody spectrum . . . . .	34
5.4	Fluorescence and transition of an electron . . . . .	34
5.5	Dips and Eclipses at different inclination angles . . . . .	35
5.6	Color-color diagram of Atoll and Z-Source . . . . .	37
5.7	Illustration of a <i>LMXB</i> extended accretion disc corona . . . . .	38
5.8	Illustration of a <i>LMXB</i> emission region after the Eastern Model . . . . .	38
5.9	Emission spectrum of a geometrical thin accretion disc . . . . .	39
6.1	Equation of state for neutron stars . . . . .	42
6.2	Profile of a broadened Iron line . . . . .	43
6.3	<i>kHz QPOs</i> in Sco X-1 . . . . .	45
6.4	<i>kHz QPOs</i> orbits and the ISCO of a neutron star . . . . .	47
6.5	<i>kHz QPOs</i> frequency difference versus the higher frequency . . . . .	49
6.6	Radial and vertical epicyclic frequencies vs. $r/r_g$ . . . . .	50

6.7	Beat frequency model and sonic-point model . . . . .	51
7.1	Serpens X-1 with <i>Simbol-X</i> and <i>IXO</i> . . . . .	56
7.2	Iron line in Serpens X-1 with Suzaku . . . . .	57
7.3	Iron line in Serpens X-1 with <i>Simbol-X</i> and <i>IXO</i> . . . . .	58
7.4	Iron line in 4U 1820-303 with Suzaku . . . . .	60
7.5	4U 1820-303 with <i>Simbol-X</i> and <i>IXO</i> . . . . .	61
7.6	4U 1820-303 with <i>Simbol-X</i> and <i>IXO</i> . . . . .	63
7.7	Iron line in 4U 1636-536 with XMM-Newton and RXTE . . . . .	64
7.8	4U 1636-536 with <i>Simbol-X</i> and <i>IXO</i> . . . . .	65
7.9	4U 1636-536 with <i>Simbol-X</i> and <i>IXO</i> . . . . .	67
7.10	<i>kHz</i> QPOs in 4U 1820-303 . . . . .	68
7.11	Exponential distribution of photons . . . . .	69
7.12	<i>kHz</i> QPOs with <i>IXO</i> . . . . .	71
7.13	<i>kHz</i> QPOs with <i>Simbol-X</i> . . . . .	72

# List of Tables

3.1	Scientific requirements for <i>Simbol-X</i> . . . . .	14
3.2	Optic parameters for <i>Simbol-X</i> . . . . .	14
3.3	Scientific requirements for <i>IXO</i> . . . . .	18
5.1	Properties of <i>LMXB</i> and <i>HMXB</i> . . . . .	36
6.1	Table of all <i>LMXB</i> with relativistic broadened iron line . . . . .	42
6.2	all <i>LMXB</i> with <i>kHz QPOs</i> . . . . .	46
7.1	Continuum parameters for Serpens X-1, 4U 1820-303 and 4U 1636-536 . . . . .	55
7.2	Line parameters for Serpens X-1, 4U 1820-303 and 4U 1636-536 . . . . .	55
7.3	Fit parameters for 4U 1820-303 with <i>Simbol-X</i> and <i>IXO</i> . . . . .	61
7.4	Fit parameters for 4U 1636-536 with <i>Simbol-X</i> and <i>IXO</i> . . . . .	65



# Zusammenfassung

Die Zielsetzung dieser Arbeit ist es, die Möglichkeiten von *Simbol-X* in der Detektion der Eigenschaften von low mass X-ray binaries mit Neutronensternen zu untersuchen und aufzuzeigen. Die zu untersuchenden Eigenschaften sind die relativistisch verbreiterten Eisenlinien, sowie die quasi periodischen oszillationen (QPO) im Zeitbereich von millisekunden. Zudem wurden ebenfalls die Möglichkeiten von *IXO*, dem International X-ray observatory, aufgezeigt.

*Simbol-X* ist ein geplanter Satellit für den Röntgenbereich von 0.5–80 keV. Um Photonen in dem Bereich über 10 keV fokussieren zu können, wird *Simbol-X* der erste Satellit sein, der eine Fokallänge über 8 Metern haben wird. Dies kann durch einen Formationsflug von zwei Satelliten erreicht werden, wobei auf einem Satelliten die fokussierende Optik und auf dem anderen Satelliten die Detektoren angebracht sind. *IXO* ist ebenfalls ein geplanter Röntgensatellit, der ähnlich wie *Simbol-X* die Möglichkeit bietet Röntgenstrahlung über 10 keV zu fokussieren. *Simbol-X* und *IXO* werden im Kapitel 3 beschrieben.

Messungen der breiten Eisenlinie erlauben Rückschlüsse auf den Ursprungsort der Linie in einer Akkretionsscheibe. Bestimmungen des Beobachtungswinkels des Systems, sowie des inneren Radius der Akkretionscheibe sind möglich. Durch den inneren Radius der Scheibe kann eine obere Grenze für den Radius des Neutronen Sterns festgelegt werden. Die Frequenzen der QPOs geben ebenfalls einen Hinweis auf den Radius des Neutronensterns, sowie auf seine Masse (Kapitel 6).

Kompakte Materie in Neutronensternen wird durch verschiedene Modelle beschrieben, wobei die Beziehung Masse-Radius als Test für diese Modelle dient.

Aus den Simulationen der breiten Eisenlinien und den QPOs wurden die Einschränkungen der gewünschten Parameter bestimmt. Die Differenzierung zwischen verschiedenen Beobachtungswinkeln und inneren Radien wurde für drei Systeme untersucht und das Linienprofil dargestellt (siehe Kapitel 7). Ausserdem wurde die Detektion von hochfrequenten QPOs einer Astrophysikalischen Quelle simuliert.



# Chapter 1

## Introduction

X-ray Astronomy is a child of the 20th Century so it is a relatively young discipline compared to optical astronomy, with its history of 400 years of observations thanks to the invention of the telescope.

The problem is that cosmic X-rays cannot be detected on earth, since they are absorbed at high altitudes of the atmosphere (see. Fig 1.1), mainly via ionisation processes with oxygen. The only way to detect X-rays is above the atmosphere by satellites or, like the first missions, with rockets.

Astronomers are interested in the observation of X-rays, because they tell us something about the hot ( $\geq 10^6 K$ ) objects in the universe. Today plenty of such objects are known: all main sequence stars, supernova remnants, hot gas in clusters of galaxies, Active Galactic Nuclei (AGNs) and binary systems, e.g., Low Mass X-ray Binaries (*LMXB*) emit X-rays. Answers to problems of general physics can be found by observing these objects, e.g., matter under extreme conditions can be studied which is important for nuclear physicists.

In the past there have been a lot of X-ray missions. The instrumentation and the achievements of some past and present missions will be described in Chapter 2. Progression was made from mission to mission in the development of technical options to build satellites as well as detectors. X-ray astronomy is present on the cusp of a completely new kind of X-ray satellite technique. Missions like *Simbol-X* and the International X-ray observatory (*IXO*) are planned to launch in the next decade (*Simbol-X* in 2014 and *IXO* in 2020). For the first time it will be possible to focus high energetic X-rays above 10 keV.

In this thesis the prospects of *Simbol-X* and *IXO* relating to the observation of *LMXB* features will be given. The features are the relativistic broad iron line originating in accretion discs around a compact object and the timing feature kilohertz Quasi Periodic Oscillations (*kHz QPOs*). Observations of these properties provide the ability to determine the Mass-Radius relation of the neutron star, which can be used to probe models for compact matter in neutron stars.

Another interesting part of *Simbol-X* will be the observation with high sensitivity over an extended energy range of 0.5–80 keV with only one satellite. An overview over the instrumentation and the goals of *Simbol-X* and *IXO* will be given in Chapter 3.

In Chapter 4 the formation and evolution of X-ray binary systems will be discussed as well as their source of power, the accretion onto a compact object. The production mechanisms of X-rays and

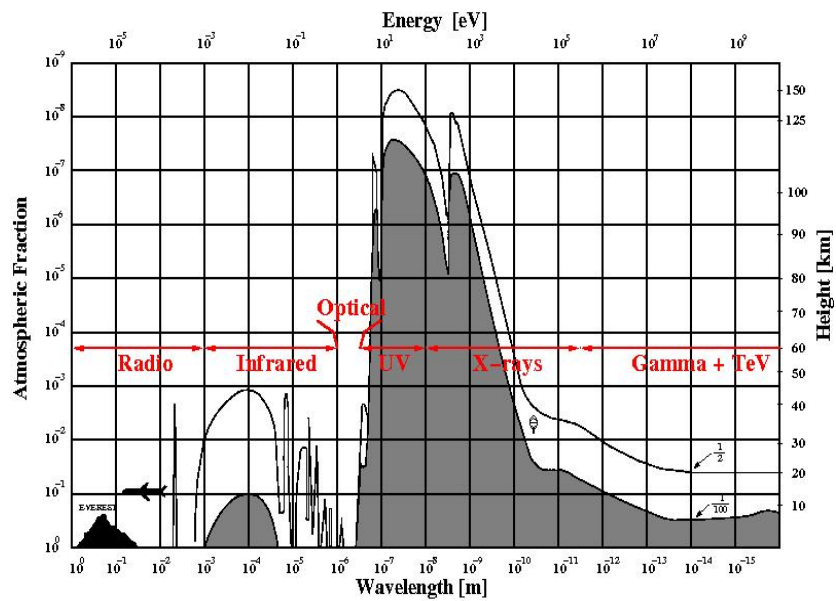


Figure 1.1: Absorption of electromagnetic waves in the atmosphere, T. Schanz & C. Tenzer based on [Giacconi et al. \(1968\)](#)

the spectral and timing properties of X-ray binary systems will be the topic of Chapter 5. The origin of the relativistic broad iron lines and the *kHz QPOs* will be discussed in detail in Chapter 6. In Chapter 7 the simulations for different sources will be described and the outcomes will be discussed. Finally a summary and an outlook of the perspectives of X-ray astronomy will be given.

## Chapter 2

# X-ray satellites

The first X-ray observations were done by rockets in the 1960's. It was 1962 when [Giacconi et al.](#) discovered the first X-ray source, Scorpius X-1. A new universe could be explored now. However the observation time was limited by the flight duration of the rockets. Thus, following the success of the rocket missions, astronomers started to work on the building of the first X-ray satellites which offered a longer observation time. But they had to wait the 1970's when the technology allowed to build scientific satellites. This chapter describes the missions focused on the study of temporal changes of X-ray sources as well as the missions which had a significantly improvement in sensitivity.

### 2.1 Past Missions

#### 2.1.1 Uhuru

The first X-ray satellite was launched in 1970 from Kenya. It was called 'Small Astronomical Satellite 1' (**SAS-1**). After the launch it was renamed to **Uhuru**, which is the Swahili word for freedom celebrate the 7th anniversary of the Independence of Kenya.

Uhuru used proportional counters with an effective area of  $\sim 840 \text{ cm}^2$  to detect X-rays in the energy range of 2–20 keV. The observable flux limit was about 0.1% of the Crab Nebula<sup>1</sup> and an angular resolution of 30' was achieved ([Giacconi et al. 1971](#)).

During the nearly three years of observations 339 X-ray sources were discovered (see Fig. 2.1). Also the first X-ray catalogue by [Forman et al. \(1978\)](#) was published.

#### 2.1.2 Einstein

An improvement of two orders of magnitude in sensitivity was reached in the late 70's with the **High Energy Astrophysical Observatory 2 (HEAO-2)** ([Giacconi et al. 1979](#)). The angular resolution was improved to 1'' using focusing optics. It was the first time that such optics were used on board of a X-ray satellite. HEAO-2 covered the soft X-ray range of 0.2–20 keV. One Wolter Type I telescope (see section 3.1) and four instruments placed in the focal plane were used for observations.

After the launch in 1978 the observatory was renamed to **Einstein**. High resolution spectroscopy of supernova remnants was one of the highlights. A lot of new X-ray sources were detected by Einstein. In Figure 2.2 the sources up to 1 keV seen by Einstein are shown.

---

<sup>1</sup>Flux of Crab Nebula  $\sim 3 \times 10^{-8} \text{ erg cm}^{-2} \text{ sec}^{-1}$

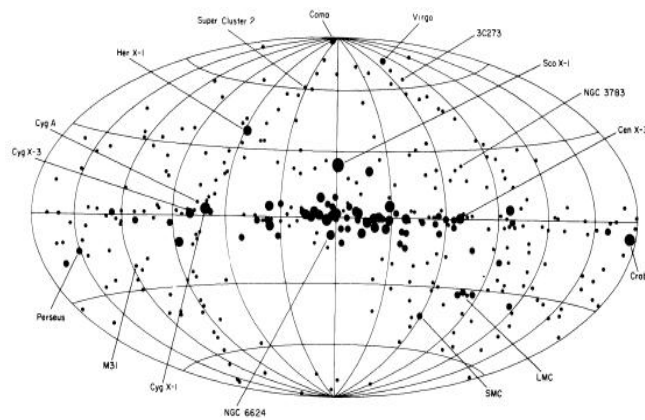


Figure 2.1: All Uhuru sources, [Forman et al. \(1978\)](#)

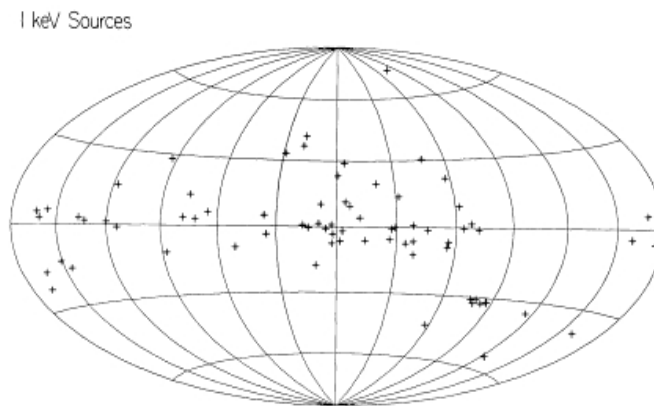


Figure 2.2: Einstein sources up to 1 keV, [Nugent et al. \(1983\)](#)

### 2.1.3 EXOSAT

In 1983 another X-ray satellite called **EXOSAT** (European Space Agency's X-ray Observatory) was launched. For the first time a phenomenon called Quasi Periodic Oscillations (QPOs) in low mass X-ray binaries was observed (Gx 5-1, [Elsner et al. 1986](#)) which will be relevant in this thesis. Also broad iron lines in low mass X-ray binaries were detected ([White et al. 1986](#)). Two Wolter Type I telescopes, each with an effective area of  $90 \text{ cm}^2$  and an energy cut-off at 2 keV were mounted on the satellite. The energy range of 0.05–50 keV was covered by three types of detectors:

- a low energy instrument was placed in the focal plane consisting of a channel multiplier array which was sensitive in an energy range from 0.05–2 keV and had a spatial resolution of  $18''$ , a position sensitive proportional counter and a transmission gratings spectrometer ([de Korte et al. 1981](#))
- a medium energy instrument consisting of two kinds of proportional counter arrays with an effective area of  $1800 \text{ cm}^2$ , an energy coverage from 2 to 50 keV and an energy resolution of

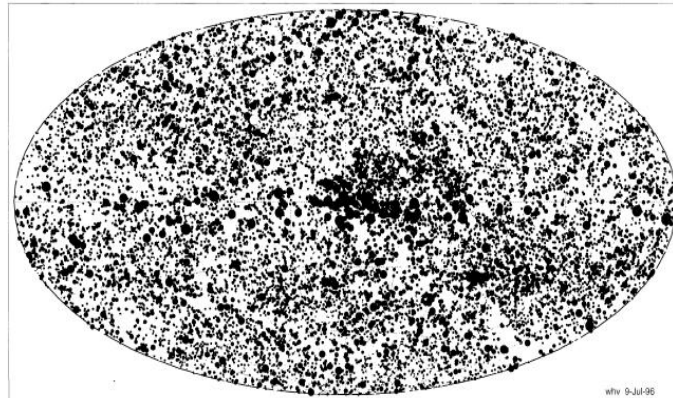


Figure 2.3: ROSAT all sky survey: bright sources in the Energy range of 0.1–2.4 keV. Number of sources 18 811, [Voges et al. \(1999b\)](#)

21% FWHM at 6 keV and 18% FWHM at 22 keV ([Turner et al. 1981](#))

- a gas scintillation proportional counter sensitive in the energy range of 2–40 keV with an energy resolution of 4.5% FWHM at 6 keV ([Peacock et al. 1981](#))

## 2.1.4 ROSAT

In 1990 the mission called **Roentgen Satellite** (short: **ROSAT**) was launched. ROSAT was developed by a collaboration of Germany, the United States and the United Kingdom ([Truemper 1982](#)). The Institut für Astronomie und Astrophysik Tübingen (*IAAT*) participated in the development of the satellite. ROSAT operated for 9 years. It covered the energy range of 0.1–2.5 keV in X-ray and 62–206 eV in the ultraviolet band. An all sky-survey three orders of magnitude more sensitive than Uhuru was performed ([Voges et al. 1999a](#)). Catalogues are also available at the MPE homepage (<http://www.mpe.mpg.de/xray/wave/rosat/catalogue/>). A separate wide field camera with the field of view of 5° was onboard. Additionally, a X-ray telescope with an effective area of 1141 cm<sup>2</sup> and a focal length of 240 cm was used in combination with two kinds of detectors:

- a position sensitive proportional counter which was built of two units each providing an angular resolution of 30'' FWHM at 1 keV and an energy resolution of 45% at 1 keV
- a high resolution imager with an angular resolution of 2''

## 2.1.5 BeppoSax

Another European satellite was launched in 1996 and operated for six years. This Italian project with a contribution of the Netherlands Agency for Aerospace was called **BeppoSAX**. For the first time broad band spectroscopy in the energy range of 0.1–300 keV was possible ([Boella et al. 1997](#)). Such a broad energy coverage was possible with the help of a wide variety of instruments:

- four X-Ray telescopes ([Conti et al. 1994](#))
  - one Low Energy Concentrator Spectrometer (0.1–10 keV) with an angular resolution of 3.5' at 0.25 keV

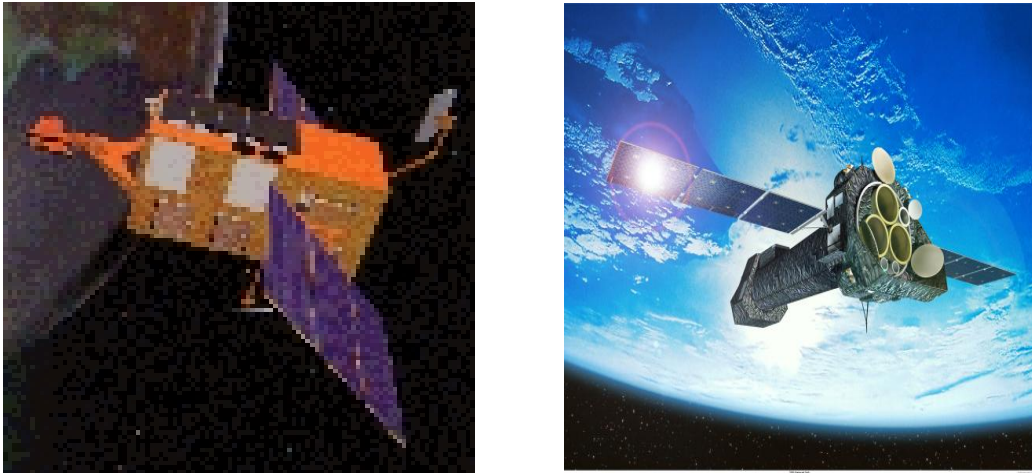


Figure 2.4: On the left side is an artistic view of RXTE, <http://heasarc.gsfc.nasa.gov>. On the right side is an artistic view of XMM-Newton, <http://xmm.esac.esa.int>

- three Medium Energy Concentrator Spectrometer (1.3–10 keV) with an angular resolution of  $1.2'$  at 6 keV (Boella et al. 1995)
- a High Pressure Gas Scintillator Proportional Counter (4–120 keV) (Giarrusso et al. 1995)
- a Phoswich Detection System (15–300 keV) (Frontera et al. 1995)
- a wide field camera (2–30 keV) of  $20^\circ \times 20^\circ$  (Jager et al. 1993)

## 2.2 Current Missions

There are several X-ray satellites presently orbiting the earth. Two of them, RXTE and XMM-Newton will be discussed in the following. RXTE is focused on time variability while XMM-Newton provides observations with a high sensitivity.

### 2.2.1 Rossi XTE

The **Rossi X-ray Timing Explorer (RXTE)**, see Fig.2.4) was launched in the end of 1995. Although it has been planned to operate for two years, RXTE still delivers scientific data. X-ray sources can be observed with a time resolution down to the order of  $\mu\text{s}$ . The Proportional Counter Array (PCA, Jahoda et al. 1996) provides such a time resolution of  $1 \mu\text{s}$  in the energy range of 2–60 keV. Combined with the High Energy X-ray Timing Experiment (HEXTE, Gruber et al. 1996) which is sensitive in the range of 15–250 keV, RXTE offers a high a time resolution over an extended energy range. Additionally an All-Sky Monitor (ASM, Levine et al. 1996) with a sensitivity of 30 mCrab in the energy range from 2–10 keV is mounted on the satellite. RXTE discovered the so called kilohertz Quasi Periodic Oscillations (kHz QPOs, Strohmayer et al. 1996) and measured the spin periods of Low mass X-ray binaries.

### 2.2.2 XMM-Newton

**XMM-Newton** was launched in 1999 with a nominal planned operation timelife up to ten years. XMM stands for X-ray Multi-Mirror Mission, see Fig.2.4. For the first time an optical monitor was mounted on a X-ray satellite. It is sensitive in the range of 180–650 nm and has a 30 cm Optical/UV telescope with a spatial resolution of  $\sim 1''$ . Thanks to that simultaneous measurements in both the X-ray and in the optical waveband could be made (Mason et al. 2001).

The optic of XMM is made of three imaging X-ray telescopes. Each is built out of 58 nested Wolter Type I mirrors with an effective area of  $\sim 1500 \text{ cm}^2$  at 1 keV. The focal length of the mirrors is 7.5 m and a spatial resolution of  $6''$  (FWHM) is achieved.

In the focal plane three types of detectors are placed:

- the European Photon Imaging Camera Metal-Oxide-Silicon (EPIC - MOS, Turner et al. 2001) which covers the energy range 0.1–10 keV and reaches a spectral resolution ( $E/\Delta E$ ) of  $\sim 20$ –50
- the European Photon Imaging Camera-PN (EPIC-PN) which is sensitive up to 15 keV with an angular resolution of  $15''$  at 1.5 keV and 8 keV, observation modes with time resolutions from  $\sim 10 \mu\text{s}$  to 200 ms are available (Strüder et al. 2001) The IAAT has participated in the development of the control and read out electronics for this camera
- the Reflection Grating Spectrometer with a spectral resolution of 200–800 (den Herder et al. 2001)



## Chapter 3

# A new era: *Simbol-X* and *IXO*

X-rays with an energy above 10 keV cannot be focused with current satellites. However, some missions with the intent to solve this problem are planned to start in the next decade. In the following two of these missions will be described in detail, *Simbol-X* and the International X-ray Observatory (*IXO*). *IAAT* participates in both.

First the basics of X-ray focusing and its realization will be discussed.

### 3.1 Focusing of X-rays

To get sharp images of X-ray sources and to detect fainter sources radiation has to be focused. This is just possible by grazing incidence, otherwise the radiation is absorbed in the matter or penetrates it. That total reflection is possible at the transition region of an optical thick to an optical thin medium, for X-rays vacuum is optical thicker than matter. The incident angle needed for reflection depends on the wavelength  $\lambda$  of the radiation and on the density  $\rho$  of the mirror material. This critical angle  $\theta_c$  is calculated by, e.g., [Aschenbach \(1985\)](#):

$$\theta_c = 5.6\lambda\sqrt{\rho} \quad (3.1)$$

with  $\theta_c$  in arcminutes,  $\lambda$  in Angstroms<sup>1</sup> and  $\rho$  in  $\text{g cm}^{-3}$ . X-rays with a wavelength of 0.1 nm ( $\sim 10$  keV) are reflected under an angle of  $\theta_c \sim 0.5^\circ$ . The critical angle and the radius of the mirror shells  $r$  determine the focal length  $f$ :

$$f = \frac{1}{4} \cdot \frac{r}{\theta_c} \quad (3.2)$$

Assuming a X-ray photon with an energy of 10 keV and a mirror radius of  $r=0.35$  m (like at XMM-Newton) the focal length is  $>10$  m. But with a focal length of 7.5 m XMM has already reached this limit. This limitation is set by the means of transport which are too small to carry a satellite which is longer than 8 m.

[Giacconi & Rossi \(1960\)](#) proposed a parabolic mirror to focus X-rays by grazing incidence. But this simple configuration was not sufficient. Though radiation which comes parallel to the optical axis is focused in one point, off-axis radiation is blurred. Another way to focus X-rays was shown by [Wolter \(1952a,b\)](#). He suggested a combination of a hyperbolic and a parabolic shaped mirror. Three different combinations were developed, but the commonly used combination is Type I because its

---

<sup>1</sup> 1 Angstrom  $\equiv$  0.1 nm

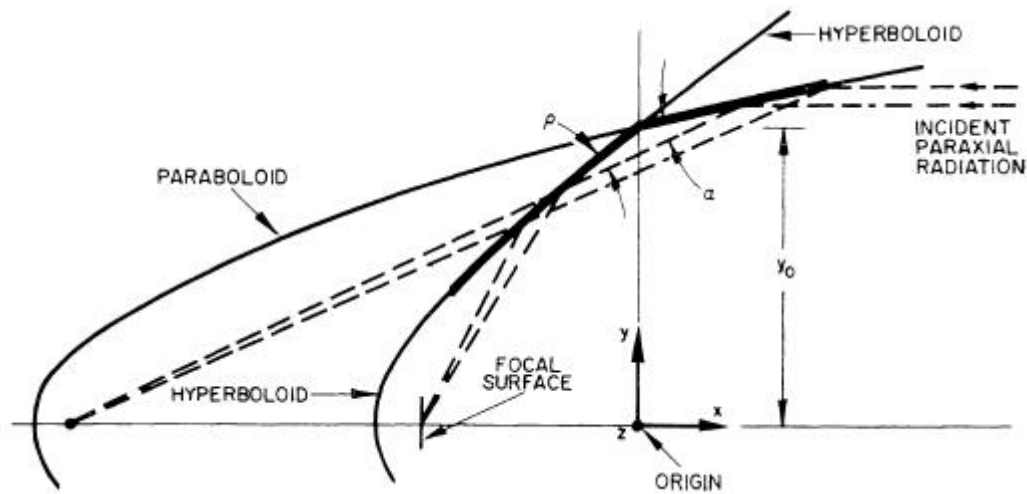


Figure 3.1: a schematic cross section of a Wolter type I telescope, [Giacconi et al. \(1969\)](#)

configuration is easy to realize (see Figure 3.1). Further it allows to nest many mirror shells because of the small reflection angles the inner part of the mirrors is not used. Thereby the effective area of the telescope increases. To shorten the focal length mirrors are made of materials with high densities (see Eq. 3.1). Typically Gold (like in XMM-Newton) or Iridium (Chandra) with densities about  $20 \text{ g cm}^{-3}$  are used

## 3.2 *Simbol-X*

*Simbol-X* is a collaboration of the French CNES<sup>2</sup> and the Italian ASI<sup>3</sup> with participation of Germany, namely the IAAT, the MPE<sup>4</sup> in Garching, the University of Darmstadt and the University of Erlangen-Nuremberg.

### 3.2.1 Performance

*Simbol-X* will be launched from Kourou, French Guiana and will be brought to a high elliptical orbit around the earth (see Fig. 3.2). Previous missions have shown that there is a low particle background above  $\sim 75\,000 \text{ km}$ , therefore an elliptical orbit with a perigee of  $\sim 20\,000 \text{ km}$  and an apogee of  $\sim 180\,000 \text{ km}$  is chosen. For this orbit observations are possible in 83% of the four days period. Furthermore uninterrupted measurements of up to 100 ks can be performed and in 4.5 months the whole sky can be covered.

All in all more than 1 000 pointings during the two years lasting nominal mission are planned. An extension of two years with 500 additional pointings is possible ([Ferrando et al. 2008](#)).

To focus also X-rays above 10 keV the observations will be performed with a focal length of 20 m. This is just possible by a formation flight of two satellites. For the first time the focusing optics are mounted on one spacecraft and the detector instruments on another spacecraft. To provide a stable

<sup>2</sup>Centre Nationale d'Etudes Spatiales

<sup>3</sup>Agenzia Spaziale Italiana

<sup>4</sup>Max Planck Institut für Extraterrestrische Physik

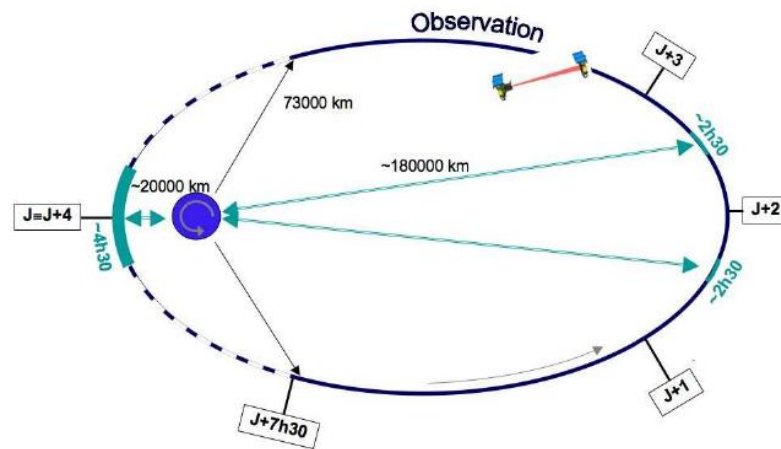


Figure 3.2: An illustration of the orbit of *Simbol-X*, Ferrando et al. (2008)

image quality the relative position of the two spacecrafts have to be known with an accuracy of  $\pm 0.3$  mm. Further the focal length is allowed to vary in a range of  $\pm 3$  cm. Thanks to the enlargement of the focal length improvements in spectral and angular resolution at energies above 10 keV will be reached. A summary of the scientific requirements is given in Table 3.2.

### 3.2.2 Focusing optic

A Wolter Type I telescope with multilayer coating mirrors is used for focusing. To increase the reflectivity each mirror is built out of 250 layers made of alternately Platinum and Carbon. Simulations by Cotroneo et al. (2008) show that the desired effective area is reached by 100 mirrors nested. Further optic parameters are shown in Table 3.2.

### 3.2.3 Focal plane

The focal plane consists of a collimator and the Focal Plane Assembly (FPA, see Fig. 3.3). A collimator is needed to deflect the light which does not come from the field of view, in order to suppress the background in the two detectors of the FPA. Both detectors are made out of  $128 \times 128$  pixels and have a pixel size of  $625 \times 625 \mu\text{m}^2$ . They are placed on top of each other to keep both as close as possible to the focal point. They are just separated by an aluminum foil to avoid electrical interferences.

- Low Energy Detector - LED

The LED is first illuminated by the focused radiation. It gets more transparent the more energetic the photons are. The detector is built out of silicon with a thickness of  $450 \mu\text{m}$  and covers an energy range of  $\sim 0.5\text{--}20$  keV. The LED is divided into four quadrants of  $64 \times 64$  pixels. Each quadrant has its own signal processing electronics. Hence all can be read-out parallel what leads to a read-out time of  $256 \mu\text{s}$  (one row is read-out in  $4 \mu\text{s}$ ). This is provided by a CAMEX<sup>7</sup> chip (Lechner 2009).

<sup>5</sup>HPD = Half Power Diameter: The diameter in where half of the power is deposited

<sup>6</sup>Half energy width: the width at the half of the maximum energy

<sup>7</sup>Charge Amplifier MultipLEXer

Table 3.1: Scientific requirements for *Simbol-X*, values taken from Ferrando et al. (2008)

Parameter	Value
Energy band	0.5–80 keV
Field of view (at 30 keV)	$\geq 12'$ (diameter)
Spectral resolution	40–50 @ 6–10 keV
$E/\Delta E$	50 @ 68 keV
On axis sensitivity $3\sigma$ , 1 Ms	$\sim 0.5\mu\text{Crab}$ @ 10–30 keV
On axis effective area	$\geq 100\text{ cm}^2$ @ 0.5 keV $\geq 1000\text{ cm}^2$ @ 2 keV $\geq 600\text{ cm}^2$ @ 8 keV $\geq 300\text{ cm}^2$ @ 30 keV $\geq 100\text{ cm}^2$ @ 70 keV $\geq 50\text{ cm}^2$ @ 80 keV
Angular resolution (HPD) <sup>5</sup>	$< 20''$ @ $< 30\text{ keV}$ $< 40''$ @ 60 keV

Table 3.2: Optic parameters for *Simbol-X*, values taken from Pareschi & the SIMBOL-X collaboration (2008)

Material for the mirror walls	Electroformed Ni (or Ni-Co)
Min-Max top diameter	260–650 mm
Min-Max angles of incidence	$0.18^\circ$ – $0.23^\circ$
Angular resolution HEW <sup>6</sup>	$20''$ (goal: $15''$ )

- High Energy Detector - **HED**

The *HED* covers the energy range of 10–80 keV. The detector is divided into 8 Caliste modules with each  $16 \times 16$  pixels. A Caliste module is made out of a Cadmium Telluride crystal with a thickness of 2 mm and the beneath fixed electronics. Each module can be read-out independent. It takes  $50\mu\text{s}$  to read-out one module by an IDeF-X<sup>8</sup> chip (Meuris et al. 2009).

The detectors are surrounded by a background reduction system which is composed of an active shielding made out of plastic scintillators which gives a veto signal if a charged particle passed through it. The veto ensures that no data is taken because the charged particle can produce signals in the detectors either by passing through them or by generating photons which are detected. Additionally a passive shielding made out of Tantalum reduces the background from photons coming from all over the sky except from the field of view.

Further a calibration wheel with two known radioactive sources ( $^{60}\text{Fe}$  and  $^{241}\text{Am}$ ) is mounted on the

<sup>8</sup>Imaging Detector Front-end for X-rays

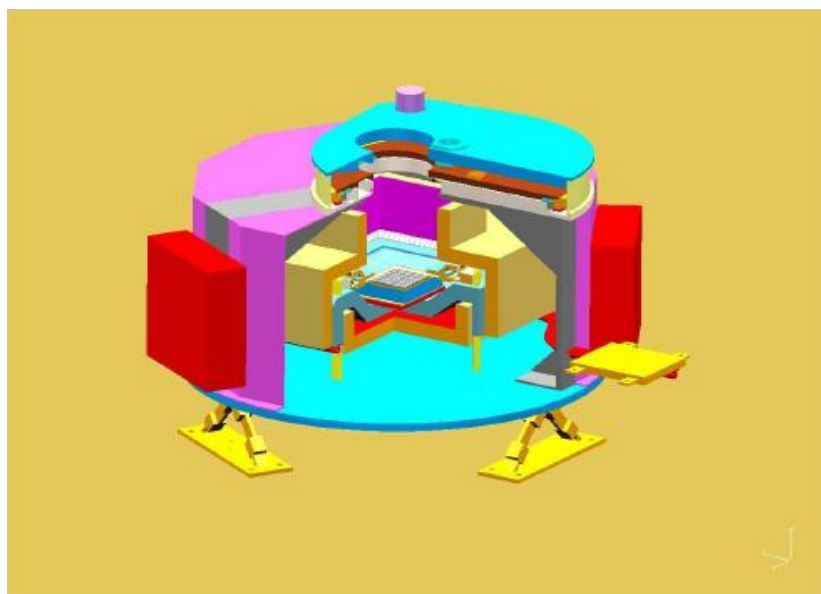


Figure 3.3: Cut view of the focal plane assembly. The active shielding, in orange, is divided into two parts to surround the imaging detectors. On top is the calibration wheel [Laurent et al. 2008](#).

FPA. This wheel can be put in three different positions, open (for observations), closed (to protect the detectors from high radiation) and calibration ([Laurent et al. 2008](#)).

### 3.2.4 Science with *Simbol-X*

The improvements in the continuum sensitivity compared to previous missions and the increase in effective area compared to the EPIC-PN of XMM are shown in Figure 3.4. Thanks to that properties a variety of X-ray sources can be explored by *Simbol-X*. More details are given in [Fiore et al. \(2008\)](#). The main goals of *Simbol-X* are::

- **Physics of black holes**

All X-ray sources contribute to the Cosmic X-ray Background (CXB) which was resolved to an energy of 7 keV by previous missions. Super-Massive Black Holes (SMBH) in Active Galactic Nuclei (AGN) are assumed to be the main contributor to the CXB. But with the known sources the maximum of the CXB at 30 keV is missed by a factor of three. [Setti & Woltjer \(1989\)](#) proposed a high population of obscured AGN in which soft X-rays (<20 keV) are absorbed by optical thick tori around the Black Hole. Due to the above shown improvements in sensitivity *Simbol-X* will be able to discover obscured AGN up to a redshift of  $z \sim 1.5$  ([Della Ceca et al. 2008](#)). The goal is to resolve 50% of the sources at 30 keV and make a census of SMBH.

- **Outflows of AGN**

The radiation fields and outflows (winds and jets) of AGN have an effect on their environment. XMM-Newton and Chandra observations of blue-shifted iron absorption lines determine the velocity of the outflows to a fraction of the speed of light. *Simbol-X* is able to study in more

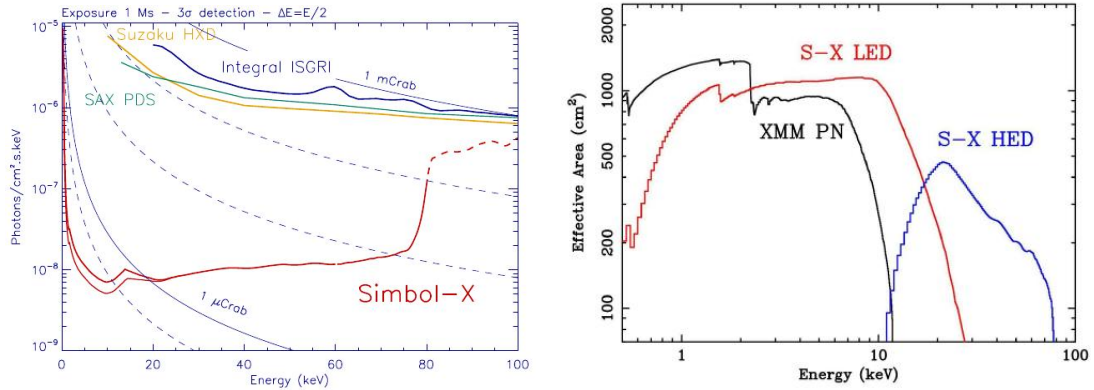


Figure 3.4: On the left panel the continuum sensitivity of *Simbol-X* for measuring broad band source spectra with  $3\sigma$  accuracy in an observation time of 1 Ms is shown. On the right panel the effective area of both *Simbol-X* detectors compared to EPIC-PN camera of XMM-Newton is shown, [Ferrando et al. \(2008\)](#).

detail the time evolution of spectral absorption structures and conclude on the dynamics of the highly ionized gas ([Cappi et al. 2008](#)).

- **Acceleration mechanisms**

Particle acceleration in supernova remnants produces non-thermal emission. The covering of a broad energy band is helpful to separate the thermal and non-thermal emission. To probe possible mechanisms of acceleration, e.g, the cut off energy of the synchrotron radiation can be measured.

But not only large objects or high energy events can be observed with *Simbol-X*.

This thesis will study the performances of *Simbol-X* in the spectral and time behaviour of *LMXB* with neutron stars. Thanks to the good spectral resolution of 150 eV at 6 keV relativistic broad iron lines in *LMXB* can be resolved (see more in Section 6.1.2). Additionally a spectrum over an extended energy range of *LMXB* can be obtained.

A time resolution below  $200 \mu\text{s}$  provide the ability to detect *kHz QPOs*.

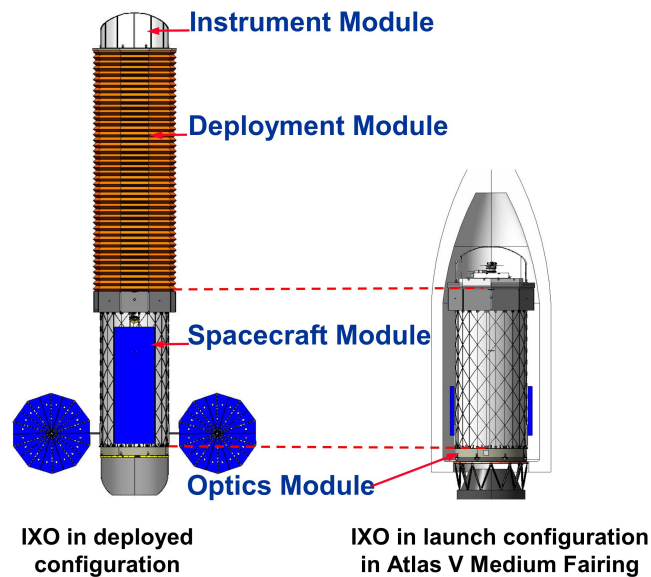


Figure 3.5: Illustration of *IXO* in On-orbit and launch configuration, <http://ixo.gsfc.nasa.gov>

### 3.3 International X-ray observatory - IXO

*IXO* is a collaboration of NASA, ESA and JAXA<sup>9</sup>. It resulted out of a merge of two missions, *Con-X* (NASA) and *XEUS* (ESA/JAXA). Nearly all information are taken from [Bookbinder et al. \(2009\)](#) and the *IXO* homepage (<http://ixo.gsfc.nasa.gov>).

#### 3.3.1 Satellite and performance

*IXO* will not be in a formation flight configuration like *Simbol-X*. Instead it will be launched in 2020 by a launch vehicle in the retracted position and extend in orbit (see Figure 3.5). It will be placed in a 800 000 km semi-major axis orbit around the L2 libration point of the sun-earth system. The mission has a nominal operation time of five years with a possible extension of additional five years.

The satellite will consist of four modules:

- the **optics module** with a Wolter Type I telescope which provides a large effective area (see Table 3.3). Two new mirror technologies are developed for *IXO*. The Goddard Space Flight Center (GSFC, San Diego) develops the so called slumped-glass optics, which provides the ability to produce high-quality mirrors in a short time ([Pareschi et al. 2009](#)). The European counterpart is called Silicon Pore optics with very light, stiff and modular optics. Large apertures can be built with this technique.
- the **instrument module** containing an X-ray Grating Spectrometer (*XGS*) and five instruments mounted on a Movable Instrument Platform (*MIP*): an X-ray Microcalorimeter Spectrometer (*XMS*), X-ray POLarimeter (*XPOL*), a High Time Resolution Spectrometer (*HTRS*) and the

<sup>9</sup>Japanese Aerospace and Exploration Agency

Table 3.3: Scientific requirements for *IXO*, values taken from [Bookbinder et al. \(2009\)](#)

Parameter	Value	Energy range	Instrument
Spectral resolution $E/\Delta E$	$\Delta E = 2.5 \text{ eV}$	@ 0.3–7 keV	XMS
	$\Delta E = 10 \text{ eV}$	@ 0.3–10 keV	XMS
	$\Delta E = 150 \text{ eV}$	@ 0.1–15 keV	WFI/HXS
	$E/\Delta E = 3000$	@ 0.3–1 keV	XGS
Mirror effective area	$3 \text{ m}^2$	@ 1.25 keV	
	$0.65 \text{ m}^2$	@ 6 keV	
	$150 \text{ cm}^2$	@ 30 keV	
Angular resolution (HPD)	$5''$	@ 0.3–7 keV	XMS
	$5''$	@ 0.1–7 keV	WFI/HXS
	$30''$	@ 7–40 keV	WFI/HXS
Count rate	$10^6 \text{ cps}$ with $<10\%$ deadtime		HTRS

Wide Field and Hard X-ray Imager (*WFI/HXI*). The three latter ones will be described in more detail.

- the **deployment module** which consists of three masts which will be extended in the orbit to the desired focal length of 22 m. Cloths are fixed on the masts to protect the detector from stray light.
- the **spacecraft module** containing solar arrays, thrusters and antennas.

### 3.3.2 Instruments

- High Time Resolution Spectrometer - HTRS

The **HTRS** is able to observe sources with fluxes up to  $10^6$  counts per second. So even for bright sources precise timing measurements can be made in the 0.3–10 keV band with a time resolution of  $1 \mu\text{s}$ . The spectral resolution is 200 eV (FWHM) at 6 keV. The spectrometer is made out of 37 hexagonal Silicon Drift Diodes (SDD) which are placed out of focus to illuminate the whole array.

- Wide Field Imager - WFI

The **WFI** provides the facility to make images simultaneously with spectrally and time resolved photon counting. It is sensitive in an energy range of 0.1–15 keV with a field of view of  $18' \times 18'$ . Nearly 1 million pixels with a size of  $100 \times 100 \mu\text{m}^2$  form a sensitive area of  $10 \times 10 \text{ cm}^2$ . Unlike XMM-Newton which uses CCD-detectors, *IXO* will use a DEPFET<sup>10</sup> Active Pixel Sensor (APS). Since each pixel has its own amplifier, the stored energy in a pixel can be directly read out without being transferred to the edge of the detector. This avoids losses due to charge transfer. The *WFI* will be tested and characterized by the *IAAT*.

<sup>10</sup>Depleted P-channel Field Effect Transistor

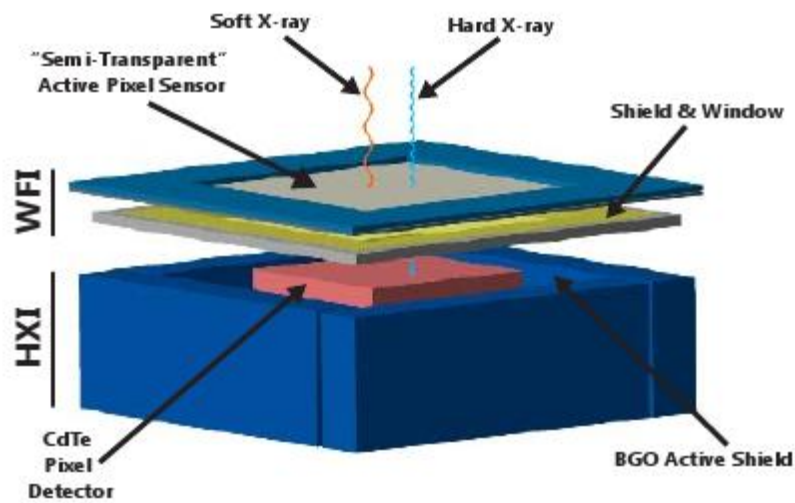


Figure 3.6: Wide Field and Hard X-Ray Imager of IXO. The WFI is in front of the HXI, [Bookbinder et al. \(2009\)](#)

- **Hard X-ray Imager - HXI**

The **HXI** which is placed behind the WFI (see Fig. 3.6) extends the energy coverage up to 40 keV. It is made of Cadmium and Telluride with a thickness of 0.5 mm which provides a 100% detection efficiency for X-rays with an energy of 40 keV. An active bismuth germanate oxide anti-coincidence shield surrounds the HXI to suppress background. Two Double-sided Silicon Strip Detectors (DSSD) are placed above the CdTe detector to detect photons between 7 and 30 keV.

The *WFI* and the *HXI* operate at different temperatures, thus a thermal shield between them is required. Also the mechanical structure, cooling and electronics for the detectors are separated and so each detector can operate independently.

### 3.3.3 Science with IXO

*IXO* will be able to observe with a better spectral resolution and a larger effective area when compared to previous X-ray missions (see Figure 3.7). *IXO* will help to find answers to questions concerning matter under extreme conditions, super massive black holes and large scale structures.

- **Matter under extreme conditions**

Radiation emitted close to a Black Hole is modified by relativistic effects. The conditions in this emission regions can be explored by *IXO*.

Further precise measurements of the mass-radius relation of neutron stars can be performed by *IXO*. This relation can distinguish between different models of neutron stars (see Chapter 6). Another aspect that will be explored by *IXO* will be broad iron lines and high frequency QPOs, especially in low mass X-ray binaries.

- **Black hole evolution**

Super massive black holes play an important role in the formation and evolution of galaxies. *IXO* will provide the capability to observe accretion in SMBH with a red-shift higher than 7.

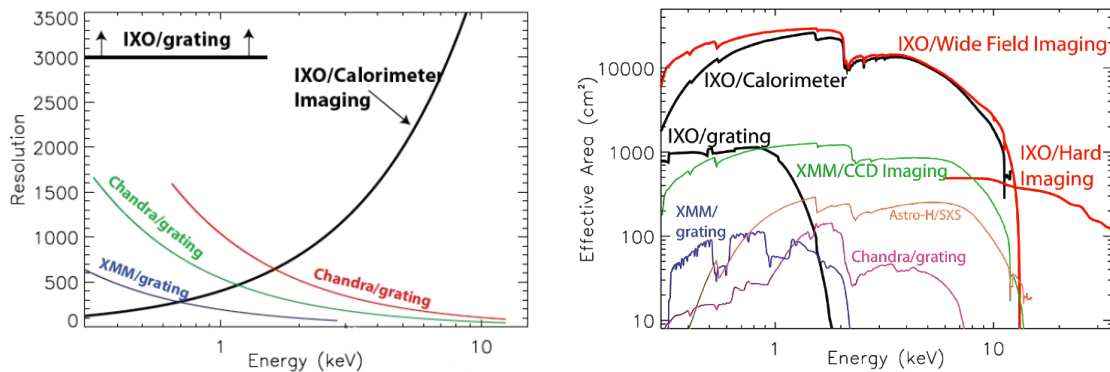


Figure 3.7: On the left panel the spectral resolution of the *IXO* calorimeter and grating compared to current missions. On the right side the effective area of the *IXO* mirror and focal plane instruments are plotted compared to current missions. The large improvement in all energies is shown, <http://ixo.gsfc.nasa.gov>

For the first time a characterization of this population of SMBHs will be possible. At lower red-shifts *IXO* will be able to explore the properties of obscured AGN. About 10 000 AGN will be observed in a survey by *IXO*.

The spin of SMBHs will also be determined by ,e.g., measurements of the broadened iron line. *IXO* will have the ability to do this measurement in different ways.

- **Large scale structures**

Measurements of fluctuations of the gas bulks in Clusters of galaxies will give a new perception of those Clusters. Also the baryonic component of the Universe, in clusters, groups of galaxies and the intergalactic medium will be determined. The origin and the properties of cosmic feedback from SMBH will be explored.

The evolution of Galaxy clusters will be understood better by determining thermodynamical properties and the metal content of the first low-mass clusters seen at  $z \sim 2$ . *IXO* will further measure the abundances and the evolution of metals in the intergalactic medium to reveal when and how the metals were produced.

Further the expansion history of the Universe in combination with the study of the growth of matter density perturbations can be used to probe equation of states for Dark Energy.

- **Life cycles of matter and energy**

Using absorption line measurements *IXO* will determine the distribution of metal abundances in the Milky Way. Also the properties and effects of galactic winds will be explored. But also main-sequence stars will be observed by *IXO*. Their influence on their environment can be studied by measurements of the coronal activities and stellar winds.

A great variety of sources will be studied by *IXO*. Additionally there will be a lot of new, serendipitous discoveries, like in almost every mission which had big technical improvements.

## Chapter 4

# X-ray binaries

X-ray binaries are laboratories for physics at high temperatures of  $10^6$ – $10^9$  K which corresponds to the energy range of  $\sim 1$ – $100$  keV. Binary systems allow to determinate masses of the stars, or at least give the lower limit. Binary systems are built of a compact object (a neutron star or a black hole) and a normal companion star.

They are very bright sources with a luminosity of  $L = 10^{34}$ – $10^{38}$  erg s $^{-1}$  which is up to four orders of magnitude larger than the luminosity of the sun with  $L \sim 4 \times 10^{33}$  erg s $^{-1}$ . This great amount of energy is produced by mass accretion onto the compact object.

In the following sections the formation of X-ray binaries will be discussed, and an overview over the accretion process will be given. Most information in the following is taken out of [Lewin et al. \(1995\)](#) and [Lewin & van der Klis \(2006\)](#).

### 4.1 Equipotential surfaces and Roche lobe

In binary systems the gravitational potential is formed by the gravity of both stars and their motion around the center of mass. The potential  $\phi$  can be calculated in a reference frame corotating with the binary system and is given with:

$$\phi = -\frac{GM_1}{r_1} - \frac{GM_2}{r_2} - \frac{\omega^2 r_3^2}{2} \quad (4.1)$$

where  $r_1$  and  $r_2$  are the distance to the center of the stars,  $M_1$  and  $M_2$  their masses,  $r_3$  the distance to the rotation axis of the binary, and  $\omega$  is the orbital angular velocity. The equipotential surfaces, which depend only on the mass ratio  $M_1/M_2$ , are shown in Figure 4.1. The innermost surface which encloses both stars is called Roche lobe<sup>1</sup>. A particle inside one lobe is gravitationally bound to the corresponding star. The intersection point of the Roche lobes is called inner Lagrangian point ( $L_1$ ). At this point no effective force would act on a test particle and it could stay there theoretically forever.

### 4.2 Formation of X-ray binaries

X-ray binaries result out of a binary system consisting of two main-sequence stars. The more massive star evolves faster and will at some point fill its Roche lobe. Hence, matter can be transferred by Roche

---

<sup>1</sup>First mentioned 1849 by Edouard Albert Roche

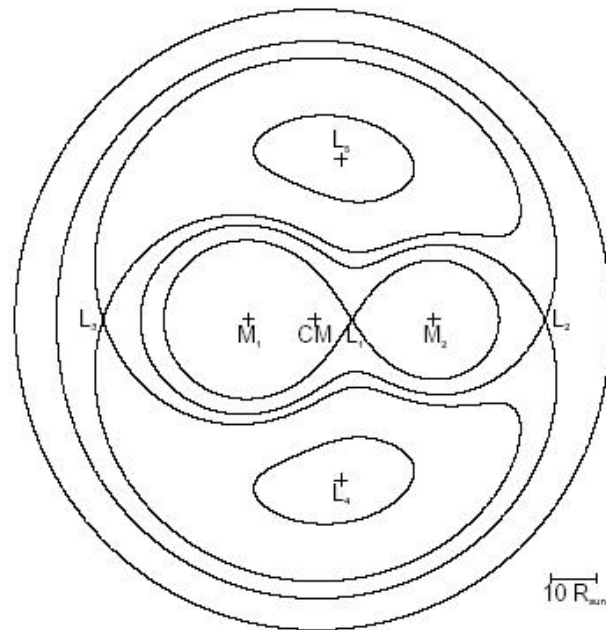


Figure 4.1: An illustration of the gravitational equipotential surfaces. The Roche lobe surrounds both stars. Also the lagrangian points, where an object would stay stationary relative to the both stars, are shown, Wilms 1996

lobe overflow via the inner Lagrangian point from the massive star to its companion. Depending on the transferred mass, one of the stars reaches the end of its life and may explode in a supernova. The nature of the resulting compact object depends on the mass of the progenitor star. In general, stars with masses below  $8 M_{\odot}$  end as white dwarfs, neutron stars are produced by stars with masses in the range of  $\sim 8\text{--}40 M_{\odot}$ , above that mass black holes can be formed. An overview over the formation of compact objects is given by, e.g., [Muno \(2007\)](#).

The further evolution of the system will be described separately, as two subclasses of X-ray binaries exist, the High Mass X-ray Binaries (*HMXB*) and the Low Mass X-ray Binaries (*LMXB*), their distribution in the Galaxy is shown in Figure 4.2. The *LMXB* will be the topic of this thesis.

#### 4.2.1 High Mass X-ray Binaries

The progenitor system of a *HMXB* has to consist of two massive stars with masses typically exceeding  $12 M_{\odot}$  to be above the supernova explosion limit. In Figure 4.3 a possible evolution track of such a system is illustrated, but the exact evolution depends strongly on the initial conditions.

The more massive star star explodes in a supernova and creates a compact object. Although the remaining normal star does not fill its Roche lobe, accretion can take place by capturing a fraction of the stellar wind. At this stage the object is seen as a *HMXB* with typical sizes of  $\sim 20 R_{\odot}$  and orbital periods of some days. The lifetime of *HMXB* depends on the evolution time of massive stars which is known to be relatively short leading to *HMXB* lifetimes in the range of  $10^5\text{--}10^7$  years.

After this period of accretion the normal star expands and fills its Roche lobe or even fill the orbit of the system, creating a common envelope around both objects. This leads to high losses of

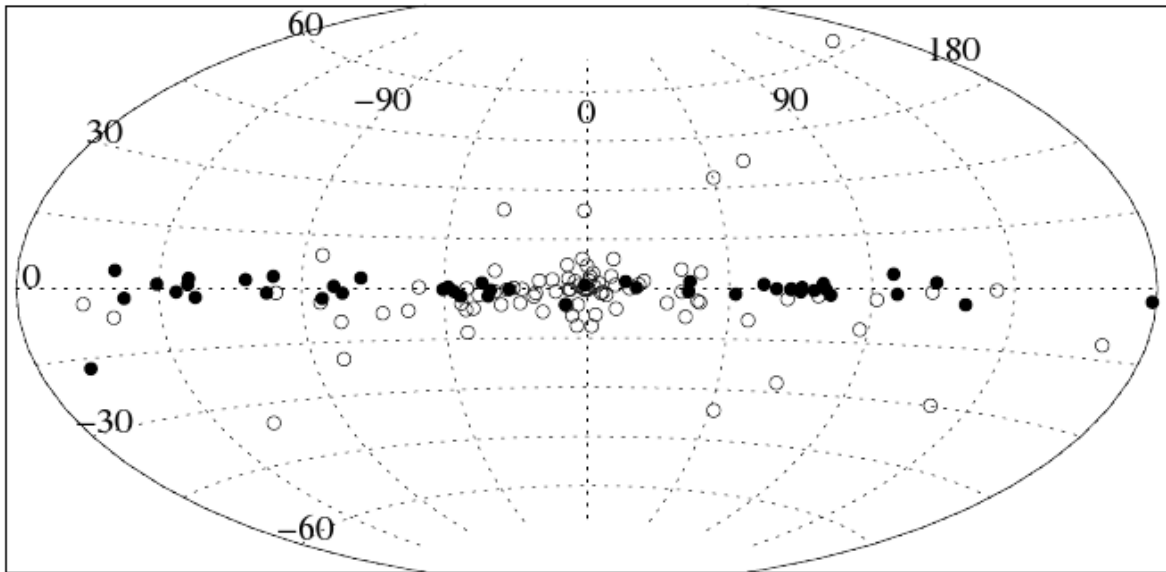


Figure 4.2: Distributions of *LMXB* (open circles) and *HMXB* (filled circles) in the Galaxy, Grimm et al. (2003)

angular momentum and the compact object spirals inwards. Eventually the second star explodes in a supernova and a close system consisting of two neutron stars or a neutron star and a white dwarf (depending on the masses) is produced.

#### 4.2.2 Low Mass X-ray Binaries - *LMXB*

The progenitor system of a *LMXB* consists of two main sequence stars, one of them is a massive star with  $M > 10 M_{\odot}$  and the other one with a typical mass of  $\sim 1.6 M_{\odot}$ . An example scenario of the evolution is shown in Figure 4.4.

When the massive star expands the system will be in a common envelope phase, thus the companion loses angular momentum and spirals in. This phase ends with the supernova explosion of the massive star, which creates a binary system composed of a compact object and a normal star. However, if the normal star fills its Roche lobe during its stellar evolution, mass overflow via the inner Lagrangian point can take place. Due to the conservation of angular momentum, an accretion disc forms around the compact object (see the next section). At this stage the system is observed as a *LMXB* with typical sizes of several solar radii and an orbital period of several hours. The lifetime of a *LMXB* is limited by the accretion timescale which leads to lifetimes in the range of  $10^7$ – $10^9$  years.

At the end of the evolution the system consists of a neutron star, e.g., a millisecond Pulsar and a white dwarf.

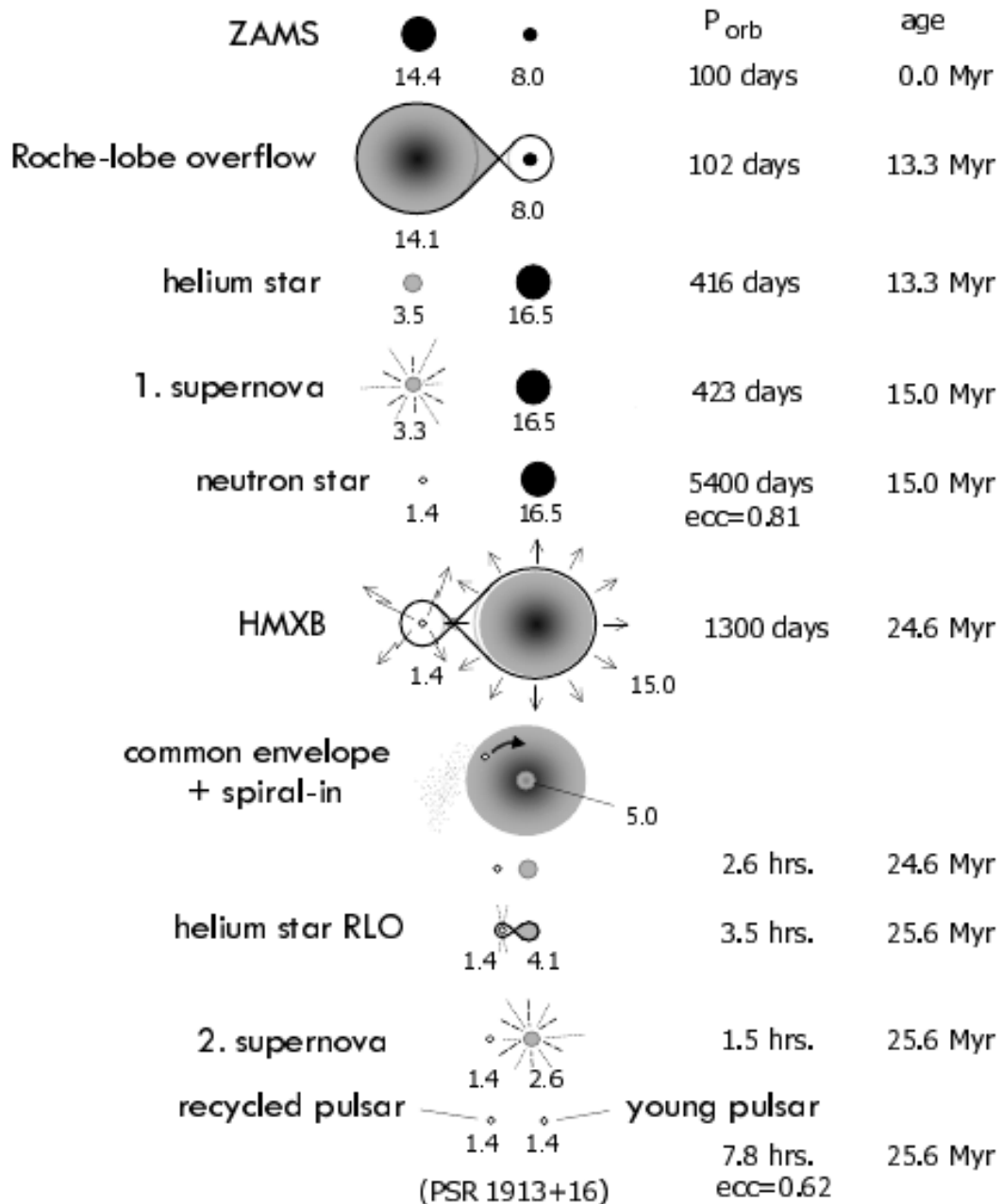


Figure 4.3: Illustration of the evolution of *HMXB*. The masses are typical start masses. In every step there is a transfer of matter. The evolution time for *HMXB* is of the order  $\sim 10^7$  years (Lewin & van der Klis 2006)

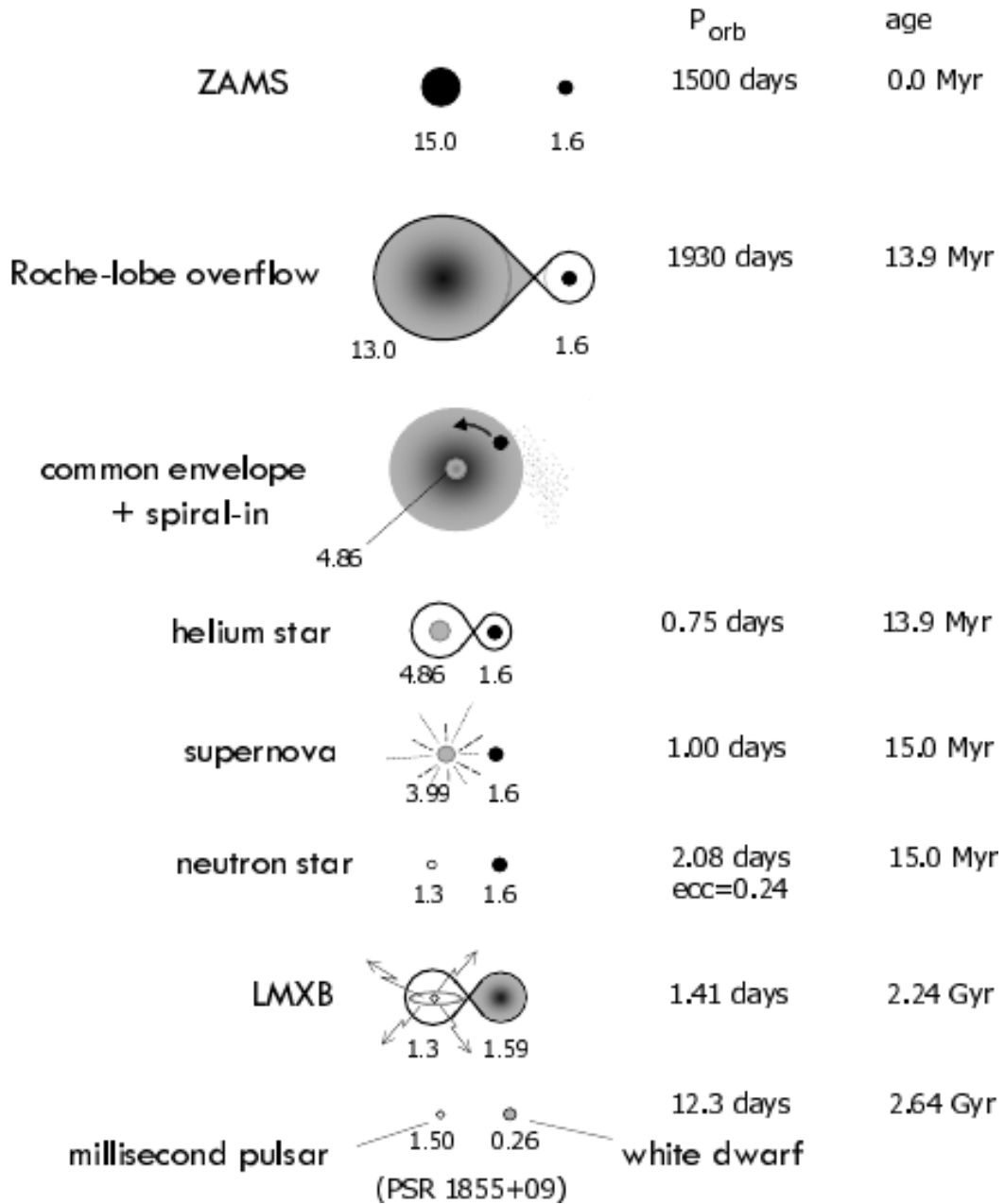


Figure 4.4: Illustration of the evolution of LMXB. The masses are typical start masses. In every step there is a transfer of matter. Parameters are given for a scenario leading to the formation of the observed binary millisecond pulsar PSR 1855+09. The stellar masses given in solar units (Lewin & van der Klis 2006)

### 4.3 Accretion

Accretion of matter is the main energy source of X-ray binaries. It is the most efficient way to convert kinetic energy into radiation, e.g., it is three orders of magnitude more efficient than the nuclear conversion from H to He. In the following the basics of accretion and the two types of accretion which are important for X-ray binaries will be discussed according to Longair (1994), Lewin et al. (1995) and Lewin & van der Klis (2006).

#### 4.3.1 Idea of Accretion

In general, accretion takes place onto compact objects, e.g., in binary systems like the systems discussed above. However, in the following the discussion is restricted to the case of a neutron star as the compact companion.

The energy output created by accretion can be calculated in a simple model by assuming a proton which falls from infinity onto the neutron star surface. The kinetic energy of the proton grows and its gravitational potential decreases the closer it gets to the compact object. Due to energy conservation this can be expressed by:

$$\frac{1}{2}m_p v_{\text{ff}}^2 = \frac{GMm_p}{r} \quad (4.2)$$

with  $m_p$  the mass of the proton,  $v_{\text{ff}}$  the free-fall velocity,  $G$  the gravitational constant<sup>2</sup>,  $M$  the mass of the compact object, and  $r$  the distance of the proton to the center of the neutron star.

At the surface of the star the proton is immediately stopped and, if there is no bounce back, its whole kinetic energy is converted into radiation. The total amount of the dissipated energy depends on the mass accretion rate  $\dot{m}_{\text{acc}}$  and the dissipation rate  $\frac{1}{2}\dot{m}_{\text{acc}}v_{\text{ff}}^2$ . With this definitions the luminosity can be written as:

$$L = \frac{1}{2}\dot{m}_{\text{acc}}v_{\text{ff}}^2 = \frac{GM\dot{m}_{\text{acc}}}{r} \quad (4.3)$$

With  $2GM/c^2$  as the Schwarzschild Radius  $r_g$  and  $R$  the radius of the compact object, the luminosity can be rewritten to:

$$L = \frac{1}{2}\dot{m}_{\text{acc}}c^2 \left( \frac{r_g}{R} \right) \Rightarrow L = \xi \dot{m}_{\text{acc}}c^2 \quad (4.4)$$

where the efficiency of mass to radiation conversion is defined as  $\xi = \frac{1}{2} \frac{r_g}{R}$ . This formula shows that for a bigger Schwarzschild radius, as well as for smaller radii  $R$  of the compact object the conversion is more efficient. A typical neutron star with  $M=1 M_{\odot}$  and a radius of  $R=15$  km has an efficiency of  $\sim 0.1$  compared to the nuclear conversion ( $\text{H} \rightarrow \text{He}$ ) with  $\xi = 7 \times 10^{-3}$ , accretion is a much more efficient process. Accretion onto a black hole is thought to be even more efficient. However, this is a complex problem. There is no solid surface..

#### 4.3.2 Eddington Luminosity

Although there seems to be no upper limit for the luminosity in formula 4.4, there is a physical limit. This has been calculated by Sir Arthur Eddington<sup>3</sup>. He assumed a spherically symmetric object on which accretion takes place, but at some value of the accretion rate the radiation pressure prevents the

<sup>2</sup> $G=6.67428(67) \cdot 10^{-8} \text{ cm}^3 \text{ g}^{-1} \text{ s}^{-2}$

<sup>3</sup>English astrophysicist (1882–1944)

matter from falling onto the object. The gravitational force can be calculated under the assumption of fully ionized infalling matter:

$$f_{\text{grav}} = \frac{GM}{r^2}(m_p + m_e) \approx \frac{GMm_p}{r^2} \quad (4.5)$$

The electron mass is negligible compared to the mass of the proton<sup>4</sup>. However, the electrons have to be considered to calculate the radiation pressure due to the Thomson Scattering<sup>5</sup>. Since protons are coupled electromagnetically with the electrons these assumptions are allowed. The radiation pressure acting on the electrons can be calculated by:

$$f_{\text{rad}} = \sigma_t \frac{L}{4\pi r^2 c} \quad (4.6)$$

Formula 4.5 and 4.6 leads to the Eddington luminosity:

$$L_E = \frac{4\pi GMm_p c}{\sigma_T} \quad (4.7)$$

Inserting the known constants the Eddington limit can be easily calculated for an object with known mass:

$$L_E = 1.3 \times 10^{38} \left( \frac{M}{M_\odot} \right) \text{ erg s}^{-1} \quad (4.8)$$

### 4.3.3 Roche lobe overflow - accretion discs

As seen above, at some point in the evolution of binary systems the normal companion star fills its Roche lobe and matter can be transferred by Roche lobe overflow via the inner lagrangian point. However, the accreting matter has typically a specific angular momentum  $J$  which prevents the matter from falling directly on the neutron star surface, an accretion disc is formed in which the matter can loose angular momentum. An accretion disc can be formed, if the size of the compact object is smaller than the circularization radius  $R_{\text{circ}} = J^2/GM$ . If there is no loss of angular momentum the matter will stay in this orbit for ever. However, friction provides the possibility to transport angular momentum in keplerian discs. In such discs the angular velocity is given by:

$$\omega(R) = \left( \frac{GM}{R} \right)^{1/2} \quad (4.9)$$

Due to this differential rotation, each annulus of the disc moves with a different angular velocities which leads to shearing between the annuli causing a torque between them. Angular momentum is transported outwards and matter inwards by this torque, thus an accretion disk can be formed.

The disc is in most cases geometrical thin (see Figure 4.5), what means that the height is much smaller than the radius. There are two main assumptions to be made to maintain the feature of thin discs:

- the mass of the matter in the disc has to be much smaller than the mass of the accreting star
- everywhere in the disc, the Kepler velocity  $\omega$  has to be higher than the local speed of sound  $c_s$

<sup>4</sup> $m_e \approx 511 \text{ keV} \ll m_p \approx 938 \text{ MeV}$

<sup>5</sup>Cross section for Thomson scattering:  $\sigma_T = 6.653 \times 10^{-29} \text{ m}^2$

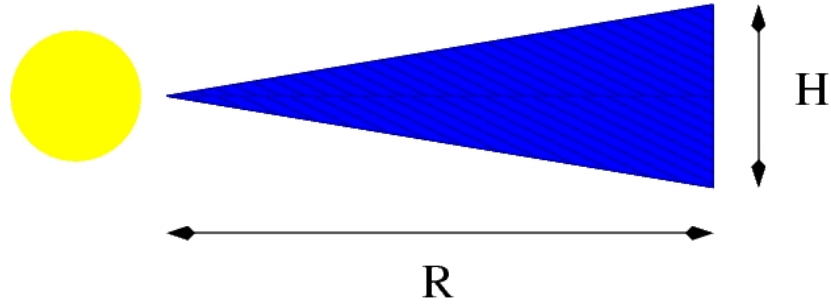


Figure 4.5: Illustration of a thin accretion disc

Under these assumptions the height  $H$  of the disc, depending on the radius  $R$ , can be calculated by the equation for hydrostatic support:

$$\frac{\partial p}{\partial z} = -\frac{GM_s \rho \sin \theta}{r^2} \quad (4.10)$$

From this the height can be determined by:

$$H \simeq \frac{c_s}{\omega} R \ll R \quad (4.11)$$

This geometry of the disc is valid far away from the central object. However, close to the accreting object its magnetic field  $B$  becomes important. The strength of the magnetic field at distance  $r$  can be calculated with  $B=(R_s/r)^3 B_s$  with  $B_s$  the magnetic field strength at the surface of the compact object at radius  $R_s$ . Thus the magnetic pressure on the matter is:

$$B \approx \left( \frac{B_s^2}{2\mu_0} \right) \left( \frac{R_s}{r} \right)^6 \quad (4.12)$$

But also the infalling matter puts pressure on the magnetic field which is known as *ram* pressure:

$$p_{\text{ram}} = \rho v^2 \quad (4.13)$$

The pressure of the infalling matter and the magnetic pressure cancel each other out at the Alfvén radius

$$r_M = \left( \frac{2\pi^2}{G\mu_0^2} \right)^{1/7} \left( \frac{B_s^4 R_s^{12}}{M_s \dot{m}} \right)^{1/7} \quad (4.14)$$

with  $\dot{m} = 4\pi r^2 \rho v$  the mass accretion rate. This will give for typical values of a neutron star with a magnetic field strength of  $B_s = 10^{12}$  Gauss an Alfvén radius in the order of 1 000 km which is 100 times larger than the radius of the neutron star. Hence, the surrounding area of the neutron star is magnetically dominated and the matter has to follow the magnetic field lines. Therefore the matter is accreted to the poles of the magnetic field and an accretion column is formed.

However, *LMXB* have typical magnetic fields in the range of  $10^6$ – $10^{10}$  Gauss, therefore the magnetosphere<sup>6</sup> shrinks. The accretion disk can extend down to the neutron star surface.

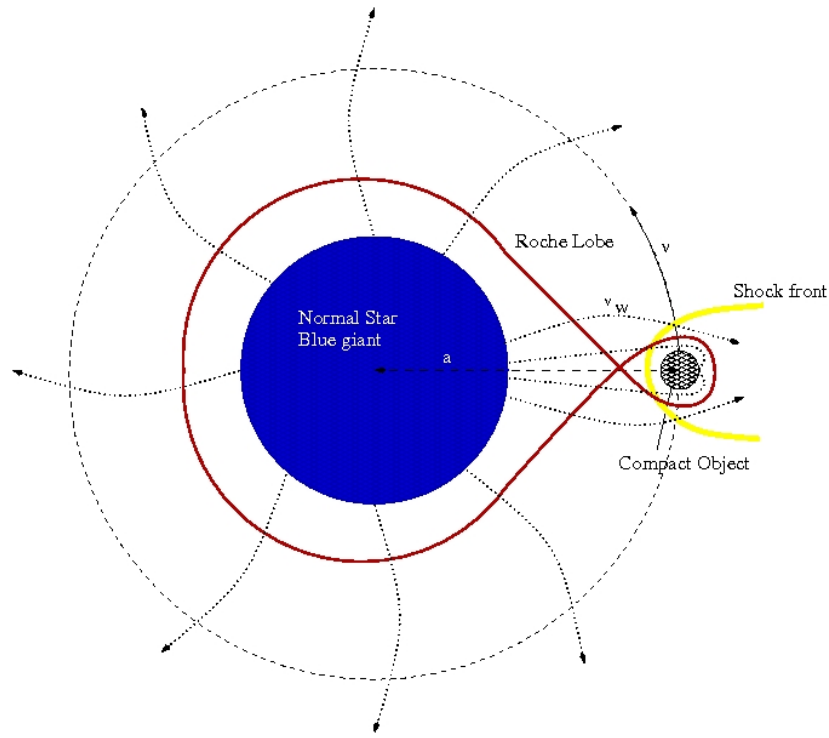


Figure 4.6: Illustration of the stellar wind and a compact object embedded in it. There are turbulences and a shock front in the region where the wind hits the magnetic field of the compact object, figure based on Longair (1994)

#### 4.3.4 Stellar wind Accretion

If Roche lobe overflow is not possible in a binary system there is also another possibility to transfer mass. Some kind of stars (luminous stars of spectral type O and B) have strong stellar winds from which matter can be accreted by the compact object (see Fig. 4.6). Obviously this is not a very efficient process because the matter is blown in all directions ( $\Omega = 4\pi$ ) and is not pointed towards the compact object. Therefore, only matter passing very close to the compact object can be accreted. The radius in which matter is captured and accreted onto the compact object can be calculated by:

$$r = \frac{2GM}{v_{\text{rel}}^2} \quad (4.15)$$

with  $v_{\text{rel}}^2 = v_{\text{w}}^2 + v^2$ . Typical velocities of stellar winds are about  $1-2 \times 10^3 \text{ km s}^{-1}$ . Defining the mass loss rate to  $\dot{M}_{\text{W}}$  and set  $a$  to the distance between the binary companions the accretion rate can be derived:

$$\dot{M} \sim \frac{\pi r^2}{\Omega a^2} \dot{M}_{\text{W}} \quad (4.16)$$

<sup>6</sup>The magnetosphere is determined by the Alfvén radius



## Chapter 5

# Properties of X-ray binaries

X-ray binaries emit radiation over the whole energy range, from radio waves via optical up to X - and  $\gamma$ - rays. Studying the properties of the produced spectrum, as well as the time behavior of radiation can help us to understand physics. In the following section spectral and timing properties and their possible origin will be discussed. But first an overview over some fundamental physical processes that generate X-rays will be given according to Longair and Rybicki & Lightman.

### 5.1 Origin of X-rays

X-ray photons originate in regions with temperatures above  $10^6$  K. Several mechanisms that can generate photons with such high energies exist. Some of them, especially the mechanisms important in *LMXB*, will be discussed in the following section.

#### 5.1.1 Blackbody radiation

Objects in thermal equilibrium emit a so-called blackbody spectrum. A blackbody is a theoretical object which absorbs all incident electromagnetic radiation and reflects none. Such an idealised object would radiated only due to its non-zero temperature.

A real object, for which thermal equilibrium can be assumed, is an optical thick element of a gas where a photon undergoes many interactions with the present electrons in situ. The energy of the photon is distributed uniformly and the object can be characterized by a single temperature which determines the emitted spectrum described by the Planck function:

$$B_\nu = \frac{2h\nu^3}{c^2} \frac{1}{\exp(h\nu/kT) - 1} \quad (5.1)$$

with  $h$  as the Planck's constant<sup>1</sup>,  $k$  as the Boltzman constant<sup>2</sup> and  $T$  as the temperature of the object. The characteristic spectrum for each temperature is shown in Figure 5.1. For higher temperatures the maximum of the intensity is shifted to higher frequencies (also shown in Figure 5.1 which can be calculated by  $\partial B_\nu / \partial \nu = 0$  which leads to the Wien displacement law:

$$\nu_{\max} = 5.88 \cdot 10^{10} \text{ T}^2 \text{ K}^{-1} \text{ Hz} \quad (5.2)$$

---

<sup>1</sup> $h = 4.13566733(10) \cdot 10^{-15} \text{ eV s}$

<sup>2</sup> $k = 8.617343(15) \cdot 10^{-5} \text{ eV/K}$

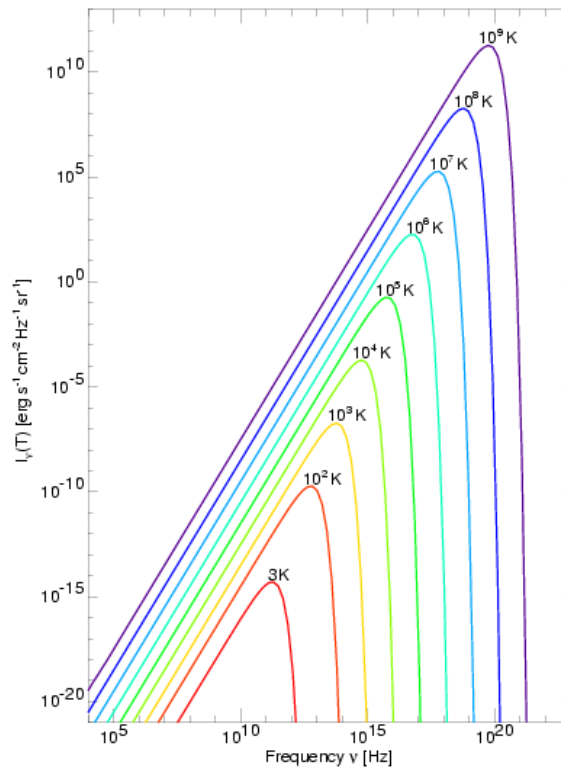


Figure 5.1: Blackbody spectra for different temperatures. On the y-axis the intensity is shown and on the x-axis the frequency, (J. Wilms)

It can be shown that the integral over the spectrum increases, as for higher temperatures more photons are produced.

### 5.1.2 Bremsstrahlung

A charged particle, e.g., an unbound electron, passing through, e.g., a gas, is accelerated by the Coulomb field of the present nuclei and ions, therefore the electron emits electromagnetic radiation. This free-free scattering process is called Bremsstrahlung. The emitted spectrum of thermal Bremsstrahlung depends on the density and on the temperature of the gas, as well as on the energy of the electrons, which is the maximal energy of the emitted photons. The spectrum is flat up to an cut-off frequency where it exponentially decreases:

$$I(E) = (kT)^{-1/2} \exp\left(-\frac{E_e}{kT}\right) \quad (5.3)$$

### 5.1.3 Synchrotron radiation

Charged particles (typically electrons) moving with a velocity  $\vec{v}$  through a magnetic field  $\vec{B}$  emit electromagnetic radiation. The electron is driven by the Lorentz force  $\vec{F} \propto \vec{v} \times \vec{B}$  into a motion perpendicular to the magnetic field and its flight direction, hence, the electron is accelerated. According

to Bremsstrahlung radiation with a characteristic frequency is emitted, depending on the  $\gamma$ -factor of the particle and the strength of the magnetic field:

$$\nu_c = \frac{1}{2\pi} \frac{eB}{m_e c} \left( \frac{E_{e^-}}{m_e c^2} \right)^2 \quad (5.4)$$

which can be written as:

$$\nu_c \approx 630 \text{ MHz} \left( \frac{B}{10^{-4} \text{ G}} \right) \cdot \left( \frac{E/m_e c^2}{10^3} \right)^2 \quad (5.5)$$

Relativistic electrons with  $\gamma \leq 100$  produces in a magnetic field above  $10^8$  G photons with X-ray energies.

### 5.1.4 Compton scattering

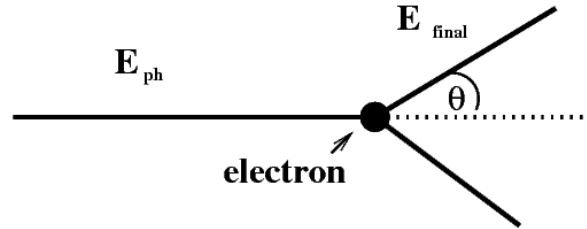


Figure 5.2: Schematic illustration of compton scattering in the reference frame of the electron

The scattering of a photon with initial energy  $E_{\text{ph}}$  with an electron at rest is called Compton scattering. Energy can be transferred from the photon to the electron like shown in figure 5.2. The resulting energy  $E_{\text{final}}$  of the photon depends on the angle under which the photon is scattered and on its initial energy:

$$E_{\text{final}} = \frac{E_{\text{ph}}}{1 + \frac{E_{\text{ph}}}{m_e c^2} (1 - \cos\theta)} \quad (5.6)$$

where  $m_e c^2$  is the rest mass energy of the electron (511 keV).

For non-relativistic energies of the photon,  $E/m_e c^2 \ll 1$ , Equation 5.6 can be rewritten as:

$$E_{\text{final}} \approx E_{\text{ph}} \left( 1 - \frac{E_{\text{ph}}}{m_e c^2} (1 - \cos\theta) \right) \quad (5.7)$$

However, if the electrons are not at rest, energy can be transferred from the electrons to the photons by inverse Compton scattering. In the rest frame of the electron the transferred energy can be calculated by:

$$E_{\text{final}} = \gamma E_{\text{ph}} \left( 1 + \frac{v}{c} \cos\theta \right) \quad (5.8)$$

where  $\gamma$  is  $\frac{E_e}{m_e c^2}$ .

What leads to a maximal final energy of the photons of:

$$E_{\text{final}} = 4\gamma^2 E_{\text{ph}} \quad (5.9)$$

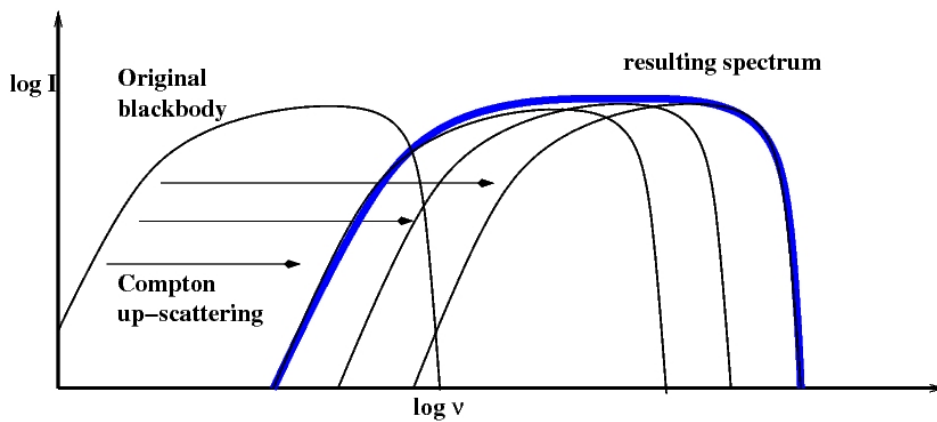


Figure 5.3: Spectrum of a comptonized blackbody spectrum (just schematic)

Therefore even optical photons with an energy of 1 eV can reach X-ray energies if they scatter with a bunch of GeV<sup>3</sup> electrons.

Comptonization is used to describe a spectrum of a X-ray source which is dominated by inverse Compton scattering. However, seed photons have to be provided by another mechanisms. In Figure 5.3 an example of a blackbody spectrum which is shifted to higher energies by Compton up scattering is shown.

### 5.1.5 Fluorescence

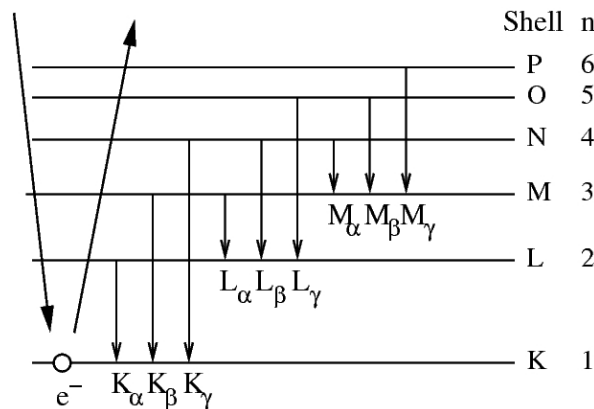


Figure 5.4: Possible transitions of electrons in the atomic shell (K. Freund)

A photon which impinges on atom can interact with the bound electrons in the atomic shell. If the photon energy exceeds the binding energy of the electron, the atom can be ionized. The energy states in an atomic shell are subdivided into shells which have different main quantum numbers  $n$  and therefore different binding energies. The shell with the highest binding energy is called K-shell with  $n=1$ , followed by the L-shell with  $n=2$ , and so on. Typically the photon interacts with an electron of

<sup>3</sup>GeV means  $10^9$  eV, which are common in cosmic rays

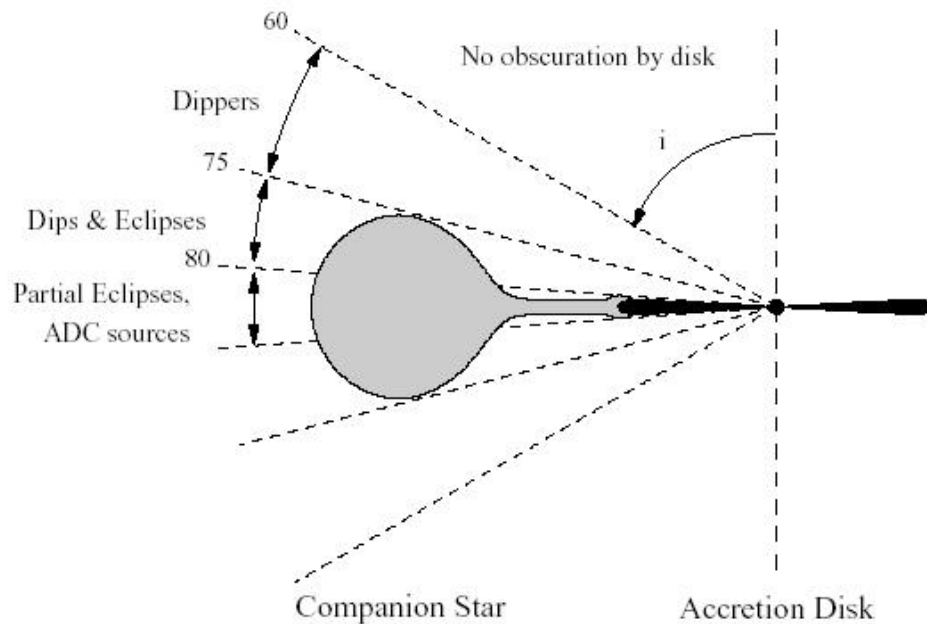


Figure 5.5: Dips and Eclipses at different inclination angles, after [Seward & Charles \(1995\)](#)

the the K-shell, the resulting hole is filled by an electron of a higher shell. The excessive energy of the electrons is released by a so-called fluorescent photon which is named after the state it occupies after the transition has taken place, see Figure 5.4.

## 5.2 Timing properties

X-ray binaries show variabilities from small timescales in the ms range up to large timescales in the order of hours to days. Studying these time properties provides the ability to constrain parameters of the system and its companions, e.g., the masses and orbital periods. However, the lightcurves of X-ray binaries depend very strongly on the angle under which the system is observed.

- **Dips and eclipses**

The compact object can be observed unobscured if the inclination angle is below  $\sim 60^\circ$  (see Figure 5.5). Above that angle the object can be obscured by thickened regions in the accretion disc. This will cause dips, in which the detected countrate of the central object decreases. Such thickened regions are formed at the point where the infalling matter hits the disc.

For nearly edge-on observations the companion star leads to variations in the lightcurve, creating dips and eclipses, from which the orbital period of the binary system can be determined. For *LMXB* the orbital periods range from the order of minutes to the order of ten days and for *HMXB* the period is in the order of days to the order of ten days.

- **Pulsations**

A temporal feature of the lightcurve which is not caused by the observation angle are pulsations. They originate from highly magnetized neutron stars which accrete matter in a column at the magnetic poles (as discussed in Section 4.3.3). However, if the rotational axis and the magnetic

dipole axis are misaligned, pulsations can be observed. Typical periods are in the order of some seconds, but also ms pulsars have been observed. Although most of the pulsars are high mass X-ray binaries, because they are young objects with a high magnetic field, millisecond pulsars seem to have their origin in low mass X-ray binaries.

- **Bursts**

Although accretion is much more efficient than nuclear fusion, also fusion leads to observable features in the lightcurve. Fusion is ignited by the pile-up of accreted hydrogen and helium on the neutron star surface. At some point the density and the temperature exceeds the threshold for fusion and hydrogen burning via the CNO-cycle is ignited. However, this process is unstable for low mass accretion rates and will lead to a thermonuclear flash, which is seen as a burst in the luminosity. In *LMXB* with higher accretion rates the hydrogen burning is stable and even helium burning is possible, cause burning of hydrogen is faster, bursts can still occur. For high mass accretion rates, hydrogen and helium burning is stable, thus no bursts occur.

Bursts occur when enough material has been accumulated on the neutron star surface to ignite fusion, which is reached typically in several days. The burst itself lasts typically up to ten seconds, however a 'superburst' which lasted  $\sim 3$  hours have been observed in the *LMXB* 4U 1820-30 by [Strohmayer & Brown \(2002\)](#).

Another feature called kilohertz Quasi Periodic Oscillations (*kHz QPOs*) will be described in detail in the next chapter.

Table 5.1: Properties of *LMXB* and *HMXB* ([Lewin & van der Klis 2006](#))

	<i>HMXB</i>	<i>LMXB</i>
X-ray spectra:	$kT \geq 15$ keV (hard)	$kT \leq 10$ keV (soft)
type of time variability:	regular X-ray pulsations no X-ray bursts	only a very few pulsars often X-ray bursts
Accretion process	wind	Roche-lobe overflow
Timescale of accretion	$10^5$ yr	$10^7$ – $10^9$ yr
Accreting compact star:	high B-field NS (or BH)	low B-field NS (or BH)
Spatial Distribution:	Galactic plane	Galactic center and spread around the plane
Stellar population:	young, age $< 10^7$ yr	old, age $> 10^9$ yr
Companion stars:	luminous, $L_{\text{opt}}/L_x > 1$ early type O(B)-stars $> 10 M_{\odot}$ (Pop. I)	faint, $L_{\text{opt}}/L_x \ll 0.1$ blue optical counterparts $\leq 1 M_{\odot}$ (Pop. I and II)

### 5.3 Spectral properties of *HMXB*

The optical emission of *HMXB* is dominated by the normal star which emits a blackbody spectrum with absorption lines, which are typically broadened due to the high rotational velocity. The temperature of the star depends on its spectral type, *O* stars with masses up to  $60 M_{\odot}$  have temperatures of 30 000 up to 50 000 K and *B* stars with  $M \leq 18 M_{\odot}$  have temperatures in the range of 10 000–28 000 K.

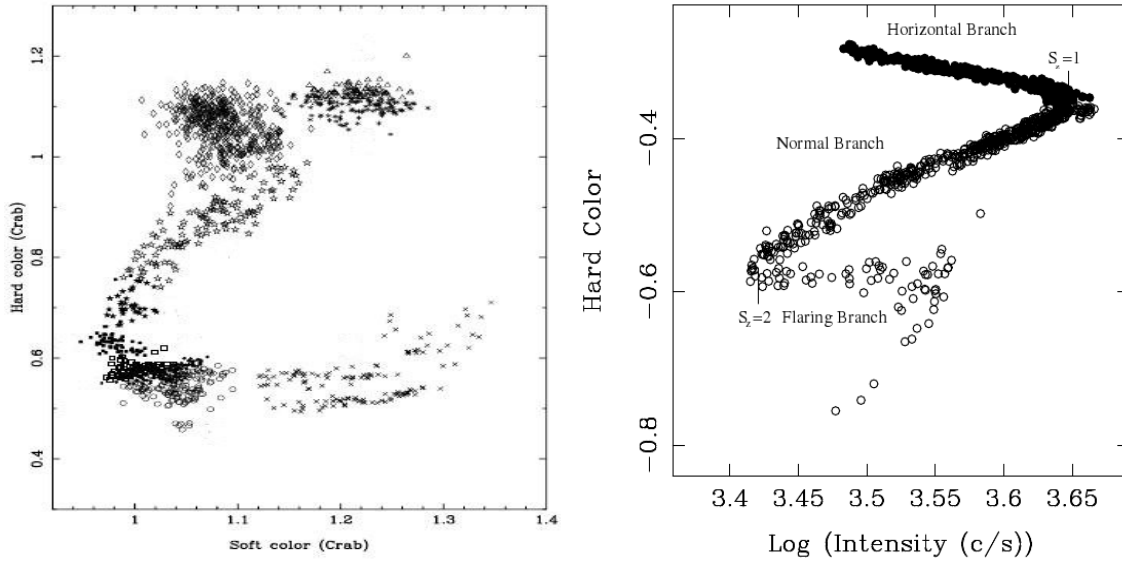


Figure 5.6: Color-color diagram of the Atoll source 4U 1608-52 (van Straaten et al. 2003) on the left side, and GX 340+0 (Jonker et al. 2000) as an example for a Z-source

Typical optical luminosities of *HMXB* are  $L_{\text{opt}} > 10^5 L_{\odot}$  which exceeds the X-ray luminosity of the compact object and leads to  $L_{\text{opt}}/L_X > 1$ .

The spectrum emitted by the neutron star follows a power law with an typical index of -1.0–2.0 and a high-energy cut-off between 10–25 keV. The photons are produced at the surface of the neutron star by bremsstrahlung and scattered to higher energies by compton scattering.

Due to the typical high magnetic field of a *HMXB* the kinetic energy of the plasma electrons is quantized in Landau-levels with an energy spacing of  $E_c$ . Hence, resonant scatterings between photons with energies  $E_{\text{ph}} \sim nE_c$  ( $n=1, 2, 3, \dots$ ) and the Landau electrons can occur. Cyclotron lines at energies close to the Landau-levels are observed, for the first time in Hercules X-1 by Truemper et al. (1978). Hence, *LMXB* are the topic of this thesis, just the basic properties of *HMXB* has been discussed here. A detailed overview was given by, e.g., White et al. (1995).

## 5.4 Spectral properties of LMXB

Hasinger & van der Klis (1989) classified *LMXB* after their track in color-color diagrams (*CD*)<sup>4</sup> shown in Figure 5.6. The tracks are shown in Figure 5.6, which give an indication of their names, sources with tracks in the *CD* shown on the left side of Figure 5.6 are called Atoll sources, whereas sources with a *CD* like on the right side are called Z-sources. Their main differences are their X-ray luminosities, Atoll sources are faint sources with  $L_x \sim 0.01\text{--}0.1 L_{\text{Edd}}$  and Z-sources have typical luminosities of  $L_x \sim 0.1\text{--}1.0 L_{\text{Edd}}$  which leads to ratios  $L_{\text{opt}}/L_x$  below 0.1.

The spectral shape of all *LMXB* sources can be described very well by a power law with an exponential cut off:

$$N_{\text{ph}} \propto E^{-\Gamma} \exp\left(-\frac{E}{E_{\text{cutoff}}}\right) \quad (5.10)$$

<sup>4</sup>In a *CD* the count ratio of an upper X-ray energy band is plotted over the count ratio of a lower X-ray energy band

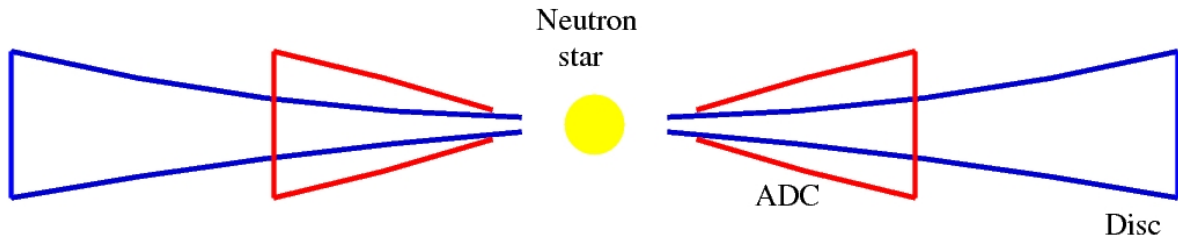


Figure 5.7: Geometry of an *LMXB* showing the extended accretion disc corona above a thin accretion disc, after Church & Bałucińska-Church (2004)

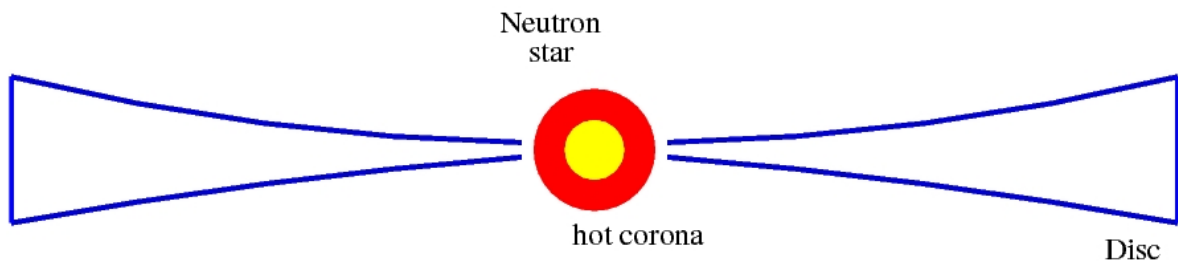


Figure 5.8: Geometry of an *LMXB* showing the hot plasma close to the neutron star where the photons are comptonized, after Church & Bałucińska-Church (2004)

with  $N_{\text{ph}}$  the photon flux<sup>5</sup>,  $\Gamma$  as the power law index with values between 0.00–2.00 and  $E_{\text{cutoff}}$  the cut-off energy which is in the range of 1–20 keV.

However, the correct composition of the spectrum is not yet clarified. Two different models for the description of the Z-sources behavior, the Western and the Eastern model, exist.

#### 5.4.1 Western model - Birmingham model

White et al. (1988) proposed a blackbody spectrum from the neutron star which is scattered to higher energies by compton scattering in the hotter inner regions of the disc around the central object to describe the spectral shape. The maximal photon energy is related to the energies of the electrons in this regions. Due to the fact that just a spectrum up to 30 keV can be described by this model, another component is needed to explain the hard tail up to 100 keV. To solve this problem Church & Balucinska-Church (1995) proposed a comptonized emission from an extended accretion disc corona (ADC), which is shown in Figure 5.7. Studies by Church & Bałucińska-Church (2001) showed that the region where comptonization takes place has typical sizes of up to 50 000 km. Further Church & Bałucińska-Church (2004) showed that X-rays from the neutron star irradiate the disc and therefore a highly extended corona can be formed.

#### 5.4.2 Eastern model

In contrast to the Western model Mitsuda et al. (1984, 1989) interpreted the spectrum as a multicolor blackbody radiation from the disc and a single blackbody from the neutron star surface. The blackbody

<sup>5</sup>photons per unit area, unit time and per keV

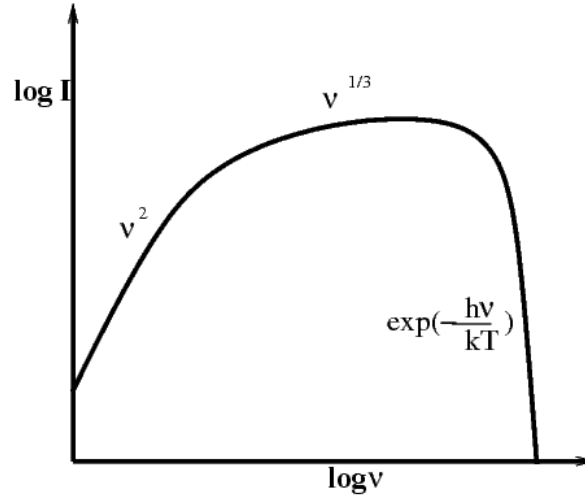


Figure 5.9: Emission spectrum of a geometrical thin accretion disk(just schematic)

radiation comptonized in an optical thin corona of hot plasma, which is placed in a small central region around the neutron star with typical sizes of less than 100 km (see Figure 5.8). The multicolor blackbody spectrum originates from an optical thick accretion disc, thus thermal equilibrium can be assumed. The dissipated radiation can be expressed by the Stefan-Boltzmann law:

$$j = \sigma T^4 \quad (5.11)$$

which describes the radiated energy per unit surface area and unit time, with  $\sigma$  as the Stefan-Boltzmann constant<sup>6</sup>. The luminosity of an annulus from  $r$  to  $r+\Delta r$  is determined by

$$L = 2\sigma T^4 \times 2\pi r \Delta r \quad (5.12)$$

This leads to an expression for the temperature structure of the disc:

$$T = \left( \frac{3G\dot{m}M}{8\pi r^3 \sigma} \right)^{1/4} \quad (5.13)$$

where  $G$  is the gravitational constant,  $M$  is the mass of the compact object and  $\dot{m}$  is the mass accretion rate. This equation shows that the temperature of the disc increases towards the centre with  $r^{-3/4}$ . Therefore the disc can be separated into annuli with different temperatures, each emitting a blackbody spectrum. The total intensity can be written with help of the Planck formula 5.1 as:

$$I(\nu) \propto \int_{r_1}^{r_{\max}} 2\pi r B(\nu, T(r)) dr \quad (5.14)$$

which can be simplified to a qualitative expression of  $I(\nu) \propto \nu^{1/3}$  lead to a spectrum of a geometrical thin accretion disc shown in Figure 5.9. In the cooler outer regions of the accretion disc optical photons are emitted whereas close to the neutron star X-rays are emitted.

<sup>6</sup> $\sigma = 5.670400(40) \times 10^{-5} \text{ erg cm}^{-2} \text{ s}^{-1} \text{ K}^{-4}$

### 5.4.3 Powerlaw and reflection component

The complex X-ray spectrum of *LMXB* is completed by a power-law component with  $\alpha$  as the power-law index and a reflection component, e.g., see [Di Salvo et al. \(2006\)](#), and references therein). There are some atoll sources with hard X-ray components up to several hundred keV. This spectrum follows a power law with an index of  $-\alpha$  where  $\alpha$  is in the range of 1.5–2.5 and an exponential cut off above  $\sim 20$  keV. In some *LMXB* no cut off have been seen up to 200 keV, e.g., in 4U 0614+091 ([Piraino et al. 1999](#)). The hard power law is assumed to be produced by thermal Comptonization of soft photons in a hot electron gas which is placed close to the neutron star, e.g., in a corona. However, to explain the energies up to  $\sim 100$  keV very high electron temperatures are necessary. Another possibility is the presence of a jet in which Comptonisation with high-velocity electrons can take place, jets and other alternative models are summarized in [Di Salvo & Stella \(2002\)](#), and references therein).

A reflection component was detected in some Atoll sources (e.g. [Piraino et al. \(1999\)](#)). This Compton reflection occurs when X-rays interact with a cold medium, e.g., the outer parts of the optically thick accretion disc. The typical shape is produced by photoelectric absorption at low energies and Compton scattering at high energies. A broad hump around 30 keV occurs. A detailed discussion is given by, e.g., [Lightman & White \(1988\)](#).

## Chapter 6

# Broad iron lines and quasi periodic oscillations

The first detection of a broad iron line was made with *EXOSAT* (White et al. 1986) and the first kilohertz quasi periodic oscillations (*kHz QPOs*) have been measured in 1996 by *RXTE* (van der Klis et al. 1996).

As we will see in the chapter the simultaneous measurement of a broad iron line and *kHz QPOs* provides the possibility to constrain the mass and the radius of the central neutron star in an X-ray binary. The mass-radius ratio of a neutron star can be used to probe different equation of states for dense matters shown in Figure 6.1. A detailed discussion was given by, e.g., Lattimer & Prakash (2001) and Haensel (2003).

Both features, broad iron line and *kHz QPOs*, are produced by relativistic effects next to the compact object. General relativity has to be taken into account for systems with neutron stars. For a typical neutron star with  $1.4 M_{\odot}$  the Schwarzschild radius  $r_s = 2GM/c^2$  is  $\sim 4$  km which is just a little bit smaller than the radius of the neutron star ( $r_{NS} = 10$  km).

In this chapter an overview over broad iron lines in *LMXB* and their broadening mechanisms will be given. Further the origin and the properties of *kHz QPOs* will be discussed in detail in this chapter.

### 6.1 Broad iron lines

Broad iron lines are assumed to have their origin in the inner regions of an accretion disc. The shape of the line depends strongly on the distance from the emitting region to the central object and the inclination under which the system is observed. A table of all *LMXB* in which broad iron lines have been observed is given in Table 6.1.1, and the formation mechanisms will be discussed according to Fabian et al. (2000) and Fabian (2006).

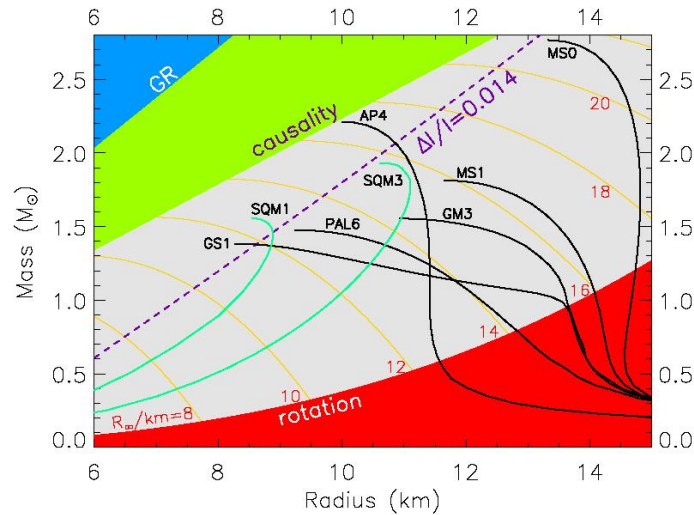


Figure 6.1: Mass-Radius curves for different equation of states for neutron stars. Illustration based on [Lattimer & Prakash \(2001\)](#)

### 6.1.1 List of all observed broad iron line in *LMXB*

An review of broad iron lines in *LMXB* was given by [Asai et al. \(2000\)](#), however, up to now there have been reported only six *LMXB* showing relativistic broadened iron lines.

Table 6.1: Low mass X-ray binaries with a relativistic broad iron line. The best-fit parameters are given reported in the denoted references.

Source	Line energy in keV	Inner Radius in $GM/c^2$	Inclination	Reference
Serpens X-1	6.83	7.7	$26^\circ$	<a href="#">Cackett et al. (2008)</a>
4U 1820-303	6.97	6.7	$19^\circ$	<a href="#">Cackett et al. (2008)</a>
GX 349+2	6.97	8.0	$23^\circ$	<a href="#">Cackett et al. (2008)</a>
4U 1636-536	6.43	6.3	$81^\circ$	<a href="#">Pandel et al. (2008, 3rd obs.)</a>
SAX J1808.4-3658	6.4	13.0	$59^\circ$	<a href="#">Cackett et al. (2009, XMM data)</a>
4U 1705-44	6.7	8.1	$28^\circ$	<a href="#">Piraino et al. (2007)</a>

### 6.1.2 Mechanism of broadening

Fluorescent iron lines are produced in an accretion disc which is irradiated by X-rays from the neutron star. The photons can be absorbed by atoms in the disc and an electron of the K-shell is ejected. The resulting hole is filled by an electron of the L-shell which leads to the most prominent fluorescent line, the iron  $K_\alpha$  line, with energies in the range between 6.4–6.97 keV. The exact line energy depends on the ionization level of the atom, since in an ionized atom the nucleus charge acts

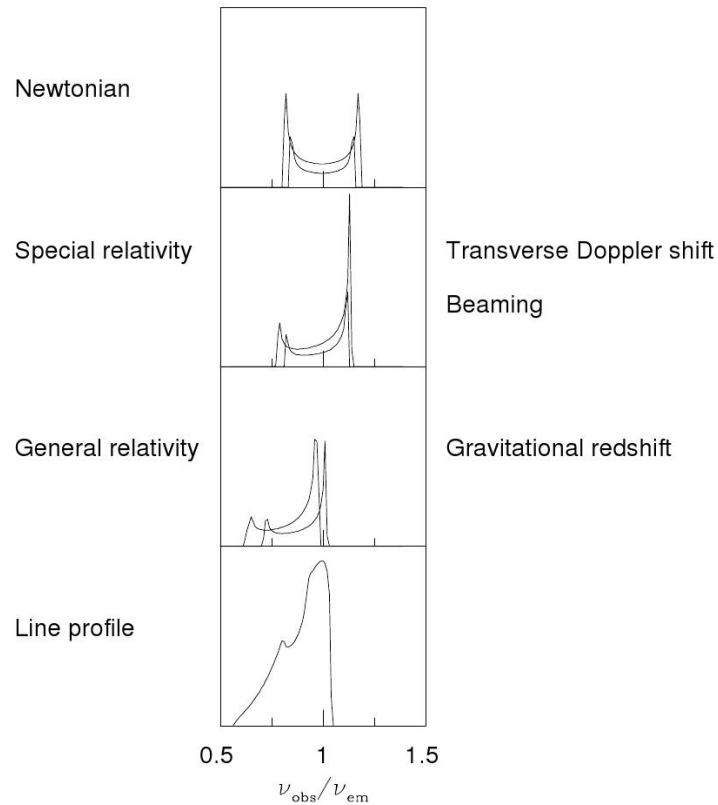


Figure 6.2: Profile of a broadened iron line. The contributions of the different effects are illustrated (Fabian et al. 2000)

on fewer electrons in the atomic shell, thus, the binding energy increases for each electron, especially in the lower shells. Therefore measurements of the line provides also an indirect measurement of the disc temperature.

In Figure 6.2 the contribution of the different broadening mechanisms are summarized. In the upper panel the effect of a rotating newtonian disc is shown. A double peaked line profile is emitted at each annulus of the disc, the approaching part of the disc emits higher energetic photons (blue-shifted) and the receding part emits lower energetic photons (red-shifted) due to the Doppler effect. Close to the compact object the disc rotates with the highest velocities which leads to the broadest line profile.

The inner boundary layer of a *LMXB* accretion disc can extend close to the surface of the compact object. Thus, emission of the iron fluorescence line can take place just a few gravitational radii<sup>1</sup> away from the compact object where gravitational effects become important. The line profile is modified by gravitational redshift and transverse Doppler shift (second and third panel of Figure 6.2). The whole profile is shifted to lower energies by transverse Doppler shift which can be explained by the fact that moving clocks run slower. Due to the high velocities close to the neutron star, time dilation must be

<sup>1</sup>The gravitational radius is defined as  $r_g = GM/c^2$

taken into account. This special relativity effect can be expressed by:

$$\Delta t' = \gamma \Delta t = \frac{\Delta t}{\sqrt{1 - v^2/c^2}} \quad (6.1)$$

with  $v$  as the velocity of the matter and  $c$  as the speed of light.

The emitted wavelengths seem to be longer and therefore the frequency of the emitted photon is lower than the frequency of a photon emitted at rest.

An additional shift to lower energies is caused by a similar effect, the gravitational redshift. This results, equivalent to the transverse Doppler shift out of the fact that clocks near big masses run slower.

The blue part of the line profile is enhanced by relativistic beaming, in which the radiation is pointed into the direction of the motion of the emitting matter.

The lowest panel of Figure 6.2 shows the resulting profile including all effects. The inclination angle under which the system is observed determines the maximal observable energy. The angle is also important for effects resulting from relativistic beaming and light bending.

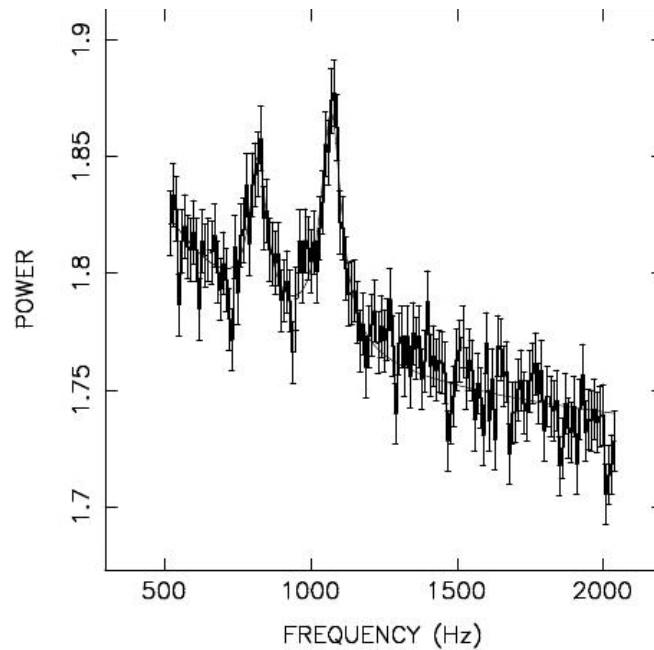


Figure 6.3: The first detection of a *kHz* QPOs by [van der Klis et al. \(1996\)](#) in Sco X-1

## 6.2 kilohertz Quasi Periodic Oscillations

The fastest variable component in the lightcurve of *LMXB* are *kHz* QPOs, which have been observed in the *LMXB* listed in Table 6.2.2. *kHz* QPOs also seem to have their origin in the accretion disc around neutron stars. To understand *kHz* QPOs the orbital motion around a compact object has to be studied. Possible mechanisms which produce *kHz* QPOs are discussed according to van der Klis in [Lewin & van der Klis \(2006\)](#).

### 6.2.1 Detection of *kHz* QPOs

*kHz* QPOs can be detected in a Fourier transformation of an observed X-ray photon flux with a time resolution of below 1 ms. In the transformed spectra which is also called Power Spectral Density (PSD), the contribution of each frequency to the time variability of the source is shown, e.g., the PSD of Sco X-1 in Figure 6.3.

The peak can be fitted with a lorentzian profile with centroid frequency  $\nu_0$  and the full width at half maximum (FWHM)  $\lambda$ . The quality factor  $Q = \nu_0/\lambda$  distinguishes between a real *kHz* QPOs ( $Q > 2$ ) and a peaked noise ( $Q < 2$ ). The higher the quality factor the sharper the line.

The strength of the signal is expressed by the root mean square amplitude which describes the amplitude of the signal as a fraction of the total source flux. The PSD can be normalized in different ways, where one of the most commonly used for *kHz* QPOs is the normalization after [Leahy et al. \(1983\)](#), which will also be used in this thesis. In this normalization the square of the fourier coefficient of each frequency is divided by the total number of photons. The power is given as the squared root mean squared variability per frequency interval and therefore the Poisson noise level is 2. A detailed discussion is given by, e.g., [Pottschmidt \(2002\)](#). In the example Sco X-1 [van der Klis et al.](#) reported a lower *kHz* QPOs with a frequency of  $\sim 800$  Hz with a FWHM varying between 50 and 100 Hz

and an rms amplitude of 0.9%–1.2%. The higher frequency has been measured to  $\sim 1\,000$  Hz with a Quality factor up to 100 and an rms amplitude of also 0.9%–1.2%. The discrepancy of the power to the expected value due to Leahy normalization is caused by deadtime of the detector.

## 6.2.2 List of all observed QPOs in LMXRBs

Table 6.2: Low mass X-ray binaries with quasi periodic oscillations after [Lewin & van der Klis \(2006\)](#), and references therein). Only the highest simultaneous observed values will be given, because therefore a limit of for the radius can be given.

Name of the source	High frequency	Low frequency	References
XTE J1807–294	563.6 Hz	359.9 Hz	<a href="#">Linares et al. (2005)</a>
SAX J1808.4–3658	$\Delta\nu = 195$ Hz		<a href="#">Wijnands &amp; van der Klis (1998)</a>
Sco X-1(1617–155)	1080 Hz	833 Hz	<a href="#">van der Klis et al. (1996)</a>
GX 340+0 (1642–455)	753 Hz	452 Hz	<a href="#">Jonker et al. (1998)</a>
GX 349+2 (1702–363)	978 Hz	712 Hz	<a href="#">Zhang et al. (1998b)</a>
GX 5–1 (1758–250)	856 Hz	557 Hz	<a href="#">Wijnands et al. (1998b)</a>
GX 17+2 (1813–140)	1087 Hz	781 Hz	<a href="#">Wijnands et al. (1997a)</a>
Cyg X-2 (2142+380)	862 Hz	516 Hz	<a href="#">Wijnands et al. (1998a)</a>
4U 0614+09	858 Hz	549 Hz	<a href="#">Ford et al. (1997a)</a>
2S 0918–549	single kHz QPOs: 1156 Hz		<a href="#">Jonker et al. (2001)</a>
4U 1608–52	1100 Hz	600–900 Hz	<a href="#">Mendez et al. (1998)</a>
4U 1636–53	1150–1193 Hz	890–920 Hz	<a href="#">Wijnands et al. (1997b)</a>
4U 1702–43	$\sim 900$ Hz	$\sim 567$ Hz	<a href="#">Markwardt et al. (1999)</a>
4U 1705–44	1073 Hz	770–870 Hz	<a href="#">Ford et al. (1998a)</a>
4U 1728–34	1284 Hz	895 Hz	<a href="#">Méndez &amp; van der Klis (1999)</a> and <a href="#">Piraino et al. (2000)</a>
KS 1731–260	1176 Hz	900 Hz	<a href="#">Wijnands &amp; van der Klis (1997)</a>
4U 1735–44	982–1026 Hz	632–729 Hz	<a href="#">Ford et al. (1998b)</a>
SAX J1750.8–2900	1253 Hz	936 Hz	<a href="#">Kaaret et al. (2002)</a>
4U 1820–303	1060 Hz	800 Hz	<a href="#">Zhang et al. (1998a)</a>
Aql X-1 (1908+005)	1083 Hz	803 Hz	<a href="#">Barret et al. (2008)</a>
4U 1915–05			
XTE J2123–058	1129 Hz	853 Hz	<a href="#">Homan et al. (1999)</a>

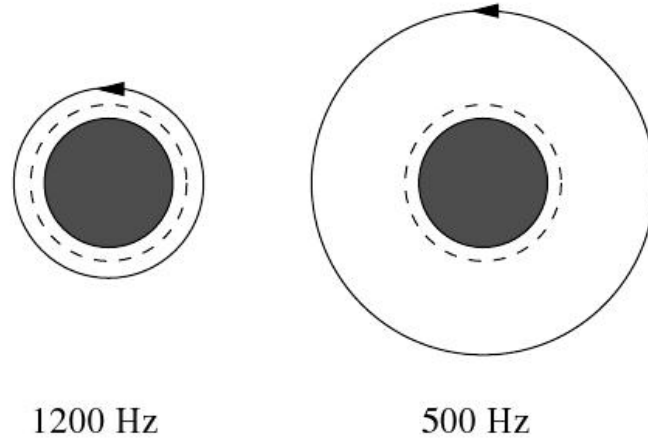


Figure 6.4: A 10-km radius,  $1.4M_{\odot}$  neutron star with the corresponding innermost stable circular orbit (ISCO; dashed circles) and orbits (drawn circles) corresponding to orbital frequencies of 1200 and 500 Hz, drawn to scale (Lewin & van der Klis 2006)

### 6.2.3 Orbital motion

Assuming classical physics, a free particle rotates around an object in keplerian orbits (illustrated in Figure 6.4). The frequencies of these orbits can be calculated by:

$$\nu_K = \frac{\sqrt{GM/r^3}}{2\pi} \approx 1184 \text{ Hz} \left( \frac{r}{15 \text{ km}} \right)^{-3/2} m_{1.4}^{1/2} \quad (6.2)$$

with  $m_{1.4}$  the mass of the compact object in units of  $1.4 M_{\odot}$  and  $r$  the orbital radius.

Close to the compact object general relativity has to be taken into account. The environment is described, in the case of a non-rotating central object, by the Schwarzschild metric. For a spinning mass, the spacetime around an object can be described by the Kerr metric with  $j = Jc/GM^2$  as the Kerr-angular momentum parameter. In neutron stars with a typical spin period of 300 Hz,  $j$  would be smaller than 0.3, thus, the errors caused by frame dragging are much less than 10% (Miller et al. 1998). The Schwarzschild metric can still be used.

In general relativity the orbits are not closed, hence, there are the azimuthal (orbital) frequency  $\nu_{\phi}$  and in addition to that a radial pointing oscillation occurs with frequency  $\nu_r$ , and a vertical oscillation with frequency  $\nu_{\theta}$  occurs. This leads to a periastron precession with a frequency of

$$\nu_{\text{peri}} = \nu_{\phi} - \nu_r \quad (6.3)$$

as well as a nodal precession for which the frequency can be expressed by:

$$\nu_{\text{nodal}} = \nu_{\phi} - \nu_{\theta} \quad (6.4)$$

In Kerr spacetime the orbital frequency can be calculated by:

$$\nu_{\phi} = \nu_K \left( 1 + j \left( \frac{r_g}{r} \right)^{3/2} \right)^{-1} \quad (6.5)$$

where  $r_g = GM/c^2$  is the gravitational radius.

The radial and vertical frequency can be expressed by:

$$\nu_r = \nu_\phi \left( 1 - 6 \left( \frac{r_g}{r} \right) + 8j \left( \frac{r_g}{r} \right)^{3/2} - 3j^2 \left( \frac{r_g}{r} \right)^2 \right)^{1/2} \quad (6.6)$$

$$\nu_\theta = \nu_\phi \left( 1 - 4j \left( \frac{r_g}{r} \right)^{3/2} + 3j^2 \left( \frac{r_g}{r} \right)^2 \right)^{1/2} \quad (6.7)$$

Since for a non-rotating ( $j=0$ ) neutron star, the Schwarzschild metric can be used, the azimuthal frequency  $\nu_\phi$  is identical to the keplerian frequency  $\nu_K$  and therefore equations 6.6 and 6.7 simplify to:

$$\nu_r = \nu_\phi \left( 1 - 6 \left( \frac{r_g}{r} \right) \right)^{1/2} \quad (6.8)$$

No nodal precession occurs since it results out of frame dragging of a spinning object.

Close to a compact object with mass  $M$ , a particle cannot have a stable orbital motion due to effects of general relativity. However, there is an innermost stable circular orbit (ISCO) which can be determined in the Schwarzschild metric by:

$$R_{\text{ISCO}} = \frac{6GM}{c^2} \quad (6.9)$$

Matter circulating at the ISCO have the maximal orbital frequency which is expressed by:

$$\nu_{\text{ISCO}} = \frac{c^3}{2\pi 6^{3/2} GM} \approx \frac{1566}{m_{1.4}} \text{ Hz} \quad (6.10)$$

Observing *kHz QPOs* with such frequencies allows to constrain the radius and the mass of the neutron star. Since the radius has to be smaller than  $R_{\text{ISCO}}$ , an upper limit can be given. In the same way the mass limit can be determined with the help of equation 6.9 for the ISCO radius.

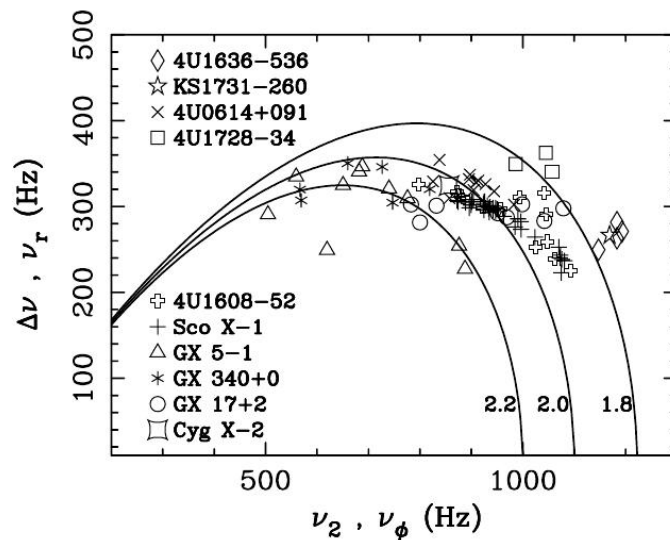


Figure 6.5: kHz QPOs frequency difference versus the higher frequency for ten LMXB with plotted frequencies for models with  $2.2 M_{\odot}$ ,  $2 M_{\odot}$  and  $1.8 M_{\odot}$  (Stella & Vietri 1999)

## 6.2.4 Models of kHz QPOs

The origin of kHz QPOs is not yet clarified. Different models have been developed to explain them. Since typically two frequencies are observed, the models have also to predict their occurrence.

- **Relativistic precession models**

Stella & Vietri (1998, 1999) proposed that all observed frequencies originate from the motion of matter around a neutron star. Inhomogeneities in the disc close to the ISCO form clumps with inclined and eccentric orbits. The Keplerian motion  $v_{\phi}$  of these clumps in the disc is associated with the higher kHz QPOs frequency  $\nu_2$ . The lower frequency  $\nu_1$  is assumed to originate from the periastron precession with frequency  $\nu_{\text{peri}}$ . This leads, with equation 6.3, to a  $\Delta\nu$  of  $\nu_2 - \nu_1 = \nu_r$ . In figure 6.5 the radial frequency versus the Keplerian frequency for three different neutron star masses are plotted, additionally the measured frequencies of ten LMXBs are shown. The observations are in best agreement with the model assuming a neutron star mass of  $2 M_{\odot}$  which is higher than predicted for most neutron stars. There is also no explanation for X-ray modulations which are observed.

- **Relativistic resonance models**

Kluźniak & Abramowicz (2001); Abramowicz & Kluźniak (2001) suggest resonances between the radial epicyclic motion and the orbital motion to produce kHz QPOs. The epicyclic motion is inharmonic and so a 1:2 or 1:3 resonance can occur due to effects of general relativity. The resonances can occur at particular radii in the disc shown in Figure 6.6. However, it is not yet clarified when and why such resonances occur.

- **Beat frequency models**

Although the beat frequency model was proposed by Lamb et al. (1985); Alpar & Shaham (1985) originally for low frequency QPOs, Strohmayer et al. (1996); Ford et al. (1997b) suggested to use this model also for kHz QPOs. This model provides explanations for almost all

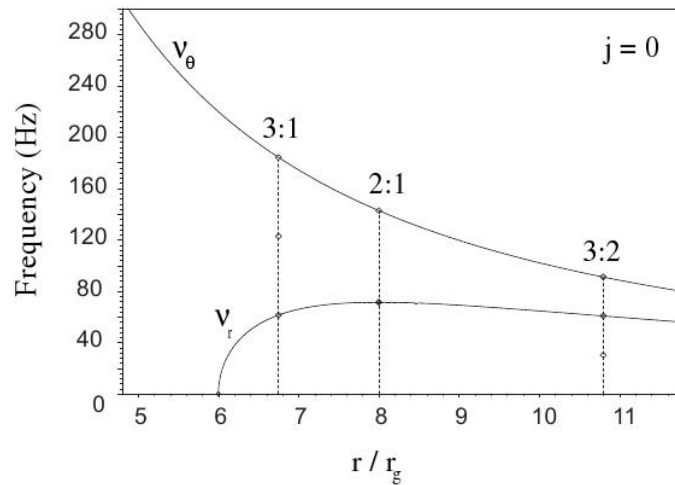


Figure 6.6: Radial and vertical epicyclic frequencies vs.  $r/r_g$  in Schwarzschild geometry. Three resonant radii are indicated (Lewin & van der Klis 2006, and references therein).

observed features of *kHz QPOs*, thus, it is described in detail.

The basic idea of this model is that Keplerian frequencies which are 'beaten' by the spin frequency of the central object can produce *kHz QPOs*. However, a non-uniform structure has to corotate with the object which could be, e.g., a non-aligned magnetic field or radiation pattern. Such structures cannot be provided by a black hole due to the no-hair theorem<sup>2</sup>, thus the central object has to be a neutron star.

Additionally some kind of structure has to be in the disc to interact with the spin, which could be, e.g., a clump orbiting the neutron star with its Keplerian frequency  $\nu_K$ . If this clump orbits a pulsar it will at some point overtake the pulsar beam and will be illuminated by the beam as illustrated in figure 6.7 which leads to modulations of the X-ray flux. This illumination takes place with the 'beat' frequency  $\nu_{\text{beat}} = \nu_K - \nu_{\text{spin}}$  for prograde orbital motion whereas for retrograde motion illumination occurs only for frequencies  $\nu_{\text{beat}} = \nu_K + \nu_{\text{spin}}$ . However, at a certain disc radius of the clump the frequencies equals, respectively the spin frequency surpasses the orbital frequency.

A variation is the magnetospheric beat frequency model in which the interaction takes place outside the magnetosphere. In this sphere, close to the central object, the magnetic field is dominant and the sphere is restricted by the Alfvén radius. The observed modulations in the flux originate from a higher accretion rate when the clump is next to the magnetic poles which occurs periodically with  $\nu_{\text{beat}}$ . This is observed as the lower *kHz QPOs* frequency. The upper frequency originates from the Keplerian motion of the clump. However, e.g., Miller et al. (1998) showed that the mechanism of the magnetospheric model just produce a single strong oscillation with the beat frequency. Thus, another model is needed to explain the occurrence of two *kHz QPOs*. Therefore the sonic point model was proposed by Miller et al. (1998) assuming a Keplerian disc which penetrates the magnetosphere close to the ISCO radius where matter can reach supersonic velocities. A clump formed at this sonic point generates a stream of dense infalling gas which still rotates with its original Keplerian frequency  $\nu_K$ , even at the surface of the

<sup>2</sup>The no-hair theorem postulates, that a black hole is completely defined by mass, electrical charge and angular momentum.

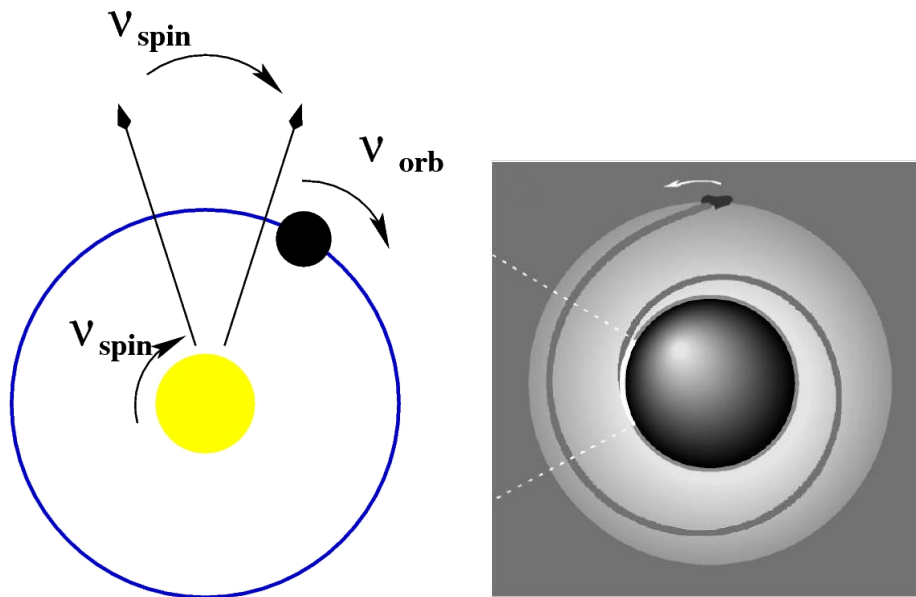


Figure 6.7: Example of a beat-frequency interaction. The blob in the disc periodically overtakes the non-uniform structure of the neutron star, after [Lewin & van der Klis \(2006\)](#). On the right side an illustration of the sonic-point model is shown, where the clump with its spiral flow and the emission from the flow's footpoint rotate at the same angular velocity (that of the clump's orbit), ([Miller et al. 1998](#)).

neutron star (see right side on [Figure 6.7](#)). The dense gas collides with the neutron star surface at the footpoint of the stream and produces a region with high X-ray luminosity which rotates with  $v_K$ , independent from the neutron star spin. This sonic-point frequency is associated with the high kHz QPOs frequency.

The magnetic field close to the neutron star is strong enough to channel the gas, thus a hot spot is produced at the magnetic poles which rotates with  $v_{spin}$ . The clump is irradiated by this hot spot and therefore the flux of the inwards flowing stream increases. Hence, the sonic-point frequency is beaten with the spin frequency which produces the so-called sonic-point beat frequency with  $v_B = v_K - v_{spin}$ .

The problems of this model are the restrictions on neutron stars and that variations of  $\Delta v$  cannot be explained easily.



# Chapter 7

## Results

The goal of this thesis is to show the expected performances of *Simbol-X* and *IXO* concerning the observation and characterization of broad iron lines and *kHz QPOs* in *LMXB*. The capability in the detection of broad iron lines in *LMXB* has been studied for three *LMXB* with neutron stars, namely Serpens X-1, 4U 1820-303, and 4U 1636-536. The capability to detect *kHz QPOs* of *Simbol-X* and *IXO* has been simulated for 4U 1820-303.

In this chapter the used software will be described first. Finally, the outcomes of the simulations will be discussed in detail.

### 7.1 Xspec and IDL

The simulations of the broad iron line were performed with the software package Xspec v11.3. For the simulations of *kHz QPOs* the Interactive Development Language IDL and a self-written C program were used.

#### 7.1.1 Xspec - A X-ray spectral fitting package

Xspec is an interactive, detector independent X-ray spectral-fitting package. It was developed in 1983 at the Institute of Astronomy in Cambridge and has become the standard package for the data analysis for most of the X-ray satellites, e.g., ROSAT and XMM-Newton (see more in [Arnaud 1996](#) and <http://heasarc.gsfc.nasa.gov/docs/xanadu/xspec/index.html>).

A variety of models is implemented in Xspec to describe X-ray spectra produced by different mechanisms (see Section 5.1). In this thesis the following models are used:

- *wabs* which describes the photo-electric absorption determined by a hydrogen column density in units of  $10^{22}$  atoms/cm<sup>2</sup>. The Wisconsin cross-section is used ([Morrison & McCammon 1983](#)).
- *vphabs* which uses contrary to *wabs* the cross-section proposed by [Balucinska-Church & McCammon \(1992\)](#), allowing variable abundances
- *bbody* which describes a simple blackbody with a temperature  $kT$  in keV and a normalization determined by  $L_{39}/D_{10}^2$  where  $L_{39}$  is the luminosity in units of  $10^{39}$  erg sec<sup>-1</sup> and  $D_{10}$  is the distance of the source in units of 10 kpc<sup>1</sup>

---

<sup>1</sup> 1 parsec (pc)  $\equiv$  3.4 lightyears

- *bbodyrad* similar to *bbody* but the normalization is proportional to the surface area of the neutron star
- *diskbb* is the model for a spectrum of a multicolor accretion disk after Mitsuda et al. (1984), which is expressed by the inner disk temperature and an expression of  $(R_{in}/\text{km})/(D/10\text{kpc})^2 \cos \theta$  with  $\theta$  as the angle of the disc.
- *compTT*: the spectrum resulting from the Comptonization of soft photons in a hot plasma is calculated after Titarchuk (1994), in which relativistic effects have been taken into account. The spectrum is described by the plasma temperature and the  $\beta$  parameter which determines the optical depth.
- *powerlaw*: describes a simple power law with a given photon index and flux.
- *gaussian*: a gaussian profile, described by the line energy in keV, the line width in keV and the flux of the photons in the line
- *diskline*: model based on Fabian et al. (1989) in which all broadening mechanisms described in 6.1 have been taken into account. The line energy, the emissivity<sup>2</sup> index  $\beta$  of the disc scaling with  $R^\beta$ , the inner and outer radius, the inclination angle and the photon flux can vary to fit the data to the model.

Xspec provides the ability to perform simulations for detectors which are in the development phase. A model of an X-ray source is folded with a given response matrix file (*rmf*) and if necessary an auxiliary response file (*arf*) to produce the spectrum which would be seen with the desired instrument. A *rmf* describes the distribution of a given photon energy over the detector pulse height channels, whereas in an *arf* information of the effective area and the geometry of the instrument is given.

Such simulations have been done for *Simbol-X* and *IXO* within this thesis. The responses for the *LED* and *HED* of *Simbol-X* are available at <http://www.apc.univ-paris7.fr/Simbolx2008/>. For the *WFI* and *HTRS* of *IXO* the response file has been taken from <http://jeeves.cfa.harvard.edu/ixo/IXOHome/IxoResponse>.

### 7.1.2 IDL - Interactive Development Language

For the simulation of *kHz QPOs* two IDL routines implemented in the *aitlib*<sup>3</sup> have been used. The routine **timmerlc.pro** is based on Timmer & Koenig (1995). A simulation of a lightcurve is performed with a given periodic shape, countrate and time resolution. The phase and the amplitudes of the Fourier transformation is changed randomly to get a real lightcurve which gives the countrate in each time bin including white noise (Poisson noise), in which all frequencies contribute equally to the time variability.

Further the routine **psd.pro**<sup>4</sup>, provides the ability to produce a Power Spectral Density (PSD) out of an evenly binned lightcurve which has to be given in counts per second. The power can be normalized in different ways, including the normalization after Leahy et al. (1983).

---

<sup>2</sup>Emissivity is defined as the ratio of the radiated energy to the radiated energy of a blackbody at same temperature

<sup>3</sup>aitlib available at <http://astro.uni-tuebingen.de/software/idl/aitlib/index.shtml>

<sup>4</sup>originally developed by Katja Pottschmidt and modified by Jörn Wilms

## 7.2 Studied Sources

In Table 7.1 and 7.2 are listed the best-fit parameters which have been used to simulate *Simbol-X* and *IXO* observations.

Table 7.1: The best-fit values of the continuum components of Serpens X-1, 4U 1820-303 (Cackett et al. 2008) and 4U 1636-536 (Pandel et al. 2008). The parameter of the vphabs model are given relative to their solar values (Wilms et al. 2000). Not given parameters are set to their solar abundances.

Model	Parameter	Serpens X-1	4U 1820-303	4U 1636-536
wabs	$N_{\text{H}}$ in ( $10^{22}\text{cm}^{-2}$ )	$0.56\pm 0.01$	$0.26\pm 0.01$	
phabs	$N_{\text{H}}$ in ( $10^{21}\text{cm}^{-2}$ )	-	-	$3.83\pm 0.10$
	O abundance	-	-	$1.27\pm 0.03$
	Ne abundance	-	-	$1.2\pm 0.2$
	Si abundance	-	-	$2.0\pm 0.4$
	Fe abundance	-	-	$1.47\pm 0.11$
body	temperature in keV	$2.28\pm 0.02$	$2.46\pm 0.03$	
	normalization( $10^{-2}$ )	$4.9\pm 0.2$	$3.2\pm 0.1$	
diskbb	temperature in keV	$1.21\pm 0.01$	$1.15\pm 0.02$	
	normalization	$103\pm 5$	$55\pm 3$	
Power-law	index	$3.6\pm 0.4$	$2.1\pm 0.1$	
	normalization ( $10^{-2}$ )	$18\pm 3$	$8.17\pm 0.02$	
compTT	$T_0$ (keV)			$1.45\pm 0.02$
	$T_C$ (keV)			$>9$
	$\tau_C$			$<1.3$
	normalization ( $10_{-3}$ )			$9\pm 8$
diskbb	$T_{\text{Disk}}$ (eV)			$780\pm 20$
	normalization			$200\pm 13$
bodyrad	$T_{\text{bb}}$ (eV)			$177\pm 7$
	normalization ( $10^3$ )			$29\pm 8$

Table 7.2: The best-fit values of the diskline components of Serpens X-1, 4U 1820-303 (Cackett et al. 2008) and 4U 1636-536 (Pandel et al. 2008).

Parameter	Serpens X-1	4U 1820-303	4U 1636-536
Line Energy (keV)	$6.83^{+0.15}_{-0.06}$	$6.97_{-0.18}$	$7.06\pm 0.10$
$R_{in}$ ( $\text{GM}/c^2$ )	$7.7\pm 0.5$	$6.7^{+1.4}_{-0.7}$	$<13.3$
Emissivity index $\beta$	$-4.8^{+0.4}_{-0.8}$	$-4.3^{1.1}_{-2.1}$	$-2.32\pm 0.22$
Inclination (degrees)	$26\pm 2$	$19^{+5}_{-18}$	$>64$
Normalization ( $10^{-3}$ )	$6.6\pm 0.6$	$1.8\pm 0.4$	$0.91\pm 0.20$

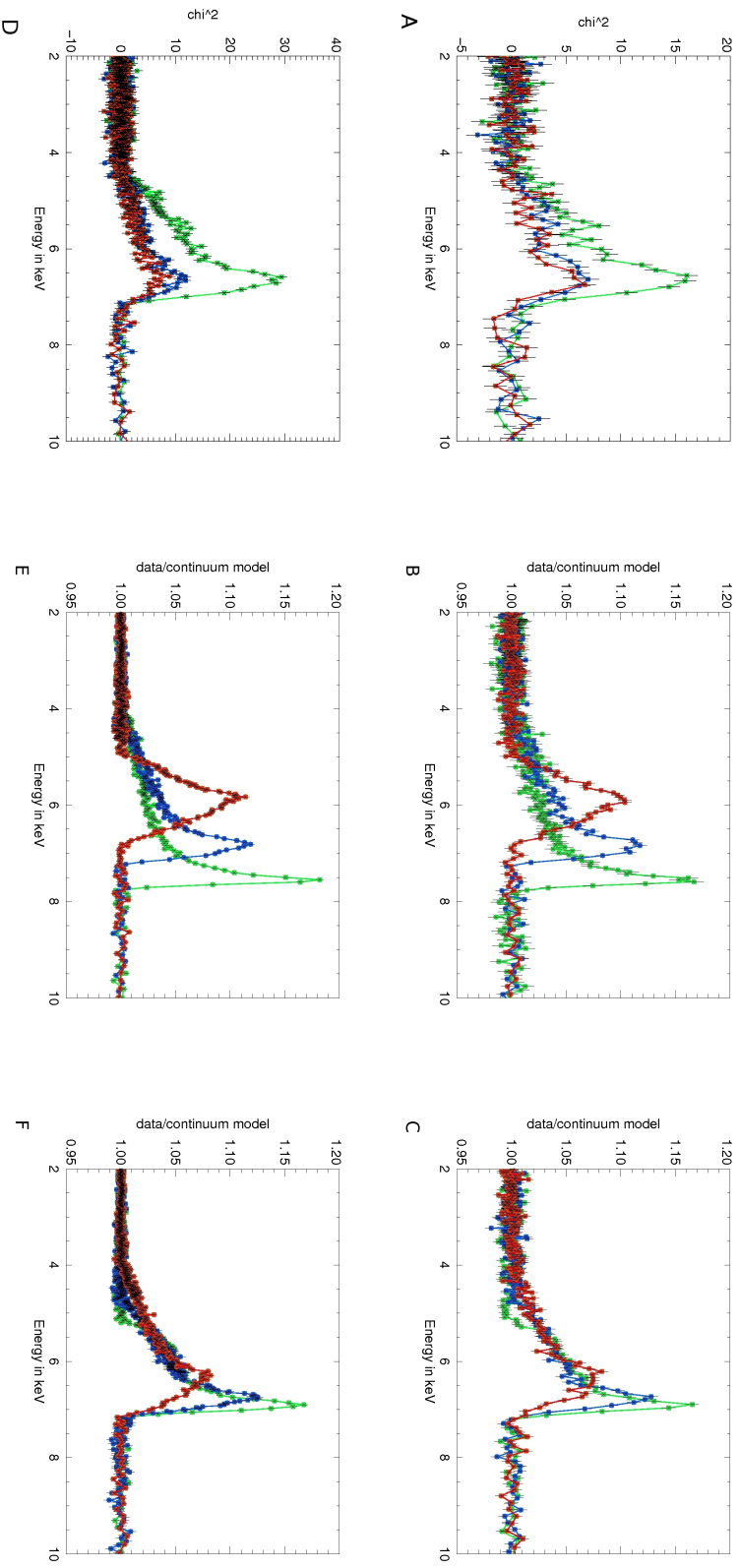


Figure 7.1: The upper panels shows simulations for *Simbol-X* and in the lower panels results for *IXO* are shown. The first plots show the broad iron line which would be observed with *Simbol-X* and *IXO* in different observation times of 500 s (red), 1 000 s (blue) and 5 000 s (green). The residuals are plotted in terms of sigma versus the energy. The plots in the panels B, C, E and F are plotted as data/continuum model versus the energy. Panels B and E show Serpens X-1 with different inclination angles, 10° (red points), 30° (blue points) and 45° (green points). The panels C and F show Serpens X-1 with different inner radii, 6  $\text{GM}/c^2$  (red), 9  $\text{GM}/c^2$  (blue) and 12  $\text{GM}/c^2$  (green). See details in the text.

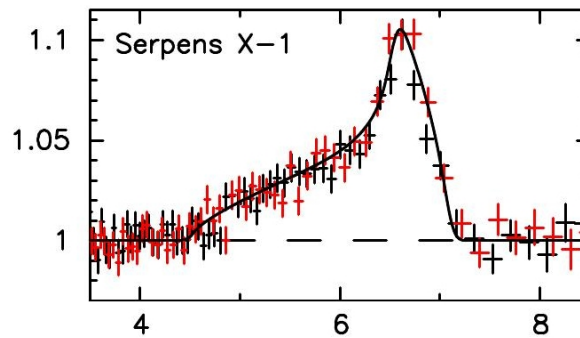


Figure 7.2: Iron line in Serpens X-1 observed with Suzaku. The ratio of count rate to continuum model is shown. The different colored points are data from two different detectors. The solid line is the best-fitting diskline model (Cackett et al. 2008).

### 7.2.1 Serpens X-1

Serpens X-1 is an Atoll source *LMXB* with a flux of  $5.09 \times 10^{-9}$  erg cm $^{-2}$  s $^{-1}$  in the constellation Serpens<sup>5</sup>. It was discovered in 1965 by Bowyer et al. in an Aerobee<sup>6</sup> mission. It was catalogued in the 4th Uhuru catalogue as 4U 1837+04. Observation of Type I X-ray bursts by Swank et al. (1976) confined that a neutron star is the compact object of the system. Analysis of the lightcurve showed dips and eclipses, therefore the inclination angle was constrained to be under 60°. The detection of a broad iron line was reported for the first time by Oosterbroek et al. (2001). In these observations, performed by BeppoSax and RXTE, the iron line profile could be fitted with a broad gaussian. XMM-Newton observations showed that the broadening is caused by relativistic effects (Bhattacharyya & Strohmayer 2007). The line profile was modeled with the Xspec model *laor*, which assumes a maximally rotating neutron star with a spin parameter *j* of 0.998, which is not expected from *LMXB* (Miller et al. 1998). The broad iron line which was detected in Suzaku<sup>7</sup> observations by Cackett et al. (2008) could be described by the diskline model.

The simulations for Serpens X-1 within this thesis were performed based on the best-fit values reported by Cackett et al. (2008, see Table 7.2).

A variety of observations have been simulated with *Simbol-X*. The line profiles are shown in panel A of Figure 7.1. The residuals<sup>8</sup> are plotted in terms of sigma versus the energy. The line profiles measured in different observation times of 5 000 s (green line), 1 000 s (blue line) and 500 s (red line) are shown in panel A in Figure 7.1.

The line was fitted with a simple gaussian profile. The energy is in a lower energy range of (6.30–6.39 keV), whereas the width of the line has to be 0.56 keV. For a 10 ks observation the best-fit gaussian is plotted together with the relativistic broad iron line in Figure 7.3. The gaussian profile does not well describe the line, the red.  $\chi^2$  is 1.39 for 1470 d.o.f, which implies that the fit is not good. Hence, the line has to be broadened by relativistic effects.

<sup>5</sup>Latin for Snake

<sup>6</sup>Research rocket in the 1950's and 1960's

<sup>7</sup>A JAXA-NASA cooperation X-ray satellite mission, which was launched in 2001

<sup>8</sup>the data flux minus the flux predicted by the model

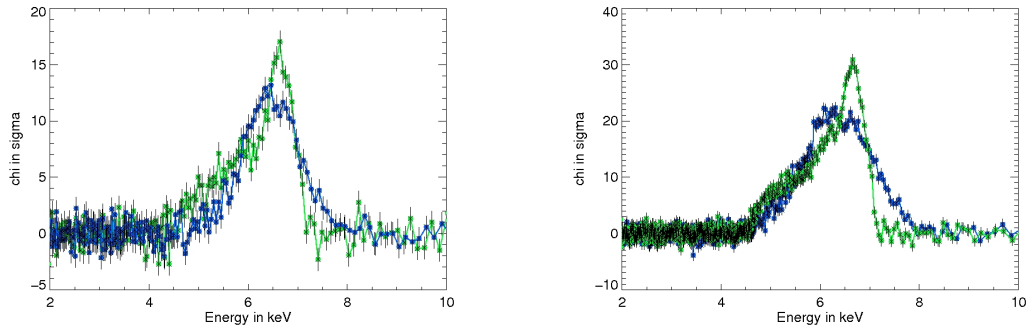


Figure 7.3: Iron line in Serpens X-1 simulated with *Simbol-X* on the left side and *IXO* on the right side. The relativistic line profile (green points) reported by Cackett et al. is reproduced. A gaussian profile with the best fit-values is shown in blue points (see Text for details).

To take relativistic effects into account the line was fitted with the diskline model. The reduced  $\chi^2$  ( $\chi^2/\text{d.o.f.}$ <sup>9</sup>) was 1.13 for 1468 d.o.f. The energy of the line was constrained to be in the 90% confidence range<sup>10</sup> of 6.80–6.98 keV (1.3%) with a best fit value of 6.89 keV. The inner radius of the disk was found to be at 7.6 GM/c<sup>2</sup> (7.30–7.94 GM/c<sup>2</sup>, 4.2%). The inclination angle was determined with a 6% uncertainty to 25.46° as a best-fit value and a range of 24.54°–27.00°.

To demonstrate the performance of *Simbol-X* the input inclination angles and the inner radius were set to different values separately. The resulted line profiles for the different inclination angles (10°, 30°, 45°) are shown in panel B of Figure 7.1. The line profile measured with *Simbol-X* for Serpens X-1 is sensitive to changes in inclination angle. For an inclination angle of 10° the energy of the line could be constrained to an energy range of 6.74–6.98 keV which give an uncertainty of 2.3% for a best fit value of 6.82 keV. The inner radius laid between 7.41–8.18 GM/c<sup>2</sup> (5.5%) with a best-fit value of 7.84 GM/c<sup>2</sup> whereas the inclination angle could be restricted to 8.6% to 9.28° with a confidence range of (8.48°–9.90°).

The inclination angle of 30° was constrained to a range of 29.86°–31.60° with a best-fit value of 31.10° which lead to an uncertainty of 4.0%. The best-fit value for the radius was 7.58 GM/c<sup>2</sup> with a 90% confidence region of 7.33–7.92 GM/c<sup>2</sup> (4.5%). The energy of the line was constrained to a range of 6.74–6.82 keV with 6.77 keV as best fit value with an uncertainty of 0.7%.

At an inclination angle of 45° the energy had a confidence region of 6.69–6.95 keV with a best-fit value of 6.88 keV (2.8%). The inner radius was restricted to 6.95–8.28 GM/c<sup>2</sup> with the best-fit value of 7.34 GM/c<sup>2</sup> (12.8%). The best-fit value for the inclination angle was determined to 43.84° with an uncertainty of 10.8% in the range of 42.50°–48.60°.

The line profiles originating at inner radii of 6 GM/c<sup>2</sup>, 9 GM/c<sup>2</sup> and 12 GM/c<sup>2</sup> are shown in panel C of Figure 7.1. For an inner radius of 6 GM/c<sup>2</sup> the line energy was constrained to the energy range of 6.75–6.92 keV with a best fit value of 6.84 keV and an uncertainty of 1.3%. The inner radius was

<sup>9</sup>degrees of freedom

<sup>10</sup>If not stated otherwise, confidence refers to the common 90% confidence of the achievement

fitted to  $6.60 \text{ GM}/c^2$  with a confidence region of  $6.16\text{--}6.75 \text{ GM}/c^2$  (6.7%). A best-fit value of  $23.05^\circ$  were found for the inclination angle with an uncertainty of 10.8% ( $21.85^\circ\text{--}25.54^\circ$ ).

With an inner radius of  $9 \text{ GM}/c^2$  the energy of the line could be restricted to  $6.74\text{--}6.85 \text{ keV}$  (0.8%) with a best fit value of  $6.79 \text{ keV}$ . The inner radius was determined to  $8.90 \text{ GM}/c^2$  with an uncertainty of 4.2% in the range of  $8.53\text{--}9.25 \text{ GM}/c^2$ . The inclination angle was constrained to be in the range of  $26.07^\circ\text{--}28.33^\circ$  with a best-fit value of  $27.22^\circ$  (3.9%).

For an inner radius of  $12 \text{ GM}/c^2$  the energy of the line was  $6.85 \text{ keV}$  with a confidence region of 0.9% ( $6.81\text{--}6.91 \text{ keV}$ ). The inner radius could be constrained to the region of  $11.48\text{--}12.48 \text{ GM}/c^2$  with the best-fit value of  $11.98 \text{ GM}/c^2$  (4.2%) and for the inclination angle the value was fitted to  $25.55^\circ$  with an uncertainty of 4.0% in the range of  $24.53^\circ\text{--}26.44^\circ$ .

The same simulations were made for *IXO*, which results are shown in the lower panels (D–F) of Figure 7.1. In panel D the line profile for different observation times are shown. The observation times are 500 s (red points), 1 000 s (blue points) and 5 000 s (green point).

A gaussian was fitted to the data, but the red.  $\chi^2$  exceeded 2, which indicates that the line cannot be modeled with a gaussian. The best-fit gaussian (blue points) with a red.  $\chi^2$  of 2.7241 for 1433 d.o.f. is shown on the right side of Figure 7.3 together with the relativistic broad iron line.

The line was fitted with diskline model, which gave a red.  $\chi^2$  of 1.0780 for 1424 d.o.f. The line energy was constrained to be in the range of  $6.81\text{--}6.86 \text{ keV}$  with a best-fit value of  $6.83 \text{ keV}$  (0.35%). The inner radius was fitted to  $7.69 \text{ GM}/c^2$  with a 90% confidence region of  $7.59\text{--}7.74 \text{ GM}/c^2$  (0.9%) and for the inclination angle a best-fit value of  $26.01^\circ$  was found within a range of  $25.70^\circ\text{--}26.42^\circ$  (1.3%).

Like for *Simbol-X* the input values for the inclination angle and the inner disk radius was varied. The resulting line profiles are shown in panel E and F of Figure 7.1.

For an inclination angle of  $10^\circ$  the line energy was fitted to  $6.81 \text{ keV}$  with a 90% confidence range of  $6.78\text{--}6.86$  (0.7%). The inner radius can be constrained to a range of  $7.67\text{--}7.89 \text{ GM}/c^2$  with a best-fit value of  $7.74 \text{ GM}/c^2$  which lead to an uncertainty of 1.8%. The inclination angle was restricted to  $9.91^\circ\text{--}10.26^\circ$  (2.3%) with a best-fit value of  $10.14^\circ$ .

The line energy could be constrained to a range of  $6.81\text{--}6.85 \text{ keV}$  for an inclination angle of  $30^\circ$ . The best-fit value was  $6.82 \text{ keV}$  which lead to an uncertainty of 0.4%. The inner radius was in the range of  $7.59\text{--}7.80 \text{ GM}/c^2$  with  $7.70 \text{ GM}/c^2$  as best-fit value with 1.4% uncertainty. The inclination angle is determined to  $30.05^\circ$  with a 90% confidence region of  $29.61^\circ\text{--}30.39^\circ$  (1.5%). With  $45^\circ$  as the inclination angle the energy of the line can be restricted to a range of  $6.77\text{--}6.86 \text{ keV}$  and  $6.78 \text{ keV}$  as best-fit with an uncertainty of 1.2%. The inner radius is restricted to  $7.31\text{--}7.77 \text{ GM}/c^2$  with a best-fit value of  $7.64$  (the uncertainty is 4.3%). The inclination angle is determined with an uncertainty of 3.9% to  $46.17^\circ$  in the range of  $44.37^\circ\text{--}46.51^\circ$ .

Emission at inner radii of  $6 \text{ GM}/c^2$ ,  $9 \text{ GM}/c^2$  and  $12 \text{ GM}/c^2$  produces line profiles shown in panel F of Figure 7.1. For an inner radius of  $6 \text{ GM}/c^2$  the line energy was constrained to the 90% confidence region of  $6.82\text{--}6.88 \text{ keV}$  with a best fit value of  $6.85 \text{ keV}$  and an uncertainty of 0.4%. The inner radius was fitted to  $6.00 \text{ GM}/c^2$  with a confidence region of  $6.00\text{--}6.08 \text{ GM}/c^2$  (1.3%). A best-fit value of  $25.84^\circ$  were found for the inclination angle within a range of  $25.35^\circ\text{--}26.34^\circ$  with an uncertainty of 1.9%.

With an inner radius of  $9 \text{ GM}/c^2$  the line energy could be restricted to the range of  $6.82\text{--}6.86 \text{ keV}$  (0.3%) with a best fit value of  $6.84 \text{ keV}$ . The inner radius was determined to  $8.89 \text{ GM}/c^2$  in the

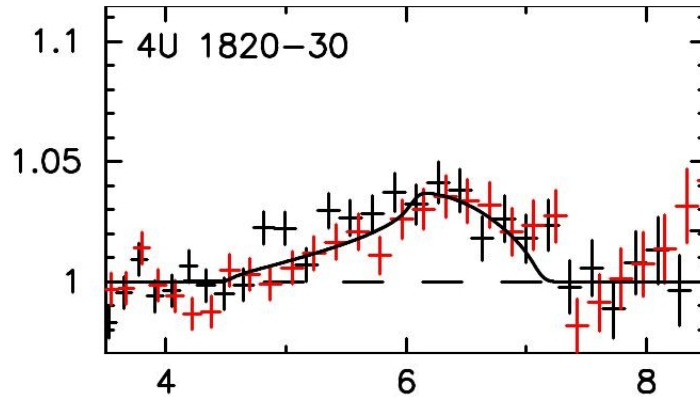


Figure 7.4: Iron line in 4U 1820-303 observed with Suzaku. (Cackett et al. 2008)

range of  $8.77\text{--}9.00\text{ GM/c}^2$  (1.3%). The inclination angle was constrained to be in the range of  $25.60^\circ\text{--}26.29^\circ$  with a best-fit value of  $26.00^\circ$  (1.5%).

For an inner radius of  $12\text{ GM/c}^2$  the line energy was  $6.83\text{ keV}$  with a confidence region of  $6.82\text{--}6.85\text{ keV}$  (0.3%). The inner radius can be constrained to the region of  $11.80\text{--}12.14\text{ GM/c}^2$  with the best-fit value of  $11.97\text{ GM/c}^2$  (1.4%) and for the inclination angle the value is determined to  $26.13^\circ$  with an uncertainty of 2.1% in the range of  $25.78^\circ\text{--}26.28^\circ$ .

### 7.2.2 4U 1820-303

4U 1820-303 was classified as an Atoll source by [Hasinger & van der Klis \(1989\)](#) with an orbital period of 11.4 minutes ([Stella et al. 1987](#)). [Grindlay et al.](#) observed in 1976 X-ray bursts. *kHz QPOs* have been first detected by [Smale et al. \(1997\)](#) and [Zhang et al.](#) observed one year later also *kHz QPOs*. A relativistic broad iron line was reported by [Cackett et al. \(2008, see Table 7.2\)](#) from which also the input parameters for the simulation were taken. The flux is  $\sim 2.78 \times 10^{-9}\text{ erg cm}^{-2}\text{ s}^{-1}$ .

In the panels A and C of Figure 7.6 the line profile for different observation times are shown for *Simbol-X*, respectively for *IXO*. The observation time increases from 500 s, to 1000 s up to 5000 s. A gaussian profile was used to fit the line. The best-fit value delivered a line energy of 6.12 keV and a width of 550 eV. The gaussian fitted well to the data with a red.  $\chi^2$  of 1.0377 for 1470 d.o.f. The fit to the *IXO* simulation provide a width of 647 eV at an energy of 6.09 keV. The red.  $\chi^2$  was 1.0354 for 1426 d.o.f. In Figure 7.5 the gaussian with reported best fit values are shown together with the relativistic broad iron line. Based on the observation of [Cackett et al.](#) a broad gaussian line cannot be excluded.

Although, a gaussian line profile fit very well to the data, the line was also fitted with the diskline model. The best-fit values for 4U 1820-303 are reported in table 7.3.

The energy of the line was constrained for a *Simbol-X* simulation within 7.5% of the best-fit value 7.08 keV. The inner radius was fitted to  $6.75\text{ GM/c}^2$  with an uncertainty of 11.1%, whereas the inclination angle could be constrained within 27.9% of the best-fit value  $16.86^\circ$ . For an *IXO* simulation the line energy was restricted within 1.3% of 6.97 keV. The inner radius was found to be at  $6.83\text{ GM/c}^2$  with an uncertainty of 3.5%, whereas the inclination angle could be constrained within

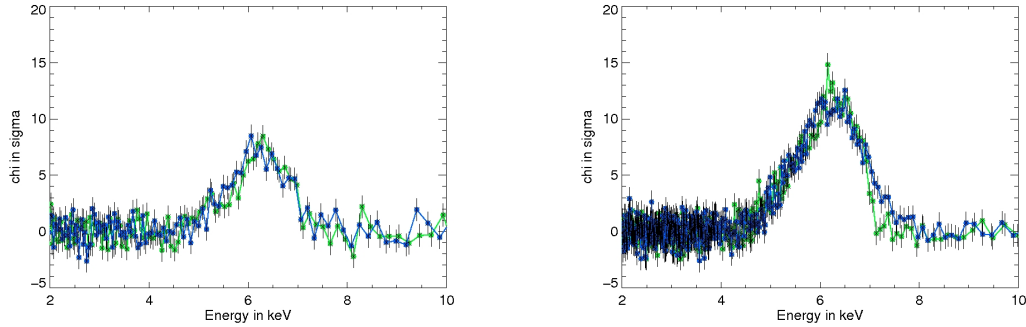


Figure 7.5: Simulations of 4U 1820-303 for *Simbol-X* and *IXO*. The relativistic line profile for a 10 ks observation is plotted in green. A gaussian profile with the best-fit values, which are reported in the text, are shown in blue.

Table 7.3: The best fit parameters for a fit with *Simbol-X* and *IXO* using diskline, in brackets the 90% confidence region is given.

Parameter	<i>Simbol-X</i>	<i>IXO</i>
Line energy in keV	7.08 (6.89–7.61)	6.97 (6.90–7.06)
Inner Radius in $\text{GM}/c^2$	6.75 (6.00–7.38)	6.83 (6.59–7.06)
Inclination angle in degree	16.86 (14.00–21.56)	18.42 (17.29–19.69)
red. $\chi^2$ (d.o.f.)	1.0320 (1468)	0.9765 (1424)

6.9% of  $18.42^\circ$ .

The inclination angle and the inner radius was varied again to demonstrate the sensitivity in changes of these values. The inclination angle was set to  $10^\circ$ ,  $30^\circ$  and  $45^\circ$ , and the inner radius was set to  $6 \text{ GM}/c^2$ ,  $9 \text{ GM}/c^2$  and  $12 \text{ GM}/c^2$ . The line profiles of the different inclination angles are shown in panel B for *Simbol-X* and in panel E for *IXO*. Panel C and F show the line profile for different inner radii for *Simbol-X*, respectively *IXO*.

For an inclination angle of  $10^\circ$  the energy of the line could be constrained to a 90% confidence region of 6.79–7.39 keV. The best-fit value was 6.89 and the uncertainty 7.3%. The inner radius was restricted to 6.52–7.61  $\text{GM}/c^2$  with a best-fit value of 7.01  $\text{GM}/c^2$ , which lead to an uncertainty of 8.6%. The inclination angle was fitted to  $9.64^\circ$  with an uncertainty of 35.8% ( $6.75^\circ$ – $13.09^\circ$ ). Whereas for an *IXO* observation the line is restricted to the energy range of 6.89–7.08 keV (1.4%) with the best fit-value at 6.98 keV. The inner radius is fitted to 6.61  $\text{GM}/c^2$  with a 90% confidence region of 6.39–6.84  $\text{GM}/c^2$  (3.5%). The inclination angle, with a best-fit value of  $9.42^\circ$ , is restricted to a confidence region of  $8.77^\circ$ – $10.38^\circ$  (10%).

In a *Simbol-X* observation with an inclination angle of  $30^\circ$  the line energy was constrained to a

region of 6.1% (6.99–7.51 keV) of the best-fit value of 7.08 keV. The best-fit value for the inner radius was  $6.84 \text{ GM}/c^2$  with an uncertainty of 11.4% ( $6.34\text{--}7.62 \text{ GM}/c^2$ ). The 90% confidence region for the inclination angle was  $20.87^\circ\text{--}29.63^\circ$  (23.1%) with a best fit value of  $27.35^\circ$ .

An *IXO* observation provided a confidence region for the line energy of 6.94–7.02 keV (0.7%) with 6.97 keV as best-fit value. A restriction of the inner radius to  $6.53\text{--}6.92 \text{ GM}/c^2$  (3.6%) was possible and a best-fit value of  $6.68 \text{ GM}/c^2$  was determined. The inclination angle was  $30.32^\circ$  within a confidence region  $29.14^\circ\text{--}31.39^\circ$  (3.9%).

In a *Simbol-X* observation with a higher inclination angle of  $45^\circ$ , the line was found at 6.82 keV with an uncertainty of 1.3% (6.75–6.91 keV). The inner radius could be constrained to  $6.00\text{--}13.91 \text{ GM}/c^2$  with a best-fit value of  $7.58 \text{ GM}/c^2$  which leads to an uncertainty of 83.5%. The inclination angle was fitted to  $45.38^\circ$  with a 90% confidence region of  $42.82^\circ\text{--}52.70^\circ$  which lead to an uncertainty of 16.1%.

The energy was constrained in an *IXO* observation to 6.84–7.12 keV with 7.04 keV as best-fit value and an uncertainty of 2.8%. The inner radius was  $7.56 \text{ GM}/c^2$  in a confidence region of  $7.21\text{--}7.84 \text{ GM}/c^2$  (4.6%). The inclination angle was restricted to  $41.38^\circ\text{--}47.48^\circ$  (10.8%) with a best-fit value of  $42.86^\circ$ .

For an inner radius of  $6 \text{ GM}/c^2$  the line energy could be determined by an *Simbol-X* observation to 6.90 keV with an uncertainty of 1.7% (6.78–7.02 keV). The inner radius was constrained to be below  $6.57 \text{ GM}/c^2$  with a best-fit value of  $6.07 \text{ GM}/c^2$  which lead to an uncertainty of 8.2%. The inclination angle was determined with an uncertainty of 9.8% ( $24.73^\circ\text{--}29.51^\circ$ ) to  $26.87^\circ$ . The line energy was constrained by an *IXO* observation to a range of 6.97–7.13 keV (1.1%) with 7.05 keV as best-fit value. The inner radius was determined to  $6.02 \text{ GM}/c^2$  within a confidence region of 3.3% ( $6.00\text{--}6.20 \text{ GM}/c^2$ ). The inclination angle with a best fit value of  $18.83^\circ$  had an uncertainty of 5.9% ( $17.72^\circ\text{--}19.92^\circ$ ).

At a larger inner radius of  $9 \text{ GM}/c^2$  the line energy could be restricted, in a *Simbol-X* observation, to 7.02–8.38 keV with a best-fit value of 7.31 keV, which lead to an uncertainty of 14.6%. The best-fit value for the inner radius was  $8.39 \text{ GM}/c^2$  within a 90% confidence region of 25.1% ( $6.28\text{--}9.73 \text{ GM}/c^2$ ). The best-fit value of the inclination angle was found to be  $20.36^\circ$  within a range of 27.7% ( $14.73^\circ\text{--}24.78^\circ$ ).

An *IXO* observation provided a confidence region of the line energy of 6.93–7.03 keV (0.8%) and a best fit value of 6.97 keV. Further the inner radius could be restricted to  $8.56\text{--}8.99 \text{ GM}/c^2$  (3.2%) with a best-fit value of  $8.84 \text{ GM}/c^2$ . The inclination angle was determined to  $19.55^\circ$  with an uncertainty of 4.7% ( $18.63^\circ\text{--}20.18^\circ$ ).

For  $12 \text{ GM}/c^2$  as inner radius the line could be constrained with *Simbol-X* to 6.96–7.22 keV (2.1%) with a best fit value of 7.07 keV. The inner radius was determined to  $11.49 \text{ GM}/c^2$  with an uncertainty of 10% ( $10.38\text{--}12.63 \text{ GM}/c^2$ ). The best-fit value for the inclination angle was  $23.88^\circ$  within the range of  $21.82^\circ\text{--}26.85^\circ$  (12.6%). An *IXO* observation could constrain the energy of the line to 6.91–6.97 keV with 6.93 keV as best-fit value which lead to an uncertainty of 0.4%. The inner radius was restricted to  $11.53\text{--}12.34 \text{ GM}/c^2$  (3.6%) with a best-fit at  $11.91 \text{ GM}/c^2$ . The inclination an angle was determined to  $19.78^\circ$  within a confidence range of  $18.99^\circ\text{--}20.46^\circ$  (4.0%).

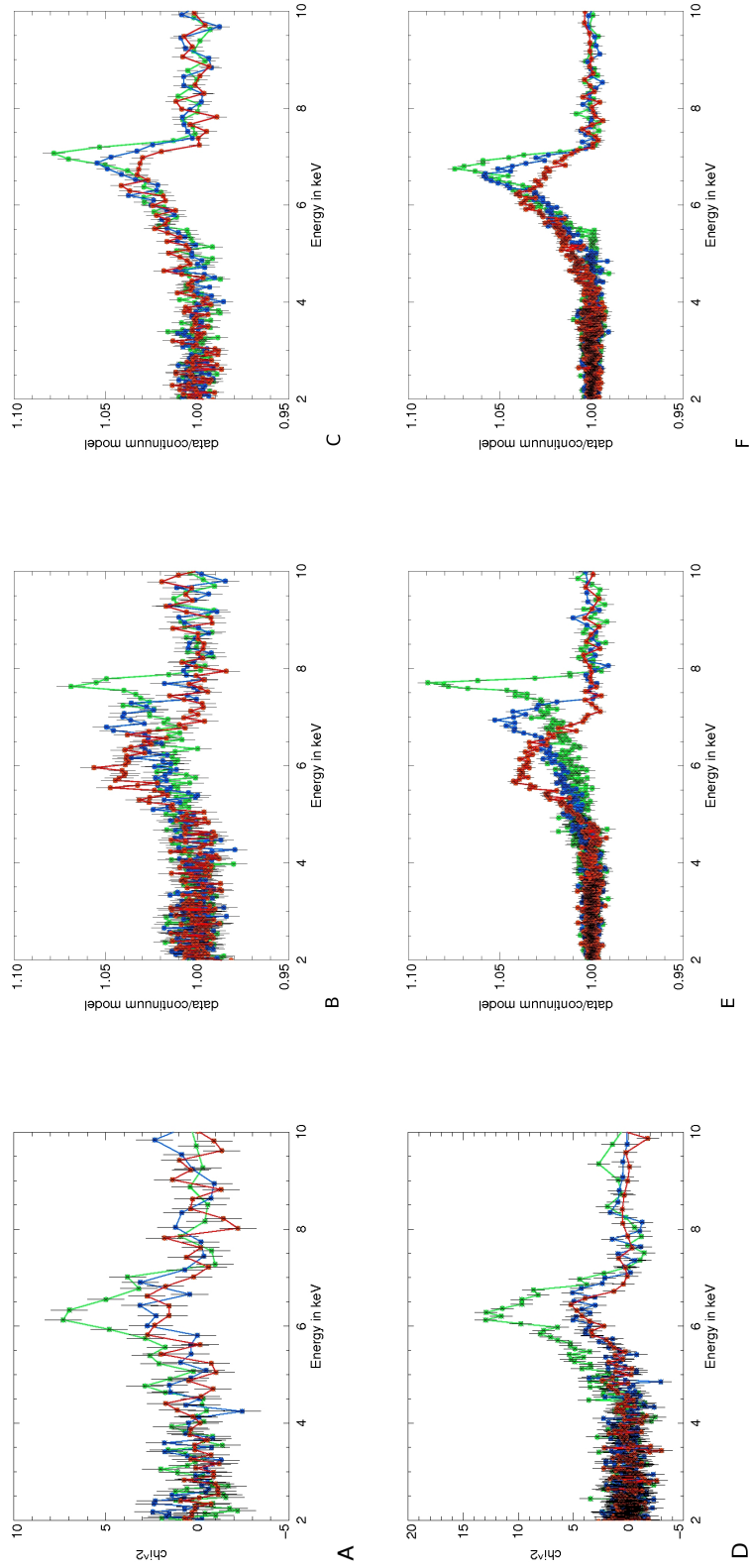


Figure 7.6: The **upper panel** shows simulations for **Simbol-X** and in the **lower panel** results for **IXO** are shown. The first plots, panel A and D, show the broad iron line which would be observed with *Simbol-X* and *IXO* in different observation times of 500 s (red), 1 000 s (blue) and 5 000 s (green). The second plots, panels B and E, show 4U 1820-303 with different inclination angles, 10° (red datapoints), 30° (blue points) and 45° (green points). The last plots, C and F, show 4U 1820-303 with different inner radii, 6  $\text{GM}/c^2$  (red), 9  $\text{GM}/c^2$  (blue) and 12  $\text{GM}/c^2$  (green).

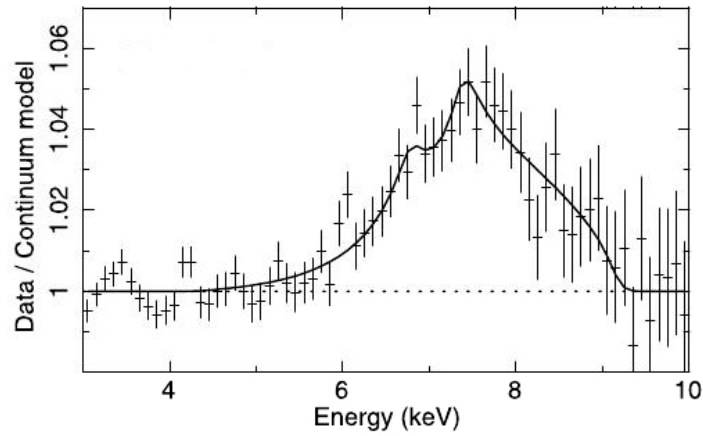


Figure 7.7: Relativistic iron line in 4U 1636-536. The flux is normalized to to the continuum flux. The solid line is the model flux (Pandel et al. 2008).

### 7.2.3 4U 1636-536

The *LMXB* 4U 1636-536 was classified as an atoll source by Hasinger & van der Klis (1989). An orbital period of 3.8 hours was measured by van Paradijs et al. in 1990. The flux has been measured to  $\sim 5.06 \times 10^{-9} \text{ erg cm}^{-2} \text{ s}^{-2}$ .

Zhang et al. (1996) and Wijnands et al. (1997b) observed *kHz QPOs* with a high frequency of  $\sim 1200 \text{ Hz}$  and a frequency difference of 300 Hz. A relativistic broad iron line has been reported by Pandel et al. (2008) for observations performed by XMM-Newton and RXTE. Three observations in which a broad iron line was detected were presented. The second observation from 2007 was chosen here, because for this observation the inclination angle could be constrained to be higher than  $64^\circ$ . The other observations had lower limits for the inclination angle of above  $80^\circ$  which is unlikely due to the none observation of dips and eclipses (Casares et al. 2006).

The simulations based on the reported values for the diskline model by Pandel et al. (2008). In panel A of Figure 7.9 the line profiles observed by *Simbol-X* for an observations time of 500 s, 1 000 s and 5 000 s are shown. In panel D of Figure 7.9 the line profile for different observation times for *IXO* are shown.

A fit with a gaussian profile gave a red.  $\chi^2$  of 0.9944 for 1477 d.o.f. with a line energy of 7.22 keV and a width of 696 eV for *Simbol-X*. For *IXO* the fit provided a red.  $\chi^2$  of 1.0661 for 1422 d.o.f. The gaussian had an energy of 7.21 keV and a width of 630 eV. The line profile of the best-fitting gaussian are shown in Figure 7.8 for *Simbol-X* and *IXO*, together with the line profile of the diskline model.

Also the diskline model was used to describe the iron line of 4U 1636-536, the best-fit values are summarized in the following table.

The inclination angles was changed to  $30^\circ$ ,  $45^\circ$  and  $60^\circ$  which is shown in Panel B of Figure 7.9 for *Simbol-X* and in panel E for *IXO*. It can be seen that the flux decreases and the line energy increases slightly. To distinguish between different inner radii is more difficult as can be seen in the panels C and F for *Simbol-X*, respectively for *IXO*. Figure 7.9. The inner radius was set to  $9 \text{ GM}/c^2$ ,  $20 \text{ GM}/c^2$  and  $30 \text{ GM}/c^2$ .

For an inclination angle of  $30^\circ$  the line energy was fitted to 7.05 keV with a confidence range

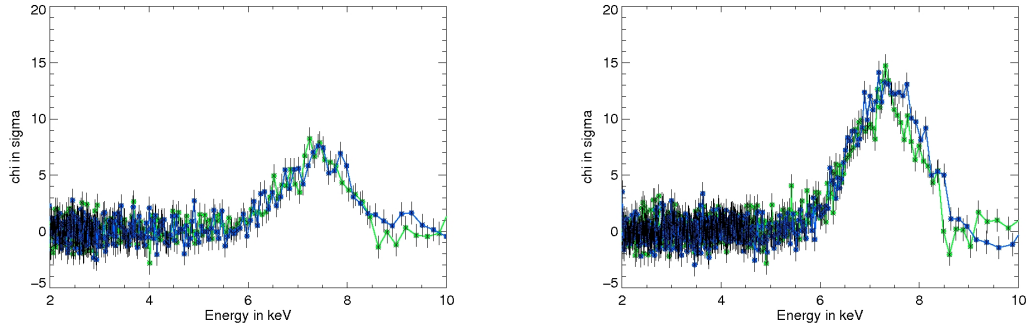


Figure 7.8: Simulations of 4U 1636-536 for *Simbol-X* and *IXO*. The relativistic line profile for a 10 ks observation is plotted in green. A gaussian profile with the best-fit values are shown in blue. See details in the text.

Table 7.4: The best fit parameters for a blind fit with *Simbol-X* and *IXO*, in brackets the 90% confidence region is given

Parameter	<i>Simbol-X</i>	<i>IXO</i>
Line energy in keV	7.03 (6.96–7.09)	7.06 (7.03–7.08)
Inner Radius in $\text{GM}/c^2$	14.09 (6.00–23.68)	6.00 (6.00–8.26)
Inclination angle in degree	66.01 (53.60–90.00)	54.81 (53.97–56.92)
red. $\chi^2$ (d.o.f.)	0.9747 (1475)	1.0268 (1419)

of 7.02–7.06 keV (0.4%). The inner radius was constrained to be in a range of 12.52–51.05  $c^2$  with a best-fit value of 36.88  $\text{GM}/c^2$ , which lead to an uncertainty of 66.6%. The inclination angle was restricted to 30.85°–39.84° (16.7%) with a best-fit value of 34.13°.

The line energy could be constrained to a range of 7.08–7.13 keV for an inclination angle of 45°. The best-fit value was 7.10 keV which lead to an uncertainty of 0.4%. The inner radius was in the range of 6.30–19.51  $\text{GM}/c^2$  with 16.22  $\text{GM}/c^2$  as best-fit value with an uncertainty of 61.1%. The inclination angle was determined to 43.65° with a confidence region of 42.32°–45.22° (3.9%).

With an inclination angle of 60° the energy of the line could be restricted to 7.07–7.15 keV and a best-fit value of 7.10 keV with an uncertainty of 0.7% was determined. The inner radius was restricted to 6.00–27.26  $\text{GM}/c^2$  with a best-fit value of 8.68  $\text{GM}/c^2$  which lead to an uncertainty of above 200%. The inclination angle was determined with an uncertainty of 28.6% (50.00°–73.61°) to 57.22°.

Emission at inner radii of 9  $\text{GM}/c^2$ , 20  $\text{GM}/c^2$  and 30  $\text{GM}/c^2$  produces line profiles shown in panel C of Figure 7.9 for *Simbol-X*. For an inner radius of 9  $\text{GM}/c^2$  the line energy was constrained to a confidence region of 6.94–7.04 keV with a best fit value of 6.99 keV and an uncertainty of 0.7%. The inner radius was fitted to 12.43  $\text{GM}/c^2$  with a confidence region of 10.44–13.62  $\text{GM}/c^2$  (16.1%). A best-fit value of the maximal allowed value of 90° were found for the inclination angle within a range of 70.15°–90.0° with an uncertainty of 22.2%.

With an inner radius of  $20 \text{ GM}/c^2$  the line energy could be restricted to  $6.97\text{--}7.11 \text{ keV}$  (1.3%) with a best fit value of  $7.06 \text{ keV}$ . The inner radius was determined to  $17.44 \text{ GM}/c^2$  in the range of  $15.14\text{--}20.31 \text{ GM}/c^2$  (16.5%). The inclination angle was constrained to be in the range of  $51.46^\circ\text{--}68.00^\circ$  with a best-fit value of  $63.14^\circ$  (19.5%).

For an inner radius of  $30 \text{ GM}/c^2$  the line energy was  $7.07 \text{ keV}$  with a confidence region of  $7.04\text{--}7.10 \text{ keV}$  (0.4%). The inner radius could be constrained to the range of  $37.73\text{--}48.90 \text{ GM}/c^2$  with the best-fit value of  $43.05 \text{ GM}/c^2$  (13.6%) The inclination angle was determined to  $89.75^\circ$  with an uncertainty of 18.6% ( $73.09^\circ\text{--}90.00^\circ$ ).

The line profiles for the different inclination angles and inner radii for *IXO* are shown in panel E, respectively panel F in Figure 7.9.

For an inclination angle of  $30^\circ$  the energy of the line could be constrained to a range of  $7.04\text{--}7.06 \text{ keV}$  which gave an uncertainty of 0.1% for a best fit value of  $7.05 \text{ keV}$ . The value of the inner radius was within the confidence region of  $12.98\text{--}15.85 \text{ GM}/c^2$  (10.1%) with  $14.45 \text{ GM}/c^2$  as best-fit value. The inclination angle was restricted to  $29.61^\circ\text{--}30.99^\circ$  (2.3%) with a best-fit value of  $30.33^\circ$ .

For an inclination angle of  $45^\circ$  the line energy was constrained to a range of  $7.05\text{--}7.10 \text{ keV}$  with an uncertainty of 0.4% for a best-fit value of  $7.07 \text{ keV}$ . The radius was determined to  $17.44 \text{ GM}/c^2$  with a confidence region of  $11.91\text{--}24.71 \text{ GM}/c^2$  (41.9%). The inclination angle had a best-fit value of  $44.95^\circ$  and an uncertainty of 5.3% ( $42.54^\circ\text{--}46.81^\circ$ ).

For an inclination angle of  $60^\circ$  the energy of the line was in the confidence region of  $7.07\text{--}7.11 \text{ keV}$  with a best-fit value  $7.09 \text{ keV}$  (0.3%). The inner radius could be restricted to the range of  $18.90\text{--}29.24 \text{ GM}/c^2$  with  $24.44 \text{ GM}/c^2$  (22.7%). The best-fit value of the inclination angle was determined to  $74.76^\circ$  with an uncertainty of 22.7% in the range of  $64.68^\circ\text{--}90.00^\circ$ .

For an inner radius of  $9 \text{ GM}/c^2$  the line energy was constrained to the range of  $7.05\text{--}7.11 \text{ keV}$  with a best fit value of  $7.08 \text{ keV}$  with an uncertainty of 0.4%. The inner radius is fitted to  $15.90 \text{ GM}/c^2$  with a confidence region of  $14.06\text{--}17.95 \text{ GM}/c^2$  (12.9%). A best-fit value of  $89.93^\circ$  were found for the inclination angle with an uncertainty of 13.5% ( $77^\circ\text{--}91^\circ\text{--}90.00^\circ$ ).

With an inner radius of  $20 \text{ GM}/c^2$  the energy of the line was restricted to  $7.04\text{--}7.08 \text{ keV}$  (0.3%) with a best fit value of  $7.06 \text{ keV}$ . The inner radius was determined to  $32.2 \text{ GM}/c^2$  with an uncertainty of 4.2% ( $21.38\text{--}36.69 \text{ GM}/c^2$ ). The inclination angle was constrained to be in the range of  $61.31^\circ\text{--}90.00^\circ$  with a best-fit value of  $87.72^\circ$  (30.1%).

For an inner radius of  $30 \text{ GM}/c^2$  the energy of the line was  $7.06 \text{ keV}$  with a confidence region of 0.3% ( $7.05\text{--}7.08 \text{ keV}$ ). The inner radius was restricted to  $33.31\text{--}50.05 \text{ GM}/c^2$  with the best-fit value of  $41.52 \text{ GM}/c^2$  (20.7%). The inclination angle was determined to  $71.11^\circ$  with an uncertainty of 26.6.0% ( $59.67^\circ\text{--}90.00^\circ$ ).

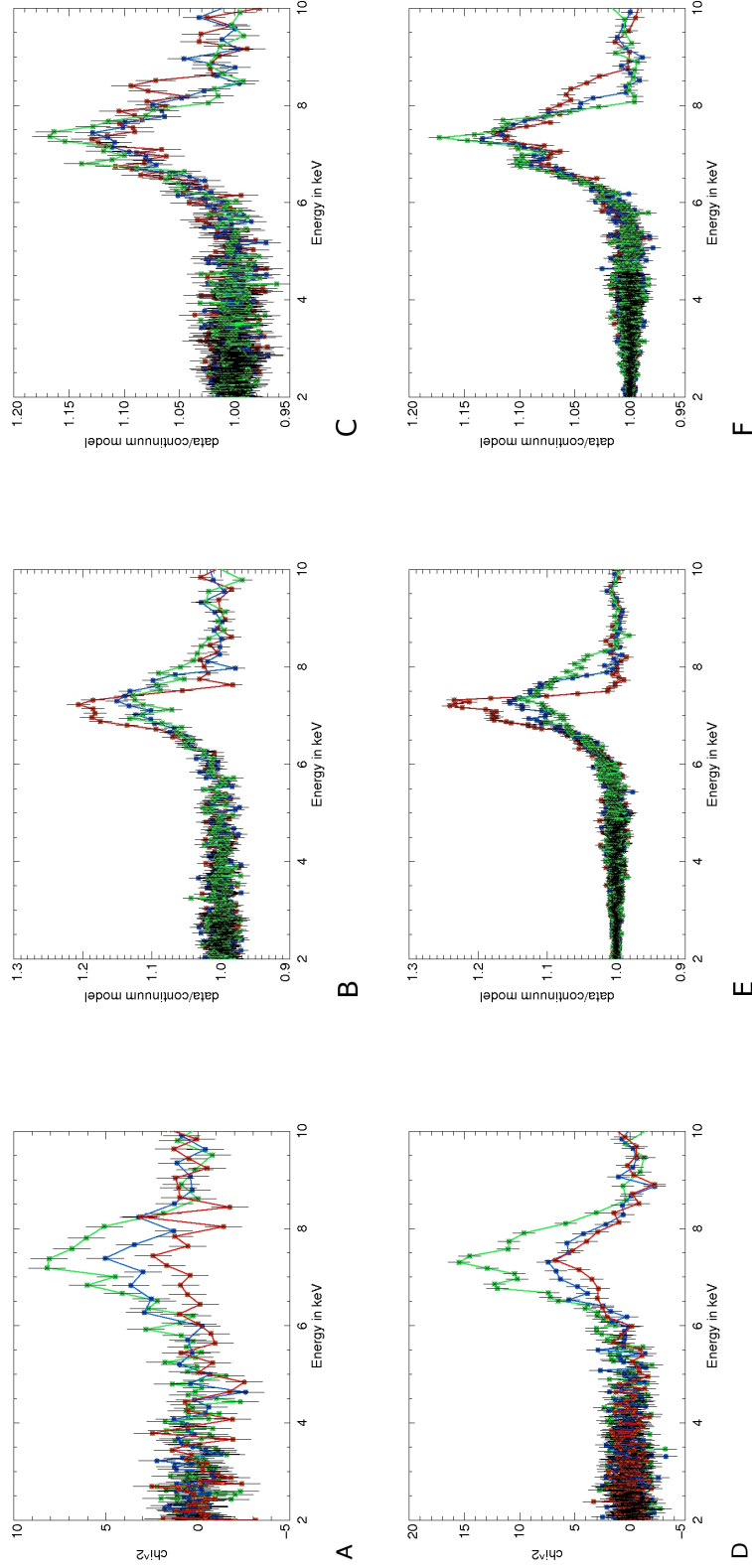


Figure 7.9: The **upper panel** shows simulations for **Simbol-X** and in the **lower panel** results for **IXO** are shown. The first plots, panel A and D, show the broad iron line which would be observed with **Simbol-X** and **IXO** in different observation times of 500 s (red), 1 000 s (blue) and 5 000 s (green). The second plots, panels B and E, show 4U 1636-536 with different inclination angles, 30° (red datapoints), 45° (blue points) and 60° (green points). The last plots, C and F, show 4U 1636-536 with different inner radii, 9  $\text{GM}/c^2$  (red), 20  $\text{GM}/c^2$  (blue) and 30  $\text{GM}/c^2$  (green).

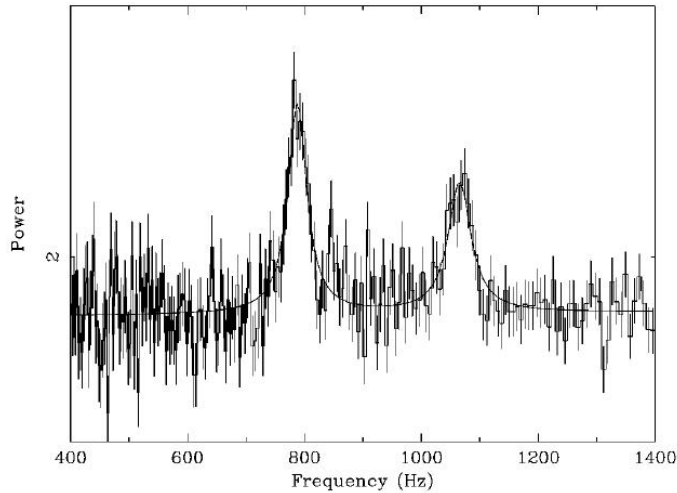


Figure 7.10: Power density spectrum of 4U 1820-303, showing the twin peaks and the best-fitting model (constant and two Lorentzians) (Smale et al. 1997)

### 7.3 Quasi Periodic Oscillations

Smale et al. reported in 1997 the discovery of *kHz QPOs* in 4U 1820-303. The observations were performed with the PCA mounted on RXTE. The power density spectrum is shown in Figure 7.10. Two frequencies were discovered: the lower QPO varies in the range of 546–796 Hz with a width of  $\sim 20$  Hz, whereas the higher frequency was detected at  $1065 \pm 7$  Hz and with a width of  $40 \pm 20$  Hz. Their amplitudes were  $4.1\% \pm 0.3\%$  and  $3.2\% \pm 0.8\%$ , respectively. When both frequencies were seen at the same time, the difference between them could be determined to  $275 \pm 8$  Hz. The *kHz QPOs* could be seen in a count rate range of 2520–2560 counts  $s^{-1}$ .

#### 7.3.1 Simulations

The simulations performed in this thesis based on the results reported by Smale et al..

The expected countrate of 4U 1820-303 in observations with *Simbol-X* and *IXO* were determined with the help of Xspec. According to the simulations for the broad iron line a spectrum was produced and the count rate for each simulated detector was returned. The expected countrate for the *LED* of *Simbol-X* is  $\sim 800$  cps, whereas for the HTRS on board of *IXO*  $\sim 16\,500$  cps can be expected. The time resolution is set to  $200 \mu s$  for both detectors. Such a time resolution provide the possibility to detect frequencies up to 5 000 Hz.

To simulate the *kHz QPOs*, an IDL procedure based on an example procedure by Michael Martin and Jörn Wilms (Wilms et al. 2004) was used. The shape of the PSD was modeled with a broken power law and two lorentzians for the *kHz QPOs*. The IDL routine `timmerlc.pro` produces with this model PSD a lightcurve with the expected countrate for each time bin.

The countrate given by `timmerlc` is used to simulate a real lightcurve. A C program was written therefore.

Every time bin  $i$  has a corresponding countrate  $c_i$ . In each time bin a given number  $N$  of photons is

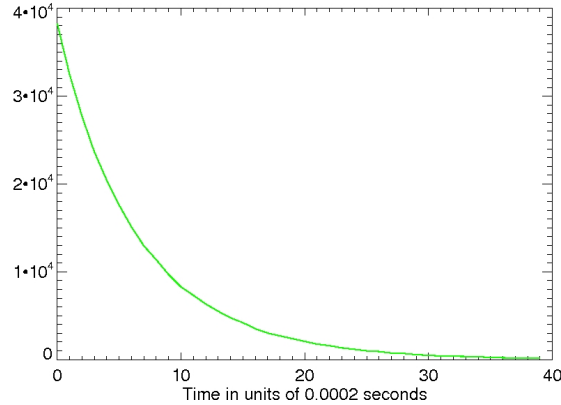


Figure 7.11: Exponential distribution of photons. On the y-axis the number of occurrences is plotted, while on the X-axis the time between two photons in units of  $200\ \mu\text{s}$  is shown.

simulated. The photons are randomly distributed over a number of bins  $b_i$  according to the countrate  $c_i$ .

$$b_i = N/c_i \times \text{bins per second}$$

The number of bins per second depend on the time resolution, for a time resolution of  $200\ \mu\text{s}$  there are 5 000 time bins per second.

For example, for a countrate of 1 000 cps and  $N=10\ 000$ , the photons are distributed randomly over 50 000 time bins. However, the countrate is not constant. Every  $c_i$  has another value according to the given PSD model for *kHz QPOs*.

The same time bin is readout after each run. In principal every time bin can be chosen, however, for a simulation of a whole lightcurve it should be always the same. Step by step a lightcurve is produced. Due to Poisson statistic, the photon distribution should follow an exponential distribution which is shown in Figure 7.11.

For *Simbol-X* and *IXO* simulations with different observation times has been performed. The significance is given as a simple signal-to-noise ratio, to give a rough estimation of the detection level. In any case this ratio is an under estimation of the real significance. The maximum signal is divided by the noise of the psd. In Figure 7.12 Two simulated PSD for *IXO* observations are shown in Figure 7.12. In the upper panel the observation time was 3.5 ks. The lines are detected with a  $4\ \sigma$  significance. For the centroid frequency of the lower frequency a best fit value of 801 Hz was determined, as well as a 90% confidence region of 786–812 Hz was given, which is an uncertainty in the order of 2%. The width of the line was restricted to 13–83 Hz with a best-fit value of 34 Hz. The higher frequency was found in a range of 1042–1078 Hz with a best-fit value of 1064 Hz, which lead also to an uncertainty of 2%. The width is constrained to 7–94 Hz with a best fit value of 34 Hz.

For the observation with 6.7 ks the confidence regions shrinks. The lower frequency was determined in a range of 796–802 Hz with a best-fit value of 799 Hz. The uncertainty is below 0.5%. The higher

frequency was found at 1056 Hz with a confidence region of 1052–1061 Hz ( $<0.5\%$ ). The width of both lines was constrained to a small frequency range of 40–60 Hz, with a best-fit value of 50 Hz.

In Figure 7.13 two simulated PSDs for *Simbol-X* are shown. In the upper panel an observation of 6,7 ks is shown. The lower frequency was constrained to a range of 795–810 Hz ( $\sim 1\%$ ) with a best-fit value of 802 Hz. The width of the line was restricted to 40–78 Hz with 56 Hz as best-fit value. The high frequency was determined to 1055 Hz with a confidence region of 1049–1061 Hz, whereas its width was restricted to 24–52 Hz with 36 Hz as best-fit value. The lines were detected with more than a  $3\sigma$  significance.

In the lower panel of Figure 7.13 a PSD of a 13.4 observation with *Simbol-X* is shown. The frequency at 802 Hz was constrained to 800–804 Hz, which lead to an uncertainty below 0.5%. The width was restricted to 36–51 Hz with 43 Hz as best-fit value. The high frequency was determined to 1061 Hz with an uncertainty of below 0.1% (1060–1064 Hz). The best-fit value of the width was 36 Hz with a confidence range of 24–52 Hz. The lines were detected with at least  $5\sigma$  significance.

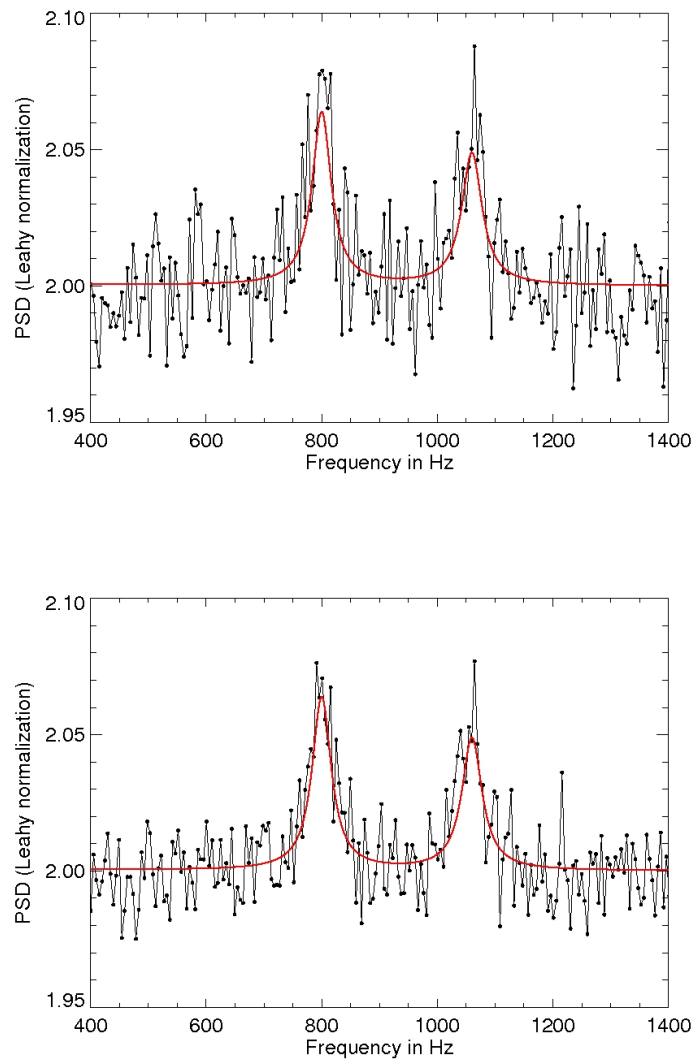


Figure 7.12: In the upper panel the  $\text{kHz}$  QPOs of 4U 1820-303 are shown observed by *IXO* in a 3.4 ks observation with at least  $4\sigma$  significance. The second panel shows a 6700 s observation in which the line is detected with more than  $5\sigma$ . The red curve is the input model.

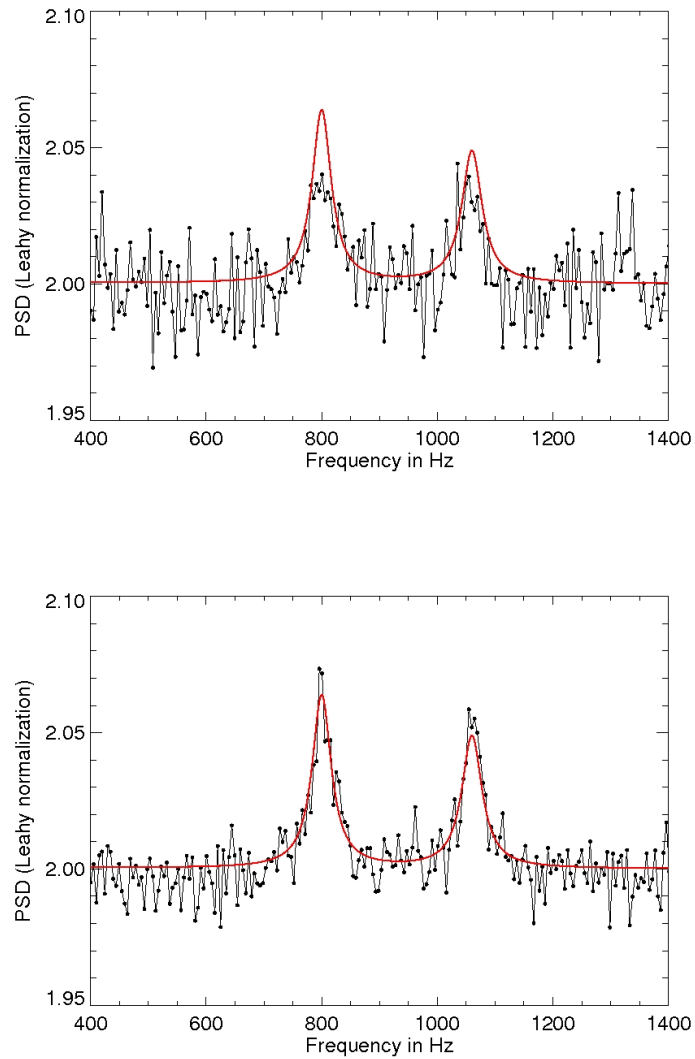


Figure 7.13: In the upper panel the  $k\text{Hz}$  QPOs of 4U 1820-303 are shown observed by *Symbol-X* in a 6.7 ks observation with at least  $3\sigma$  significance. The second panel shows a 13.4 ks observation in which the line is detected with more than  $5\sigma$ . The red curve is the input model.

## Chapter 8

# Conclusions and final remarks

The performances of new generation X-ray instruments LED onboard *Simbol-X* and the HTRS and WFI onboard *IXO* on the spectral and timing behaviour of *LMXB* have been studied in this thesis. Both missions will be able to constrain the parameters of the broad continuum spectrum of X-ray binary systems therefore determining on a large range all the physical components that contributes to the spectrum. More important for our work, we have shown that the parameters of the relativistically broadened iron line model (diskline) can be constrained with good precision.

In observations of sources like Serpens X-1, *Simbol-X* will constrain the parameters of the relativistic Iron line within a few percentages. Observations performed by *IXO* promise much better results. The line energy, and the inclination angle and the inner radius as well, will be constrained to confidence regions of less than 1%. A significant distinction between relativistic broad iron lines and broad gaussian profiles, arising from Doppler broadening, can then be obtained.

For sources with lower flux, like 4U 1820-303, it was shown that *Simbol-X*, as well as *IXO* will have difficulties in distinguishing between relativistic and non-relativistic broad iron lines. However, the diskline parameter can be constrained to confidence regions of the order of 10% for *Simbol-X*. *IXO* will provide more sensitive observations and therefore the parameters can be restricted to regions with few percentages. This might allow therefore variability studies that could help in discriminating the different scenarios.

For sources like Serpens X-1 and 4U 1820-303, both satellites are sensitive to changes in inclination angle and inner radius. However, in sources with a high inclination angle, like 4U 1636-536 ( $>60^\circ$ ), the parameters cannot be constrained within small regions. *Simbol-X* observations will give just a lower limit for the inclination angle. Also the inner radius cannot be constrained to regions with just a few percentages. *Simbol-X* will have a confidence regions of more than 100% but also *IXO* can constrain the inner radius to regions of more than 40%.

A significant detection of the line will be obtained with observations of  $\sim 1$  ks. And therefore time variability studies of the line becomes a real observational possibility.

Also the detection and characterization of timing properties can be obtained with observations of  $\sim 1$  ks for *IXO*. In fact, the characterization and detection of *kHz QPOs* in sources with typical fluxes of  $\sim 2.78 \times 10^{-9} \text{ erg cm}^{-2} \text{ s}^{-1}$ , like 4U 1820-303, can be reached with a few kilosecond observations. Our preliminary results show that *kHz QPOs* can be detected in such sources with significances of at least  $4\sigma$  for an observation time of 3 ks. *IXO* will allow simultaneous, precise measurements of timing and spectral properties of *LMXB* on timescales of around 1 ks. For brighter sources even using a few hundred seconds observations.

For *Simbol-X* a much lower countrate is expected (800 cps), so to detect the lines with a significance of at least  $5\sigma$  observations of more than 13 ks are necessary.

There are therefore reasons to believe that *Simbol-X* and *IXO* will provide new observational evidences towards the understanding of the variability of simultaneous spectral and timing properties of LMXRB. This will possibly allow to constrain the mass and the radius of the neutron star and probe the equation of states for compact matter in neutron stars. We consider the reported results are just preliminary. The study of the simultaneous detection of *kHz QPOs* and broad iron lines will be extend to other sources with higher countrates. Also the effects of broad band spectrum will be taken into account for the detection of the lines. Additionally, new models for the broad iron lines will be used. The assumption of a non-rotating neutron star of the diskline model holds not in any case. There have been already models with the spin as a free parameter published in literature.

# Bibliography

- Abramowicz M.A., Kluźniak W., 2001, *A&A* 374, L19
- Alpar M.A., Shaham J., 1985, *Nat* 316, 239
- Arnaud K.A., 1996, In: Jacoby G.H., Barnes J. (eds.) *Astronomical Data Analysis Software and Systems V*, Vol. 101. *Astronomical Society of the Pacific Conference Series*, p.17
- Asai K., Dotani T., Nagase F., Mitsuda K., 2000, *ApJS* 131, 571
- Aschenbach B., 1985, *Reports on Progress in Physics* 48, 579
- Balucinska-Church M., McCammon D., 1992, *ApJ* 400, 699
- Barret D., Boutelier M., Miller M.C., 2008, *MNRAS* 384, 1519
- Bhattacharyya S., Strohmayer T.E., 2007, *Astrophys. J., Lett.* 664, L103
- Boella G., Butler R.C., Perola G.C., et al., 1997, *A&AS* 122, 299
- Boella G., Chiappetti L., Conti G., et al., 1995, In: Fineschi S. (ed.) *Society of Photo-Optical Instrumentation Engineers (SPIE) Conference Series*, Vol. 2517. Presented at the *Society of Photo-Optical Instrumentation Engineers (SPIE) Conference*, p.223
- Bookbinder J., the IXO Study Coordination Group the IXO Science Definition Team et al., 2009, *The International X-ray Observatory*
- Bowyer S., Byram E.T., Chubb T.A., Friedman H., 1965, *Science* 147, 394
- Cackett E.M., Altamirano D., Patruno A., et al., 2009, *Astrophys. J., Lett.* 694, L21
- Cackett E.M., Miller J.M., Bhattacharyya S., et al., 2008, *ApJ* 674, 415
- Cappi M., Tombesi F., Giustini M., 2008, *Memorie della Societa Astronomica Italiana* 79, 123
- Casares J., Cornelisse R., Steeghs D., et al., 2006, *MNRAS* 373, 1235
- Church M.J., Balucinska-Church M., 1995, *A&A* 300, 441
- Church M.J., Balucińska-Church M., 2001, *A&A* 369, 915
- Church M.J., Bałucińska-Church M., 2004, *MNRAS* 348, 955
- Conti G., Mattaini E., Santambrogio E., et al., 1994, In: Hoover R.B., Walker A.B. (eds.) *Society of Photo-Optical Instrumentation Engineers (SPIE) Conference Series*, Vol. 2279. Presented at the *Society of Photo-Optical Instrumentation Engineers (SPIE) Conference*, p.101
- Cotroneo V., Basso S., Pareschi G., 2008, *Memorie della Societa Astronomica Italiana* 79, 239

- de Korte P.A.J., Bleeker J.A.M., McKechnie S.P., et al., 1981, *Space Science Reviews* 30, 495
- Della Ceca R., Severgnini P., Caccianiga A., et al., 2008, *Memorie della Societa Astronomica Italiana* 79, 65
- den Herder J.W., Brinkman A.C., Kahn S.M., et al., 2001, *A&A* 365, L7
- Di Salvo T., Iaria R., Robba N., Burderi L., 2006, *Chinese Journal of Astronomy and Astrophysics Supplement* 6, 010000
- Di Salvo T., Stella L., 2002, *ArXiv Astrophysics e-prints*
- Elsner R.F., Weisskopf M.C., Darbro W., et al., 1986, *ApJ* 308, 655
- Fabian A.C., 2006, *Astronomische Nachrichten* 327, 943
- Fabian A.C., Iwasawa K., Reynolds C.S., Young A.J., 2000, *PASP* 112, 1145
- Fabian A.C., Rees M.J., Stella L., White N.E., 1989, *MNRAS* 238, 729
- Ferrando P., Arnaud M., Briel U., et al., 2008, *Memorie della Societa Astronomica Italiana* 79, 19
- Fiore F., Arnaud M., Briel U., et al., 2008, *Memorie della Societa Astronomica Italiana* 79, 38
- Ford E., Kaaret P., Tavani M., et al., 1997a, *Astrophys. J., Lett.* 475, L123+
- Ford E., Kaaret P., Tavani M., et al., 1997b, *Astrophys. J., Lett.* 475, L123+
- Ford E.C., van der Klis M., Kaaret P., 1998a, *Astrophys. J., Lett.* 498, L41+
- Ford E.C., van der Klis M., van Paradijs J., et al., 1998b, *Astrophys. J., Lett.* 508, L155
- Forman W., Jones C., Cominsky L., et al., 1978, *ApJ* 38, 357
- Frontera F., Costa E., et al. 1995, In: *International Cosmic Ray Conference, Vol. 2. International Cosmic Ray Conference*, p.41
- Giacconi R., Branduardi G., Briel U., et al., 1979, *ApJ* 230, 540
- Giacconi R., Gursky H., Paolini F.R., Rossi B.B., 1962, *Phys. Rev. Lett.* 9, 439
- Giacconi R., Gursky H., van Speybroeck L.P., 1968, *ARA&A* 6, 373
- Giacconi R., Kellogg E., Gorenstein P., et al., 1971, *ApJ* 165, L27+
- Giacconi R., Reidy W.P., Vaiana G.S., et al., 1969, *Space Science Reviews* 9, 3
- Giacconi R., Rossi B., 1960, *J. Geophys. Res.* 65, 773
- Giarrusso S., Santangelo A.E., Fazio G., et al., 1995, In: *Fineschi S. (ed.) Society of Photo-Optical Instrumentation Engineers (SPIE) Conference Series, Vol. 2517. Presented at the Society of Photo-Optical Instrumentation Engineers (SPIE) Conference*, p.234
- Grimm H.J., Gilfanov M., Sunyaev R., 2003, *Chinese Journal of Astronomy and Astrophysics Supplement* 3, 257
- Grindlay J., Gursky H., Schnopper H., et al., 1976, *Astrophys. J., Lett.* 205, L127
- Gruber D.E., Blanco P.R., Heindl W.A., et al., 1996, *A&AS* 120, C641+
- Haensel P., 2003, In: *Motch C., Hameury J.M. (eds.) EAS Publications Series, Vol. 7. EAS Publications Series*, p.249

- Hasinger G., van der Klis M., 1989, *A&A* 225, 79
- Homan J., Méndez M., Wijnands R., et al., 1999, *Astrophys. J., Lett.* 513, L119
- Jager R., Heise J., in 't Zand J.J.M., Brinkman A.C., 1993, *Advances in Space Research* 13, 315
- Jahoda K., Swank J.H., Giles A.B., et al., 1996, In: Siegmund O.H., Gummin M.A. (eds.) *Society of Photo-Optical Instrumentation Engineers (SPIE) Conference Series*, Vol. 2808. *Society of Photo-Optical Instrumentation Engineers (SPIE) Conference Series*, p.59
- Jonker P.G., van der Klis M., Homan J., et al., 2001, *ApJ* 553, 335
- Jonker P.G., van der Klis M., Wijnands R., et al., 2000, *ApJ* 537, 374
- Jonker P.G., Wijnands R., van der Klis M., et al., 1998, *Astrophys. J., Lett.* 499, L191+
- Kaaret P., in 't Zand J.J.M., Heise J., Tomsick J.A., 2002, *ApJ* 575, 1018
- Kluzniak W., Abramowicz M.A., 2001, *Acta Physica Polonica B* 32, 3605
- Lamb F.K., Shibazaki N., Alpar M.A., Shaham J., 1985, *Nat* 317, 681
- Lattimer J.M., Prakash M., 2001, *ApJ* 550, 426
- Laurent P., Lechner P., Authier M., et al., 2008, *Memorie della Societa Astronomica Italiana* 79, 32
- Leahy D.A., Darbro W., Elsner R.F., et al., 1983, *ApJ* 266, 160
- Lechner P., 2009, In: Rodriguez J., Ferrando P. (eds.) *American Institute of Physics Conference Series*, Vol. 1126. *American Institute of Physics Conference Series*, p.21
- Levine A.M., Cui W., Remillard R., et al., 1996, In: *Bulletin of the American Astronomical Society*, Vol. 28. *Bulletin of the American Astronomical Society*, p.1316
- Lewin W.H.G., van der Klis M., 2006, *Compact stellar X-ray sources*
- Lewin W.H.G., van Paradijs J., van den Heuvel E.P.J., (eds.) 1995, *X-ray binaries*
- Lightman A.P., White T.R., 1988, *ApJ* 335, 57
- Linares M., van der Klis M., Altamirano D., Markwardt C.B., 2005, *ApJ* 634, 1250
- Longair M.S., 1992, *High energy astrophysics. Vol.1: Particles, photons and their detection*
- Longair M.S., 1994, *High energy astrophysics. Volume 2. Stars, the Galaxy and the interstellar medium.*
- Markwardt C.B., Strohmayer T.E., Swank J.H., 1999, *Astrophys. J., Lett.* 512, L125
- Mason K.O., Breeveld A., Much R., et al., 2001, *A&A* 365, L36
- Méndez M., van der Klis M., 1999, *Astrophys. J., Lett.* 517, L51
- Mendez M., van der Klis M., van Paradijs J., et al., 1998, *Astrophys. J., Lett.* 494, L65+
- Meuris A., Limousin O., Lugiez F., et al., 2009, In: Rodriguez J., Ferrando P. (eds.) *American Institute of Physics Conference Series*, Vol. 1126. *American Institute of Physics Conference Series*, p.25
- Miller M.C., Lamb F.K., Psaltis D., 1998, *ApJ* 508, 791
- Mitsuda K., Inoue H., Koyama K., et al., 1984, *PASJ* 36, 741

- Mitsuda K., Inoue H., Nakamura N., Tanaka Y., 1989, PASJ 41, 97
- Morrison R., McCammon D., 1983, ApJ 270, 119
- Muno M.P., 2007, In: di Salvo T., Israel G.L., Piersant L., Burderi L., Matt G., Tornambe A., Menna M.T. (eds.) *The Multicolored Landscape of Compact Objects and Their Explosive Origins*, Vol. 924. American Institute of Physics Conference Series, p.166
- Nugent J.J., Jensen K.A., Nousek J.A., et al., 1983, ApJS 51, 1
- Oosterbroek T., Barret D., Guainazzi M., Ford E.C., 2001, A&A 366, 138
- Pandel D., Kaaret P., Corbel S., 2008, ApJ 688, 1288
- Pareschi G., Ghigo M., Basso S., et al., 2009, In: *Bulletin of the American Astronomical Society*, Vol. 41. *Bulletin of the American Astronomical Society*, p.359
- Pareschi G., the SIMBOL-X collaboration 2008, *Memorie della Societa Astronomica Italiana* 79, 26
- Peacock A., Andresen R.D., Manzo G., et al., 1981, *Space Science Reviews* 30, 525
- Piraino S., Santangelo A., di Salvo T., et al., 2007, A&A 471, L17
- Piraino S., Santangelo A., Ford E.C., Kaaret P., 1999, A&A 349, L77
- Piraino S., Santangelo A., Kaaret P., 2000, A&A 360, L35
- Pottschmidt K., 2002, PhD thesis: *Accretion Disk Weather of Black Hole X-Ray Binaries - The Case of Cygnus X-1*, IAAT
- Rybicki G.B., Lightman A.P., 1986, *Radiative Processes in Astrophysics*
- Setti G., Woltjer L., 1989, A&A 224, L21
- Seward F.D., Charles P.A., 1995, *Exploring the X-Ray Universe*
- Smale A.P., Zhang W., White N.E., 1997, *Astrophys. J., Lett.* 483, L119+
- Stella L., Priedhorsky W., White N.E., 1987, *Astrophys. J., Lett.* 312, L17
- Stella L., Vietri M., 1998, *Astrophys. J., Lett.* 492, L59+
- Stella L., Vietri M., 1999, *Physical Review Letters* 82, 17
- Strohmayer T., Zhang W., Swank J., 1996, *IAU Circ.* 6320, 1
- Strohmayer T.E., Brown E.F., 2002, ApJ 566, 1045
- Strüder L., Briel U., Dennerl K., et al., 2001, A&A 365, L18
- Swank J.H., Becker R.H., Pravdo S.H., Serlemitsos P.J., 1976 2963, 1
- Timmer J., Koenig M., 1995, A&A 300, 707
- Titarchuk L., 1994, ApJ 434, 570
- Truemper J., 1982, *Advances in Space Research* 2, 241
- Truemper J., Pietsch W., Reppin C., et al., 1978, *Astrophys. J., Lett.* 219, L105

- Turner M.J.L., Abbey A., Arnaud M., et al., 2001, *A&A* 365, L27
- Turner M.J.L., Smith A., Zimmermann H.U., 1981, *Space Science Reviews* 30, 513
- van der Klis M., Swank J.H., Zhang W., et al., 1996, *Astrophys. J., Lett.* 469, L1+
- van Paradijs J., van der Klis M., van Amerongen S., et al., 1990, *A&A* 234, 181
- van Straaten S., van der Klis M., Méndez M., 2003, *ApJ* 596, 1155
- Voges W., Aschenbach B., Boller T., et al., 1999a, *A&A* 349, 389
- Voges W., Boller T., Dennerl K., et al., 1999b, In: Aschenbach B., Freyberg M.J. (eds.) *Highlights in X-ray Astronomy.*, p.282
- White N.E., Nagase F., Parmar A.N., 1995, In: Lewin W.H.G., van Paradijs J., van den Heuvel E.P.J. (eds.) *X-ray binaries*, p. 1 - 57., p.1
- White N.E., Peacock A., Hasinger G., et al., 1986, *MNRAS* 218, 129
- White N.E., Stella L., Parmar A.N., 1988, *ApJ* 324, 363
- Wijnands R., Homan J., van der Klis M., et al., 1998a, *Astrophys. J., Lett.* 493, L87+
- Wijnands R., Homan J., van der Klis M., et al., 1997a, *Astrophys. J., Lett.* 490, L157+
- Wijnands R., Mendez M., van der Klis M., et al., 1998b, *Astrophys. J., Lett.* 504, L35+
- Wijnands R., van der Klis M., 1998, *Astrophys. J., Lett.* 507, L63
- Wijnands R.A.D., van der Klis M., 1997, *Astrophys. J., Lett.* 482, L65+
- Wijnands R.A.D., van der Klis M., van Paradijs J., et al., 1997b, *Astrophys. J., Lett.* 479, L141+
- Wilms J., Allen A., McCray R., 2000, *ApJ* 542, 914
- Wilms J., Kendziorra E., Martin M., et al., 2004, In: Hasinger G., Turner M.J.L. (eds.) *Society of Photo-Optical Instrumentation Engineers (SPIE) Conference Series*, Vol. 5488. Presented at the Society of Photo-Optical Instrumentation Engineers (SPIE) Conference, p.341
- Wolter H., 1952a, *Ann. d. Phys.* 445, 94
- Wolter H., 1952b, *Ann. d. Phys.* 445, 286
- Zhang W., Lapidus I., White N.E., Titarchuk L., 1996, *Astrophys. J., Lett.* 469, L17+
- Zhang W., Smale A.P., Strohmayer T.E., Swank J.H., 1998a, *Astrophys. J., Lett.* 500, L171+
- Zhang W., Strohmayer T.E., Swank J.H., 1998b, *Astrophys. J., Lett.* 500, L167+



# Online references

National Air and Space Museum:

<http://www.nasm.si.edu/exhibitions/gall114/spacerace/sec200/sec231.htm>

Visited: 14th January 2009

*High Energy Astrophysics Science Archive Research Center* (HEASARC), National Aeronautics and Space Administration (NASA):

<http://heasarc.gsfc.nasa.gov>

Visited: 14th January 2009

*Symbol-X Webpage*, CNES:

<http://smc.cnes.fr/SIMBOLX/index.htm>

Visited 14th January 2009

*European Space Agency*:

<http://www.rssd.esa.int>

Visited: 5th May 2009

*Agenzia Spaziale Italiana*:

<http://www.asdc.asi.it>

Visited: 7th May 2009

*Catalogues of ROSAT all-sky*:

<http://www.mpe.mpg.de/xray/wave/rosat/catalogue/>

Visited: 7th May 2009

*XMM-Newton Science Operations Centre*:

<http://xmm.esac.esa.int>

Visited: 7th May 2009

*International X-ray observatory (IXO)*:

<http://ixo.gsfc.nasa.gov>

Visited: 14th May 2009

*IXO II* :

<http://jeeves.cfa.harvard.edu/ixo/IXOHome>

Visited: 14th May 2009

*Jörn Wilms teaching page* (Wilms):

<http://pulsar.sternwarte.uni-erlangen.de/wilms/teach/index.html>

Visited: 14th May 2009



# Danksagungen

An dieser Stelle möchte ich mich bei allen bedanken, die zum Gelingen dieser Arbeit beigetragen haben. Sei es durch physikalische Diskussionen oder durch Unterstützung und Ablenkung zur richtigen Zeit.

## **Vielen dank an:**

**Prof. Dr. Andrea Santangelo** für die Vergabe des Themas und die Korrektur dieser Arbeit, sowie für seine interessanten Vorlesungen, die mein Interesse an der Astronomie noch gesteigert haben.

**Dr. Dmitry Klochkov** für die Ideen und Diskussionen rund um die Diplomarbeit, sowie für das Korrektur lesen.

**Dr. Santina Piraino** für ihre Tipps zu dem Thema low mass X-ray binaries und *kHz QPOs*

**Michael Martin** ohne dessen zahlreichen Ratschläge zum richtigen umgehen mit LaTeX, IDL und vielen anderen Dingen diese Arbeit nicht ihr jetziges Aussehen hätte. Sowie für, zusammen mit

**Stefan Schwarzburg** , das Korrekturlesen der Rohfassungen, die, vor allem zu Beginn, sicherlich nicht leicht zu lesen waren.

**die Espressorunde** die mir den Genuss von Espresso, und Kaffee im allgemeinen, schmackhaft gemacht hat und ohne die manch einen Tag gerettet hat.

**das gesamte Institut** für eine angenehme Atmosphäre, in der man immer und jeden um Hilfe bitten konnte.

**alle** , die ich vergessen hab namentlich zu erwähnen

**meine Eltern** die mich das ganze Studium lang unterstützt haben.

**meine Freundin Judith** die, vor allem in den letzten Wochen, sehr oft auf mich verzichten musste, sowie für ihre richtigen Worte zur richtigen Zeit und dass sie mich immer unterstützt hat.



# Erklärung

Hiermit erkläre ich, dass ich die Diplomarbeit mit dem Titel “Compact objects with neutron stars observed with Simbol-X” selbstständig verfasst und dabei keine anderen als die angegebenen Quellen und Hilfsmittel benutzt habe.

Tübingen, den 16. Juni 2009

Benjamin Mück